The Dissertation Committee for Xi Chen Certifies that this is the approved version of the following dissertation:

Synthesis and Thermoelectric Properties of Higher Manganese Silicides for Waste Heat Recovery

Committee:

Li Shi, Supervisor

Jianshi Zhou, Co-Supervisor

John B. Goodenough

John T. Markert

Nicole A. Benedek

Synthesis and Thermoelectric Properties of Higher Manganese Silicides for Waste Heat Recovery

by

Xi Chen, B.E.; M.E.

Dissertation

Presented to the Faculty of the Graduate School of

The University of Texas at Austin

in Partial Fulfillment

of the Requirements

for the Degree of

Doctor of Philosophy

The University of Texas at Austin

December, 2014

Dedication

To my parents

Acknowledgements

First and foremost I would like to thank my advisors, Prof. Li Shi and Prof. Jianshi Zhou, for their educational and financial support during the past four and half years. Their diligent working attitude and rigorous research methods taught me so much from research to life. I am deeply indebted to them and truly appreciate their professional and personal advice. I am also indebted to my former supervisors of Zhejiang University, Prof. Tiejun Zhu and Prof. Xinbing Zhao, who initially led me to the field of thermoelectrics. I also would like to thank Prof. John B. Goodenough, Prof. John T. Markert and Prof. Nicole B. Benedek, for serving as my committee members and providing valuable suggestions.

I also want to thank Prof. Song Jin, Dr. Steven N. Girard, Ankit Pokhrel, Fei Meng, Dr. Olivier Delaire, Prof. Natalio Mingo, Dr. Jesús Carrete, Prof. Derek A. Stewart and Dr. Saikat Mukhopadhyay for their collaborative work and insightful discussion.

Many thanks should also go to previous and present group members: Dr. Feng Zhou, Dr. Arden Moore, Dr. Michael Pettes, Dr. Chad Baker, Dr. Insun Jo, Dr. Daniel Sellan, Dr. Shaoyi Wen, Annie Weathers, Sean Sullivan, Mir Mohammad Sadeghi, JaeHyun Kim, Evan Fleming, Patrick Jurney, Gabriella Coloyan, Eric Ou, Brandon Smith, David Choi, Haiyan Z Fateh, Libin Zhang, Dr. Lu Zhang, Dr. Jinguang Cheng, Dr. Biao Hu, Dr. Luke Marshall, Dr. Sebastian Larregola, Dr.Yuichi Shirako, Zongyao Li, and Dr. Xiang Li for their help and friendship.

Finally, I am deeply grateful to my parents for their love, sacrifice and encouragement.

Synthesis and Thermoelectric Properties of Higher Manganese silicides for Waste Heat Recovery

Xi Chen, Ph.D.

The University of Texas at Austin, 2014

Supervisors: Li Shi, Jianshi Zhou

Thermoelectric (TE) materials, which can convert temperature gradients directly into electricity and vice versa, have received renewed interest for waste heat recovery and refrigeration applications. Higher manganese silicides (HMS) are promising *p*-type TE materials due to the abundance of the constituent elements, environmental friendliness, and good chemical stability. The objective of this dissertation is to establish a better understanding of the structure-TE properties relationship of HMS with a complex Nowotny chimney ladder structure. The focus of this work is on the investigations of the phonon dispersion of HMS crystals and the effects of chemical doping and nanostructuring on the TE properties of polycrystalline HMS.

HMS crystals have been synthesized by the Bridgeman method for inelastic neutron scattering measurements of the phonon dispersion. In conjunction with density functional theory calculations, the results clearly show the presence of numerous low-lying optical phonon branches, especially an unusually low-energy optical phonon polarization associated with the twisting motions of the Si helical ladders in the Mn chimneys. The obtained phonon dispersion can be used to explain the low and anisotropic thermal conductivity of HMS crystals.

(Al,Ge) double doping was found to be effective in modifying the electrical properties of HMS polycrystals. The peak thermoelectric power factor occurs at an optimized hole concentration of $1.8\sim2.2\times10^{21}$ cm^{-3} at room temperature. On the other hand, Re substitution can suppress the lattice thermal conductivity to approach the calculated minimum value corresponding to the amorphous limit. Meanwhile, the thermoelectric power factor does not markedly change at low Re content of $x \leq 0.04$ although it drops considerably with increasing Re content. Hence, the peak *ZT* has been improved to ~0.6 in both systems.

The effects of nanostructuring on the TE properties have been studied in the cold-pressed samples and ball-milled samples. The thermal conductivity was reduced remarkably by decreasing the grain size. It is found that the grain size effects are more significant at low temperature. However, it is difficult to reduce the grain size to less than 50 nm without the formation of impurity phases by ball milling. These facts limit the *ZT* enhancement of the nanostructured HMS at high temperatures in this study.

Table of Contents

List of Tables

List of Figures

Chapter 1: Introduction

1.1 THERMOELECTRIC PHENOMENA

The increasing global need for energy and the negative environmental consequence of fossil fuels have motivated the investigation of renewable energy sources and efficient energy conversion methods. One energy conversion technology that has received renewed attention recently is thermoelectric (TE) cooling and power generation, which is based on solid-state devices for direct energy conversion between heat and electricity. Compared to other conventional energy conversion technologies based on mechanical systems, the solid-state TE device has several unique features, including the absence of moving parts, ease to switch between the power generation and refrigeration modes, low maintenance cost, and its ability to be readily integrated with other energy conversion devices.[1,2]

1.1.1 Thermoelectric effects

The research on thermoelectrics has a long history of about 200 years. In 1821, the Baltic German physicist Thomas Johann Seebeck first discovered that a compass needle would be deflected by a closed loop formed by two different metals joined in two places when there was a temperature difference between the junctions.[3] This effect, which is converting temperature difference directly into electricity, was later named after him. The Seebeck coefficient (S) is defined as

$$S = -\frac{V}{T_2 - T_1}, \tag{1.1}$$

where V is the voltage drop measured from the hot side to the cold side; T_2 and T_1 are the temperature of the hot side and cold side, respectively.

In 1834, the reverse-Seebeck effect, which is known as the Peltier effect, was found by French physicist Jean Charles Athanase Peltier. When a current I flows through a junction between two materials a and b, heat can be either generated or absorbed depending on the direction of the current.[4] The Peliter heat (Q) generated or absorbed by the junction is calculated as

$$Q = (\pi_a - \pi_b)I = \pi_{ab} I\,, \tag{1.2}$$

where π_a, π_b, and π_{ab} are the Peltier coefficient of material a, material b, and the thermocouple made by a and b, respectively.

In 1851, Lord Kelvin predicted and subsequently observed the third thermoelectric effect, which is known as the Thomson effect.[5] If a current (I) passes through a homogeneous conductor, the heat production rate $\dot{q}$ is proportional to the current and the temperature gradient (∇T) along the direction of the current:

$$\dot{q} = -\beta I \cdot \nabla T\,, \tag{1.3}$$

where β is called Thomson coefficient. It should be noted that the Thomson heat changes sign if the current changes direction.

These three thermoelectric effects are not independent. They are related to each other through the Kelvin relations:

$$S = \pi T\,, \tag{1.4a}$$

$$\frac{dS}{dT} = \frac{\beta}{T}\,. \tag{1.4b}$$

1.1.2 Thermoelectric transport theory and thermoelectric devices

In the 1940s, A.F. Ioffe was the first to develop the modern theory of thermoelectricity using the concept of the "figure of merit" *ZT*.[6] *ZT* is an intrinsic material parameter related to the thermal and electrical transport properties, and is given by

$$ZT = S^2\sigma T/\kappa, \tag{1.5}$$

where S, σ, T, and κ are the Seebeck coefficient, electrical conductivity, absolute temperature, and thermal conductivity, respectively. The numerator $S^2\sigma$ reflects the electrical performance of a material and is called the power factor (*PF*). κ mainly consists of two parts: the electronic thermal conductivity (κ_E) and lattice thermal conductivity (κ_L). Therefore, a good TE material should have high S and σ, but low κ_L. However, it is challenging to obtain high *ZT* values since the three transport properties are inter-dependent. As the charge carrier concentration increases, σ increases while S decreases. In addition, κ_E is related to σ according to the Wiedemann-Franz law.

1.1.2.1 Electrical conductivity

Electrical conductivity measures a material's ability to conduct an electric current, and is defined as

$$\sigma = ne\mu\,, \tag{1.6}$$

where n, e and μ are the charge-carrier concentration, electron charge, and mobility, respectively. Based on the Boltzmann transport theory and the assumption of a single parabolic band, the charge-carrier concentration can be expressed as

$$n = \frac{4\pi}{h^3}\left(2m^* k_B T\right)^{\frac{3}{2}} F_{\frac{1}{2}}(\xi), \tag{1.7a}$$

$$F_n(\xi) = \int x^n \left(e^{x-\xi} + 1\right)^{-1} dx\,, \tag{1.7b}$$

$$\xi = E_F / k_B T \tag{1.7c}$$

where h is the Plank constant, k_B is the Boltzmann constant, m^* is density of states effective mass, and ξ is the reduced Fermi level, which is related to the relative position of the Fermi level E_F.

The mobility μ can be calculated according to Matthiessen's rule as $1/\mu = \sum 1/\mu^i$, where μ^i is the mobility due to different scattering mechanisms. Assuming a single parabolic band model, the carrier mobility governed by the acoustic phonon scattering (μ^{ph}), grain boundary scattering (μ^{gb}), and alloy scattering (μ^{al}) can be expressed, respectively, as[7-9]

$$\mu^{ph} = \frac{\sqrt{2}\pi e\hbar^4}{3(k_B T)^{3/2}} \frac{v_L^2 \rho}{\Xi^2 (m_b^*)^{3/2} m_I^*} \frac{F_0(\eta)}{F_{1/2}(\eta)}, \tag{1.7d}$$

$$\mu^{gb} = L_{eff} e \left(\frac{1}{2\pi m_b^* k_B T}\right)^{1/2} \exp\left(\frac{E_B}{k_B T}\right), \tag{1.7e}$$

$$\mu^{al} = \frac{16 e\hbar^4}{9\sqrt{2}\pi x(1-x)(k_B T)^{1/2}} \frac{N_0}{\Xi^2 (m_b^*)^{3/2} m_I^*} \frac{F_0(\eta)}{F_{1/2}(\eta)}, \tag{1.7f}$$

where v_L is the longitudinal sound velocity, ρ is the mass density, Ξ is the deformation potential, L_{eff} is effective crystal size, E_B is energy barrier height, m_I^* is inertial effective mass, x is the fractional concentration, and N_0 is the number of atoms per unit volume. In addition, average (single valley) density-of-states (DOS) mass m_b^* is related to m^* according to $m^* = N_V^{2/3} m_b^*$, where N_V is the valley degeneracy.

1.1.2.2 Seebeck coefficient

According to the Boltzmann transport theory, the Seebeck coefficient can be expressed as

$$S = \pm \frac{k_B}{e}\left[\frac{\left(r+\frac{5}{2}\right)F_{\frac{3}{2}+r}(\xi)}{\left(r+\frac{3}{2}\right)F_{\frac{1}{2}+r}(\xi)} - \xi\right], \tag{1.8}$$

where r is the exponent contained in the approximation of the carrier scattering time $\tau = \tau_0 (E/k_B T)^r$, where E is the carrier energy and τ_0 is a constant. The scattering factors for acoustic phonons, optical phonons, ionized impurity, alloy, and neutral impurity scattering are -1/2, 1/2, 3/2, -1/2, and 0, respectively. The negative and positive sign of S correspond to *n*-type and *p*-type conduction, respectively.

A non-degenerate semiconductor is one where the Fermi level lies within the forbidden gap and far from the edge of the band in which the carriers reside. In this case, the Seebeck coefficient is given by[10]

$$S = \pm \frac{k_B}{e}\left[\xi - \left(r+\frac{5}{2}\right)\right]. \tag{1.9}$$

A high level doping in a semiconductor moves the Fermi level to the band that holds the majority charge carriers. In this case, the semiconductor, which acts more like a metal, is called a degenerate semiconductor. The Seebeck coefficient for a metal is given by

$$S = -\frac{\pi^3}{3}\frac{k_B}{e}\frac{r+3/2}{\xi}. \tag{1.10}$$

1.1.2.3 Thermal conductivity

Heat energy in a TE material is mainly carried by charge carriers (electrons and holes) and lattice vibration (phonons). The lattice thermal conductivity can be expressed as

$$\kappa_L = \sum_{Pola}\int_0^{+\infty}\frac{1}{3}\hbar\omega\cdot\frac{df_0}{T}\cdot v^2\tau\cdot D(\omega)d\omega \quad , \tag{1.11}$$

where $\hbar$, ω, v, f_0, τ and $D(\omega)$ are reduced Plank constant, phonon frequency, group velocity, phonon distribution function, relaxation time and density of states, respectively. The summation is over all phonon polarizations in the Brillouin zone.

The electronic thermal conductivity can be calculated according to the Wiedemann-Franz law as

$$\kappa_E = L\sigma T , \tag{1.12}$$

where L is the Lorenz number. L is not a universal factor, but depends on the kind of materials and doping level. For doped semiconductors, L is about 1.5-2.5 × 10^{-8} W Ω K^{-2}. For many metals, L is close to the Sommerfeld theoretical value of 2.44 × 10^{-8} W Ω K^{-2} for electron gas.

1.1.2.4 Two band model of thermoelectric transport

If both electrons and holes contribute to the thermoelectric transport in a semiconductor, a two-band model[11] can be used to describe the transport parameters. Assuming charge-carrier scattering is dominated by acoustic phonon scattering and boundary scattering. The Seebeck coefficient is given as

$$S = \frac{S_e n\mu_e + S_h p\mu_h}{n\mu_e + p\mu_h}, \tag{1.13}$$

where μ_e and μ_h are the hole and electron mobilities, p and n are the hole and electron concentrations, and the electron and hole contributions to the Seebeck coefficients are given, respectively, as

$$S_e = -\frac{k_B}{e}\left[\frac{\left(r+\frac{5}{2}\right)F_{\frac{3}{2}+r}(\xi_e)}{\left(r+\frac{3}{2}\right)F_{\frac{1}{2}+r}(\xi_e)} - \xi_e\right], \tag{1.14}$$

and

$$S_h = \frac{k_B}{e}\left[\frac{\left(r+\frac{5}{2}\right)F_{\frac{3}{2}+r}(\xi_h)}{\left(r+\frac{3}{2}\right)F_{\frac{1}{2}+r}(\xi_h)} - \xi_h\right]. \tag{1.15}$$

The reduced Fermi level for electrons, $\xi_e = E_F / k_B T$, where E_F is measured from the conduction band edge and is negative when it is in the band gap. The reduced hole Fermi level is defined as $\xi_h = -(E_F + E_g)/k_B T$, where E_g is the band gap, and ξ_h is also negative when E_F is in the gap.

In addition, the electrical conductivity is calculated as

$$\sigma = ne\mu_e + pe\mu_h \tag{1.16}$$

The Hall coefficient in the low field limit can be reduced to

$$R_H = \frac{r_H e}{\sigma^2}\left[p\mu_h^2 - n\mu_e^2\right], \tag{1.17}$$

where r_H is given by[12]

$$r_H = \frac{3\sqrt{\pi}}{4}\frac{\left(2r+\frac{3}{2}\right)!}{\left[\left(r+\frac{3}{2}\right)!\right]^2} \quad . \tag{1.18}$$

When acoustic phonon scattering and boundary scattering are the dominant charge carrier scattering mechanism, r = -1/2, and r_H = 1.18. Equations (1.13), (1.16) and (1.17) can all be reduced to functions of the Fermi levels, the hole and electron density of states effective masses, m_h^* and m_e^*, and the hole and electron mobilities by employing the following carrier concentration expressions

$$p = \frac{4\pi}{h^3}\left(2m_h^* k_B T\right)^{\frac{3}{2}} F_{\frac{1}{2}}\left(\xi_h\right), \tag{1.19}$$

$$n = \frac{4\pi}{h^3}\left(2m_e^* k_B T\right)^{\frac{3}{2}} F_{\frac{1}{2}}\left(\xi_e\right). \tag{1.20}$$

The total electronic contribution to the thermal conductivity consists of three parts

$$\kappa_E = \kappa_e + \kappa_h + \frac{e\left(p\mu_h n\mu_e\right)}{n\mu_e + p\mu_h}\left(S_h - S_e\right)^2 T\ , \tag{1.21}$$

where the first and second term refer to the electron (κ_e) and hole (κ_h) contributions to the thermal conductivity, and the third term refers to the bipolar contribution (κ_b), which can be large in some materials at high temperatures as the E_F moves into the middle of the gap. The first two terms can be found from[13]

$$\kappa_{e,h} = \frac{1}{T^2}\left[K_2 - \frac{K_1^2}{K_0}\right], \tag{1.22}$$

where

$$K_S = \frac{8\pi}{3}\left(\frac{2}{h^2}\right)^{3/2}\frac{\left(m_h^*\right)^{3/2}}{m_I^*} T\tau_0\left(s + r + \frac{3}{2}\right)\left(k_B T\right)^{s+3/2} F_{s+r+1/2}\left(\xi_{e,h}\right). \tag{1.23}$$

The dependence of K_S on the scattering rate τ_0 is eliminated by substituting $\tau_0 = 3\sqrt{\pi}m_I^*\mu / 4e\left(r + 3/2\right)!$ into equation (1.23),[12] which also eliminates the dependence on the inertial effective mass, which can differ greatly from the density of states effective mass (m_h^*) due to a high degree of band degeneracy.[14] When m_I^* and m_h^* are taken to be equal, as is the case for isotropic materials with a single valley, the expression for K_S commonly found in literature[15] can be recovered.

1.1.2.5 The efficiency of a TE device

A TE device is made from TE modules which consist of *p*-type and *n*-type materials. A simple configuration of TE devices for power generation and refrigeration is illustrated in Figure 1.1. The performance of a TE device depends on the temperature gradient and the dimensionless figure of merit *ZT*. The maximum efficiency of a TE power generation device (η) can be calculated as[16]

$$\eta = \frac{T_H - T_C}{T_H} \frac{\sqrt{1+ZT_{avg}} - 1}{\sqrt{1+ZT_{avg}} + \frac{T_C}{T_H}}, \tag{1.24}$$

where T_C and T_H are temperatures of the cold and hot sides in a TE module and T_{avg} is the average temperature. It is clear from equation (1.24) that a high efficiency of a TE device requires high *ZT* values and a large temperature difference across the TE module. Therefore, developing advanced TE materials with enhanced *ZT* values is the key to improving the TE technology.

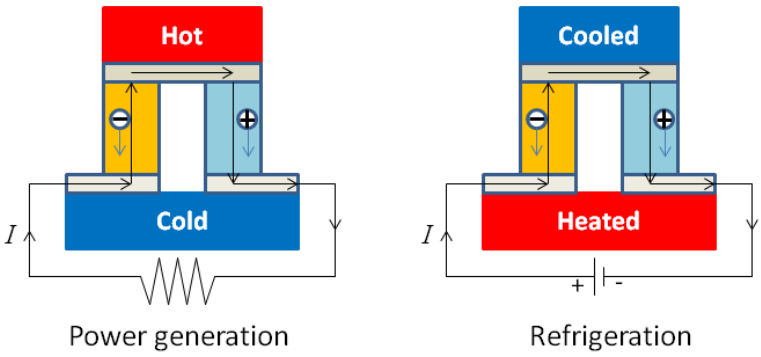

Figure 1.1: Thermoelectric power generation and refrigeration.

Since the discovery of the Seebeck effect in the 1821, a number of materials have been synthesized and studied for TE applications. Most of them are degenerately doped

semiconductors, including the Bi_2Te_3-based alloy for room-temperature application, PbTe-based alloy for intermediate temperature application, and SiGe-based alloy for high-temperature application. However, these state-of-the-art TE materials contain rare, relatively costly, or toxic elements. Thus, there is a need to develop environmentally friendly TE materials made of earth-abundant elements with low cost.

1.2 RECENT DEVELOPMENTS IN THERMOELECTRIC MATERIALS

For a long time, the best *ZT* of TE materials stayed around 1. Since the 1990s, we have witnessed a significant progress made in the peak *ZT* value. So far the highest reported *ZT* value has exceeded 2 in PbTe-based alloy[17] and SnSe single-crystal[18]. Several successful strategies have been employed to improve the *ZT* of TE materials, such as nanostructuring and band engineering. In addition, some efforts have been devoted to develop TE materials with complex crystal structures.

1.2.1 Nanostructured TE materials

The interest in nanostructured TE materials was initially inspired by the theoretical predictions by Hicks and Dresselhaus.[19,20] It is proposed that the power factor can be enhanced in two-dimensional quantum wells or one-dimensional quantum wires due to the sharp increase in the electron DOS. Since then, a lot of studies have been focused on synthesis and characterization of low-dimensional TE materials. For example, high *ZT* values up to 2.4 and 1.6 have been reported in Bi_2Te_3/Sb_2Te_3 supperlattices[21] and PbSeTe/PbTe quantum dot supperlattices[22], although these results remain to be verified independently.[23-25] It should be noted that the observed *ZT* enhancement in these systems is mainly due to the suppression of lattice thermal conductivity instead of improvement of power factor.

Despite the many successes in several low-dimensional systems, it is generally difficult to prepare the materials and to measure the TE properties. Recently, increasing efforts have been devoted to developing high performance nanostructured bulk materials and nanocomposites. The *ZT* values can be enhanced only if grain boundary scattering can result in larger reduction in the lattice thermal conductivity than in the power factor. Hsu *et al.*[26] reported that the peak *ZT* of cubic $AgPb_mSbTe_{2+m}$ can reach ~2.2 at 800 K, and this high *ZT* is attributed to the formation of "nanodot" in this material. Zhao *et al.*[27] prepared nanotube-containing Bi_2Te_3 nanocomposites, and observed a remarkable reduction in thermal conductivity with electrical conductivity much less affected. Poudel *et al.*[28] prepared nanostructured bulk Bi_2Te_3 by ball milling and hot pressing, and achieved a peak *ZT* of 1.4 at 100 ^oC. The similar methods have also been used to synthesize nanostructured n-type SiGe[29] and a peak *ZT* of 0.95 at ~900 ^oC was reported.

More recently, it has been suggested that modulation doping in nanocomposites can improve the power factor by increasing the charge-carrier mobility.[30] The modulation-doped bulk sample consists of two different types of nanograins: one is the doped nanograin and the other is the undoped or lightly doped matrix phase. As compared to the heavy uniform doping in TE materials, the ionized nanoparticles can be spatially placed much further apart in the modulation-doping scheme.[31] The goal of this approach is to improve the electron mobility via the reduction of electron-impurity scattering. This approach has been used in several material systems, such as SiGe[30,31] and BiCuSeO[32], and the *ZT* values are found to be enhanced by about 30% as compared to the uniformly doped samples.

1.2.2 Band engineering in TE materials

According to the Mott relation, the Seebeck coefficient of a metal can be expressed as[33]

$$S = \frac{\pi^2 k_B^2 T}{3e}\left(\frac{d\ln\sigma(E)}{dE}\right)\Bigg|_{E=E_F} = \frac{\pi^2 k_B^2 T}{3e}\left(\frac{1}{n}\frac{dn(E)}{dE} + \frac{1}{\mu}\frac{d\mu(E)}{dE}\right)\Bigg|_{E=E_F}, \qquad (1.25)$$

where k_B is the Plank constant, e is the electron charge, E is the electron energy, E_F is the Fermi energy, and $n(E)$ and $\mu(E)$ are the energy dependent carrier density and mobility, respectively. Thus, the Seebeck coefficient can be improved by band engineering, i.e. increasing the density of states near the Fermi level[34] or by increasing band degeneracy via temperature assisted band convergence[35]. Resonant impurities have been shown to increase the density of states near the Fermi level and thus the *ZT* values of TE materials.[36] Heremans *et al.*[34] reported an enhanced Seebeck coefficient in PbTe through the use of thallium resonant impurity levels, which led to a doubling of *ZT* to above 1.5 at 773 K. Such resonant-level doping was also reported for the tin-doped Bi_2Te_3[37] and indium-doped SnTe[38]. Besides introducing the resonant impurity level, a large valley degeneracy in the electronic bands is also beneficial to high *ZT*. Pei *et al.*[35] reported a convergence of at least 12 valleys in doped $PbTe_{1-x}Se_x$ alloys, and achieved a peak *ZT* of 1.8 at about 850 K. Moreover, Liu *et al.*[39] found the peak *ZT* of $Mg_2Si_{1-x}Sn_x$ solid solutions can be improved to 1.3 near 700 K due to an enhanced density-of-states effective mass as a result of the increased valley degeneracy as the two conduction bands cross.

1.2.3 TE materials with complex crystal structures

Semiconductors with complex crystal structures possess intrinsically low lattice thermal conductivity, and have been studied as promising TE materials.[40] In a crystal

with a large and complex unit cell, the majority of the phonon modes are optical modes, which possess low group velocities and thus make little contribution to the thermal conductivity.[41] In 1995, Slack proposed that good TE materials should have phonon-glass, electron-crystal (PGEC) properties.[42] This PGEC behavior was first pursued in crystalline clathrates and skutterudites where the well-defined host framework structure results in a good electrical conductivity and weakly bound guest atoms leads to a poor lattice thermal conductivity.[43] The inelastic neutron scattering measurements on the $Ba_8Ga_{16}Ge_{30}$ sample[44] further indicated that the group velocity of the acoustic modes are reduced due to the presence of the avoided crossing of the rattler mode.

The Zintl phase, $Yb_{14}MnSb_{11}$ was also found to be a good TE material at high temperature.[45] As compared to SiGe alloy, $Yb_{14}MnSb_{11}$ shows much lower thermal conductivity, which is between 0.7 and 0.9 W m^{-1} K^{-1} for the temperature of 300-1275 K. Thus, a higher peak *ZT* of ~1.0 is achieved at 1200 K without nanostructuring. The crystal structure of $Yb_{14}MnSb_{11}$ consists of a variety of distinct structural units, including $[Sb_3]^{7-}$ trimers, $[MnSb_4]^{9-}$ tetrahedra and isolated Sb anions. These various sites allow for the potential tuning of the transport properties by doping. Doping on the Yb site can tune carrier concentration and increase scattering of phonon; while doping on the Mn allows for possible adjustment of the electronic parameters. For example, $Yb_{14}Mn_{1-x}Al_xSb_{11}$ undergoes a metal-insulator transition, resulting in an increased Seebeck coefficient and thus an improved peak *ZT* of 1.3 at 1223 K.[46]

Glass-like thermal conductivity, which is about 0.46 W m^{-1} K^{-1} at 500 K, is also seen in the thermoelectric compound of β-Zn_4Sb_3.[47,48] The single-crystal X-ray and powder-synchrotron-radiation study[49] indicate the crystal structure contains disordered Zn interstitial sites. Furthermore, local ordering of Zn interstitials into nanoscale domains with size less than10 nm were found by the pair distribution function analysis of X-ray

and neutron diffraction results.[50] These disorders at multiple length scales account for the low thermal conductivity of β-Zn_4Sb_3.

Copper selenide, Cu_2Se, was recently realized as a promising TE material with a peak *ZT* of 1.5 at 1000 K.[51] The Cu-Se system undergoes a phase transition at about 400 K from a low-temperature α phase to a high-temperature β phase. The high-temperature β phase shows a significant Cu deficiency in which the Se atoms form a simple face-centered cubic structure and Cu ions are highly disordered with superionic liquid-like mobility. The low-temperature α phase has a lower symmetry crystal structure with localized Cu atoms. The superionic mobility of the Cu atoms has been proposed to be the origin of the unusually low κ_L of Cu_2Se.[51] The fluid arrangement of Cu atoms inhibits the propagation of the transverse phonon waves and disrupts heat transport by phonons, resulting in a lower specific heat since the specific heat is related to the excitation of lattice vibrations. Moreover, the partial liquid behavior also contributes to extra scattering of phonons. In addition, it is reported that a higher *ZT* of 2.3 can be reached at a phase transition temperature (400 K) by utilizing critical electron and phonon scattering, which is associated with the crystal structures of two phases and the structure variation during phase transitions.[52] The phase transition temperature can be changed by iodine substitution for Se.

1.3 CRYSTAL STRUCTURE AND PHYSICAL PROPERTIES OF HIGHER MANGANESE SILICIDES

The use of environmentally-friendly and low-cost materials made of abundant elements is necessary for large-scale adoption of TE devices for vehicle waste heat recovery and other applications. Thus increasing interest has been drawn to a class of silicides materials recently. Semiconducting silicides, such as higher manganese silicides

(HMS), Mg_2Si, $CrSi_2$, β-$FeSi_2$, $ReSi_{1.75}$ and Ru_2Si_3, have been found to show promising TE performance.[39,53-57] Among them, the *n*-type $Mg_2Si_xSn_{1-x}$ shows very high *ZT* values of ~1.3 at ~700 K.[39] However, the *ZT* of *p*-type silicides is not very high, and is about ~0.7 for HMS. Hence, there is a need to further improve the TE properties of *p*-type silicides.

1.3.1 Nowotny chimney ladder structure and microstructure of HMS

Higher manganese silicides, Mn_nSi_{2n-m}, are promising *p*-type TE materials for waste heat recovery due to the abundance of the constituent elements, environmental friendliness, and good thermal and chemical stability. HMS crystallize into the Nowotny chimney ladder (NCL) structure,[58] in which the unit cell consists of a tetragonal Mn chimney sublattice based on the β-Sn structure and a Si ladder sublattice with the atomic arrangement of coupled helices.[59] Each commensurate Mn_nSi_{2n-m} structure contains an integral number (n) of Mn sublattices and another integral number (m) of Si sublattices in one crystallographic unit cell, i.e.: $c = nc_{Mn} = mc_{Si}$, where c, c_{Mn} and c_{Si} are lattice constants along the *c* axis for the HMS primitive cell, Mn sublattice, and Si sublattice, respectively. The crystal structures of four distinct phases have been reported with atomic position determined by X-ray diffraction, including the commensurate Mn_4Si_7,[60] $Mn_{11}Si_{19}$,[61] $Mn_{15}Si_{26}$,[62] and $Mn_{27}Si_{47}$[63] phases shown in Figure 1.2. Each HMS phase exhibits a nearly identical *a* lattice parameter (a = 5.51 Å) and atomic ratio, but varying *c* lattice parameters, which can range from about 17 Å for Mn_4Si_7 to as long as 118 Å for $Mn_{27}Si_{47}$, as listed in Table 1.1.

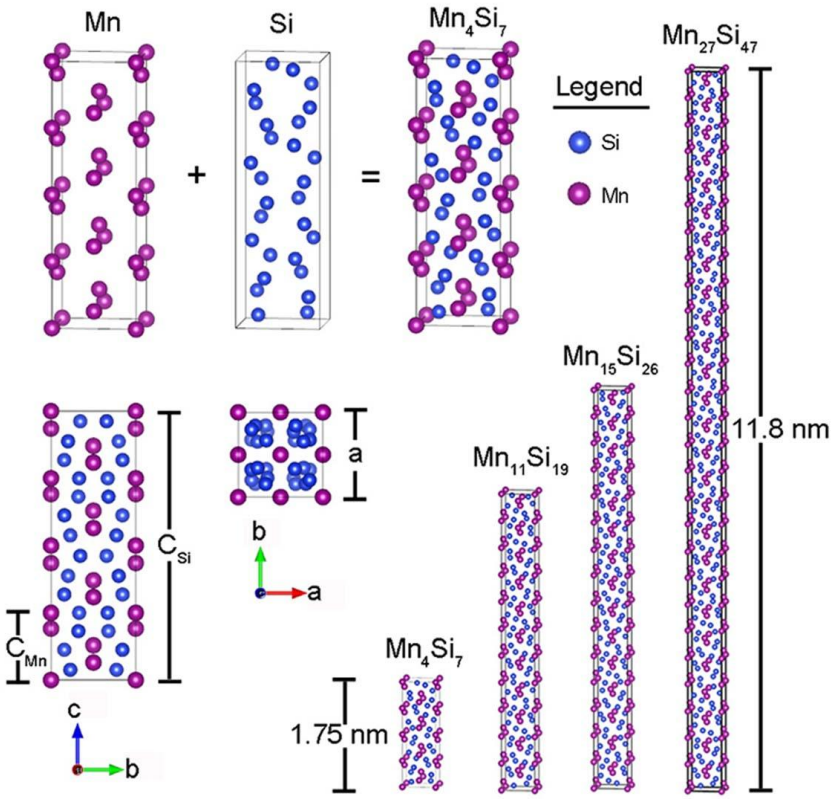

Figure 1.2: Nowotny chimney ladder structure of HMS.

Table 1.1: Lattice parameters and space groups of four HMS phases.[59]

HMS	N_{Si}/N_{Mn}	*a*, *b* (Å)	*c* (Å)	Space group
Mn_4Si_7	1.75	5.525	17.463	P-4c2
$Mn_{11}Si_{19}$	1.727	5.518	48.136	P-4n2
$Mn_{15}Si_{26}$	1.733	5.531	65.311	I-42d
$Mn_{27}Si_{47}$	1.741	5.53	117.9	P-4n2

Miyazaki *et al.*[64] have studied the crystal structure of HMS by the means of the (3+1)-dimensional superspace group approach. The refined atomic positions revealed in-plane rotational modulation in Si sublattice and positional modulation in Mn sublattice

along the *c* axis. Figure 5 of their paper[64] shows the interatomic distances as a function of the internal coordinate *t* in their study. The nearest Mn-Mn distances do not change significantly while the Mn-Si and Si-Si distances show a periodic alternation. It is found that one Mn atom is always bounded to eight Si atoms with a distance less than 2.8 Å.

According to the phase diagram of the Mn-Si binary system,[65] if a liquid mixture of Mn:Si = 1:1.75 is cooled from temperature higher than ~1440 K, MnSi starts to appear and the Si concentration in the liquid phase increases when the mixture reaches the liquidus line. At 1428 K, MnSi and the melt mixture react to form $MnSi_{\sim 1.75}$. The growth of $MnSi_{\sim 1.75}$ proceeds by a peritectic reaction ($MnSi+Si \rightarrow MnSi_{\sim 1.75}$), whose speed depends on the diffusion speed of the supplied Si.[66] Therefore, a secondary phase of MnSi naturally forms during the melt growth of HMS. Layers of the minority MnSi phase were found to inherently segregate perpendicular to the *c*-axis of HMS.[53,59] Transmission electron microscopy (TEM) study of HMS indicates that the Mn and Si sublattices are incommensurate and a strictly commensurate phase does not exist.[67,68] It is found that this structure exhibits a particular type of disorder. The spacing and orientation anomalies[68] have been observed in electron diffraction patterns. Incommensurate crystal growth from Mn:Si = 1:1.75 is hereinafter referred to a HMS.

1.3.2 Band structures of HMS

The HMS compounds are found to have a direct band gap of ~0.7 eV and an indirect band gap of ~0.4 eV at room temperature according to optical property measurements.[69-71] These features have led to the synthesis of HMS thin films and studies of their potential use in optoelectronics.[72]

Migas *et al.*[14] have investigated the electronic band structures of four different HMS phases, including Mn_4Si_7, $Mn_{11}Si_{19}$, $Mn_{15}Si_{26}$, and $Mn_{27}Si_{47}$, using first principles

calculations. They found that Mn_4Si_7 is a semiconductor with the Fermi level in the band gap. Mn_4Si_7 has an indirect band gap of 0.77 eV and a direct band gap of 0.79 eV. However, $Mn_{11}Si_{19}$, $Mn_{15}Si_{26}$, and $Mn_{27}Si_{47}$ behave like degenerate *p*-type semiconductors since the Fermi level stays in the top of the valence band. These three phases are found to have an energy gap of 0.78 eV, while the Fermi level lies 0.05-0.07 eV below the top of the valence band. In addition, the calculations suggest that the band structures change significantly by introducing stacking faults, which leads to a reduction of the band gap.

1.3.3 Synthesis of HMS materials

HMS single crystals prepared by the Bridgman method or Czochralski method possess anisotropic electrical and thermal transport properties, which is related to the complex NCL structure and the layers of secondary MnSi phase precipitating perpendicular the *c* axis.[59,66] For example, the κ_L along the *c* axis is approximately half of that along the *a* axis at room temperature. The molten metal flux method has also been used to synthesize HMS single crystals.[73,74] Ga or Sn was used as a flux to produce HMS single crystals of several mm^3. Recently, high-purity MnSi-free single crystals of HMS were prepared by the chemical vapor transport method.[75] However, it is difficult to measure all three TE properties of these samples due to their small size.

Polycrystalline HMS samples have been prepared by melting, solid-state reaction or mechanical alloying.[76-79] The lattice thermal conductivity of polycrystalline HMS samples can be suppressed due to increased grain boundary scattering. HMS thin film have also been prepared by epitaxial growth on a Si substrate, and studied for their potential use for optoelectronic application.[69-72] Moreover, HMS nanowires have recently been synthesized by the chemical vapor deposition[80] of the single-source precursor

$Mn(CO)_5SiCl_3$ or vapor phase conversion from Si nanorewire arrays[81]. The electrical transport properties of HMS nanowires were measured with single nanowire devices fabricated via standard electron beam lithography techniques. The electrical resistivity of these nanowires is about 20 mΩ·cm, which is comparable to HMS thin film and bulk samples.

1.4 OVERVIEW ON RECENT INVESTIGATIONS OF HMS MATERIALS

In the past two decades, the studies on HMS bulk materials have been focused on tuning the transport properties by chemical substitutions. Several dopants, such as Ru, Fe, Cr, Ge, and Al,[66,78,82-86] have been employed to tune the transport properties of HMS and the maximum *ZT* has been enhanced up to ~0.7 at 800 K. In addition, it has been found that the morphology of the secondary MnSi phase changes with doping level. Aoyama et al.[66] investigated the effect of Ge doping on the morphology of MnSi in HMS single crystals, and observed an initial increase and then decrease of MnSi volume concentration, which was correlated to the change of TE properties. Zhou *et al.*[86] further studied the microstructure and TE properties of Ge-doped HMS polycrystals prepared by induction melting followed by hot-pressing. They found that the number of MnSi layers is reduced remarkably at higher Ge content; Meanwhile, the MnSi layers became more curved and nonparallel to each other. Besides these experimental studies, density functional theory calculations have also been used to evaluate the doping effects on the electronic transport properties of HMS.[87] The calculated Seebeck coefficient is increased in In and Tl-doped HMS due to the high *d*-states contribution in the density of states at the Fermi level.

Nanostructuring has been explored recently in an attempt to reduce the κ_L of HMS.[76,80,81,88-95] Norouzzadeh *et al.*[90] estimated the effect of grain size on thermoelectric transport properties of HMS. A semi-classical two-band model and a Debye model have been used to characterize the charge carrier and phonon transport, respectively. Their calculations indicate that the *ZT* values cannot be improved significantly by reducing the grain size due to a remarkable loss of electrical conductivity. Moreover, some efforts have also been devoted to make HMS nanocomposites. Zhou *et al.*[88] have first prepared HMS/PbTe and HMS/Ag_2Te nanocomposites by mechanical mixing and hot-pressing, and observed a reduction of lattice thermal conductivity. However, the *ZT* values were decreased because of the much lower power factor. *ZT* improvement was later found in HMS samples with other secondary phases, such as HMS/MnSi,[89] HMS/carbon nanotubes,[92] and HMS/Yb composites.[93] Despite the reduction of κ_L in these nanocomposites, their *ZT* values still do not exceed 0.7.

The phase transformations in HMS have been studied by several groups based on X-ray diffraction (XRD) and differential scanning calorimetry.[96-98] All of them found that the intensity of the MnSi peaks increase significantly at a temperature near 800 ^{o}C, which is believed to be caused by a phase transformation of the HMS. Zhou *et al.*[96] have investigated the grain size effect on the phase transformation of HMS and found that nanostructured HMS shows more remarkable and accelerated transformation compared to that in the micropowders. Kikuchi *et al.*[97] have used the high temperature XRD to study HMS with a (3+1)-dimensional superspace approach. Refined *a* and c_{Mn} values increase linearly and the thermal expansion coefficients are comparable with those of typical metallic electrode materials. In contrast, c_{Si} changes its slope at ~773 K, which corresponds to the temperature wherein the bipolar effect starts.

Despite the above progress made in the study of HMS, there have remained a number of outstanding questions. First, the origin of the low and anisotropic thermal conductivity of HMS crystals has so far been elusive. Secondary, it is of interest to study whether the low thermal conductivity can be further suppressed either by grain-boundary scattering or alloy scattering. However, the phonon dispersion of HMS, which is indispensable for understanding thermal transport, has remained unknown. In addition, the optimum carrier concentration level for HMS has not been reported yet.

1.5 OBJECTIVE AND ORGANIZATION OF THIS DISSERTATION

The overall goal of this work is to establish a better understanding of the structure-thermoelectric property relationship of HMS with a complex crystal structure. By measuring the phonon dispersion and thermoelectric properties of HMS, this research aims to address several outstanding questions on the effects of crystal structure on the phonon and electron transport behaviors in HMS, and to explore methods to improve the *ZT* of HMS. The specific objectives include

(1) Understanding the origin of low and anisotropic thermal conductivities of HMS crystals by examining the phonon dispersion and scattering processes in HMS single crystal via inelastic neutron scattering and thermal transport measurements.

(2) Investigation of doping and nanostructuring as two approaches to enhance the TE performance of polycrystalline HMS and establish the structure-property relationship.

The organization of the dissertation is the following. Chapter 2 describes the experimental results of phonon dispersion of HMS crystals with focus on the discovery of

a low-energy twisting polarization. Chapter 3 addresses the effects of (Al,Ge) double doping on the microstructure and thermoelectric properties of HMS. Chapter 4 reports that the minimum thermal conductivity can be approached in Re-substituted HMS. Chapter 5 discusses the effects of nanostructuring, especially the grain size effect, on the thermoelectric properties of HMS. The major findings of this dissertation are summarized in Chapter 6.

Chapter 2: Phonon dispersion of higher manganese silicide

2.1 Introduction

The Nowotny chimney ladder (NCL) phases are a class of materials characterized by a uniquely complex structure composed of two interlocking sublattices. The structures are derived from transition metal elements from group 4-9, which form a tetragonal, 'chimney' sublattice, and main group elements from group 13-15, which likewise forms helical "ladders" embedded within the transition metal chimneys.[80,99,100] A prominent example of NCL phases are the HMS, which consist of a tetragonal Mn chimney sublattice and a Si helices.[59] The phases of HMS are characterized by both local disorder and long range ordering and sit at the transition from an ordered crystal to a disordered system.

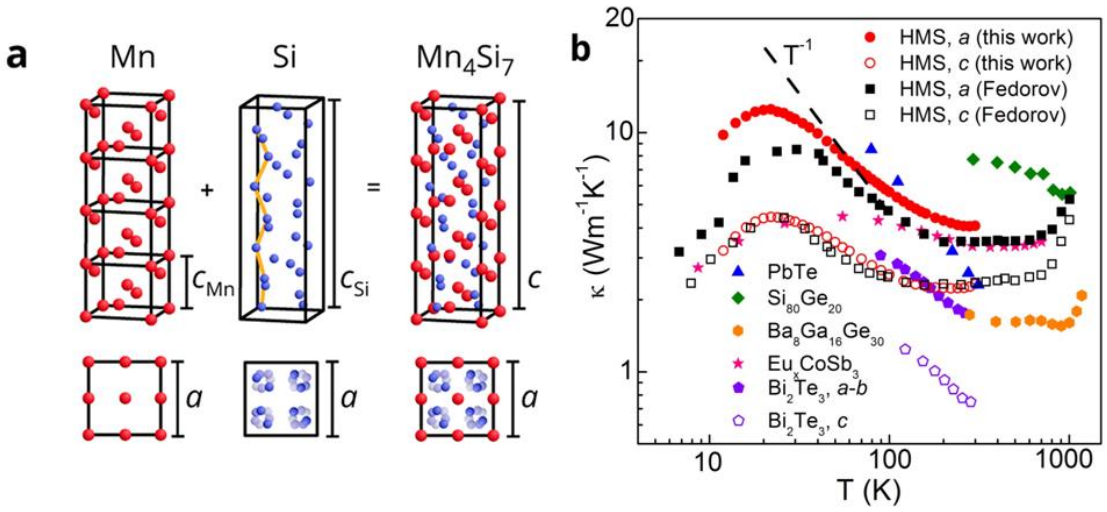

Figure 2.1: (a) Schematic illustrations of the crystal structure of Mn_4Si_7. (b) Temperature-dependent thermal conductivities of the HMS crystal measured in this work along the *c* and *a* axes. Shown for comparison are the reported thermal conductivity data of HMS [59], Bi_2Te_3 [101], PbTe [102], and $Ba_8Ga_{16}Ge_{30}$ [103] crystals, and $Si_{80}Ge_{20}$ [104] and Eu_xCoSb_3 [105] alloys.

One of the outstanding questions on HMS concerns the relationship between the complex NCL structure and the low and anisotropic thermal conductivity. As shown in Figure 2.1b in comparison with other TE materials,[59,101-105] the thermal conductivity of HMS along the Si ladder direction (*c* axis) can be a factor of two lower than that perpendicular to the ladder (*a* axis). This κ anisotropy is similar in magnitude to layered Bi_2Te_3, where the heavy atoms are responsible for the inherently low κ and the large bonding anisotropy is responsible for the κ anisotropy.[10] As the bonding energy in HMS is not nearly as anisotropic as that in Bi_2Te_3, the reason for the κ anisotropy in HMS remains unclear. It has been suggested that low κ_L can be achieved in crystals with a large and complex unit cell because a large fraction of the phonon modes are optical modes with small group velocities and thus make little contributions to κ_L.[41,106] However, the actual phonon dispersion, which is indispensable for understanding thermal transport, has remained unknown for HMS.

Recently, Natalio Mingo's group at Commissariat à l'Énergie Atomique Grenoble and Derek A. Stewart's group at Cornell University conducted density functional theory (DFT) calculations of the phonon dispersion and electronic band structure of Mn_4Si_7.[107] Figure 2.2 shows the calculated full phonon dispersion along the two principal axes of Mn_4Si_7, [00*L*] and [*H*00], the latter of which is equivalent to [0*K*0]. The calculation results reveal numerous flat optical branches with energy as low as about 10 meV. The polarizations of the calculated phonon branches are determined and shown in Figure 2.2c and d.

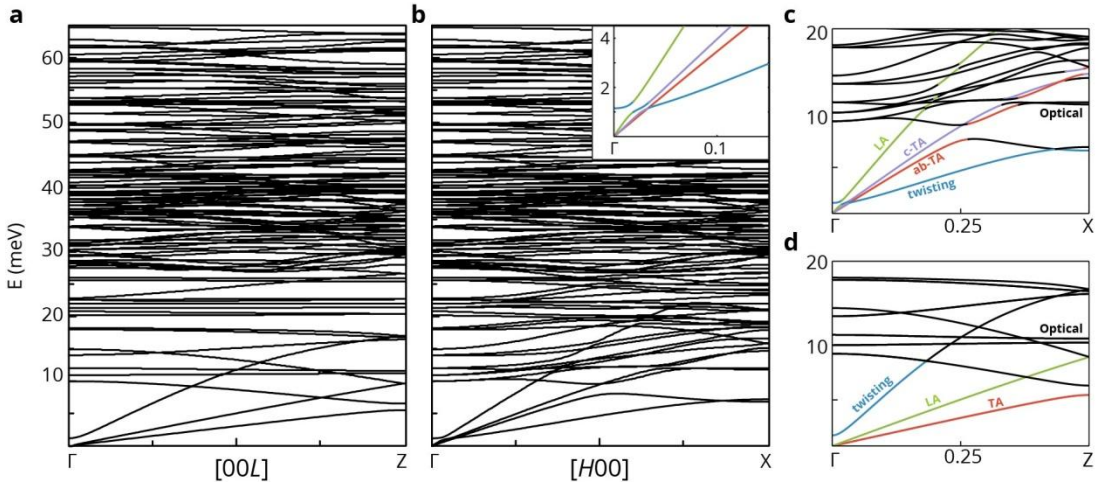

Figure 2.2: Calculated phonon dispersion of Mn_4Si_7.[107] (a), (b) Calculated harmonic dispersions of Mn_4Si_7. (c), (d) The calculated low energy harmonic dispersions indexed by the polarization as LA, TA, twisting, or other optical modes. The inset to (b) shows the modes close to the avoided crossing at ~1 meV along the Γ-X direction, with the color coding of the modes the same as that in (c).

A significant finding from the calculation results is the discovery of the lowest-lying optical (LLO) polarization with energy comparable to the three acoustic polarizations. The atomic motions of the LLO polarization correspond to a twisting motion of the Si atoms and a nearly stationary Mn sublattice with minor translations along the *c* axis. Such twisting modes are commonly associated with quasi-1D structures such as single-walled carbon nanotubes[35], where they are purely acoustic modes. In the case of the Si helices interacting with adjacent helices and the Mn chimneys in the three-dimensional HMS structure, the twisting polarization is an optical branch with a nonzero energy of 0.8 meV at the zone center, according to the calculation results shown in the inset of Figure 2.2b. In addition, because of the anisotropic structure, the calculation

results show that the two transverse acoustic (TA) polarizations are degenerate along [00*L*] but slightly non-degenerate along [*H*00] and [0*K*0].

The twisting polarization is the lowest energy polarization along [*H*00] and [0*K*0] except near the zone center, where it undergoes two consecutive avoided crossings with the longitudinal acoustic (LA) and *c*-polarized TA branches at a very low energy of about 1.4 meV, as illustrated in the inset of Figure 2.2b. In addition, the calculation suggests another avoided crossing of the *a*-*b* polarized TA branch and an optical branch near $E = 9$ meV and $\boldsymbol{q} = 0.25(2\pi/a)$ (Figure 2.2c). Indicating a similar symmetry in the displacement patterns of two hybridized modes, avoided crossings of this kind have been observed between the rattler mode and acoustic modes in the clathrate $Ba_8Ga_{16}Ge_{30}$,[44] where the low κ has been attributed to both the presence of many flat optical branches associated with the large unit cell, and by the flattening of the acoustic modes from the presence of the rattler mode.

This chapter presents an experimental effort to obtain the phonon dispersion of HMS so as to verify the theoretical calculation results. The HMS crystals were prepared by the Bridgeman method. The phase, microstructures, and TE properties of the HMS crystal were studied in detail. The phonon dispersion was measured by inelastic neutron scattering, and the results were compared with the calculated phonon dispersion of the Mn_4Si_7 phase. In addition, the phonon density of states and specific heat of HMS were also investigated.

2.2 EXPERIMENTAL METHODS

2.2.1 Materials synthesis and characterization

A crystal sample of HMS was grown by melting the powder sample via the Bridgman method. The starting materials, Mn (purity, 99.95%) and Si (purity, 99.999%) powders, were purchased from Alfa Aesar. The powders with nominal chemical composition $MnSi_{1.8}$ were weighed, and then hand-ground with an agate mortar and pestle for 1 h. Subsequently, the powders were sealed in a vacuumed quartz tube. The quartz tube was placed in a furnace and sintered at 900 ^{o}C for 48 h. The as-sintered powder was loaded into a quartz tube, and the tube was loaded into an infrared (IR)-heating image furnace (model SC-M35H, NEC Nichiden Machinery) with 2 × 1500 W halogen lamps. The tube rotated at a rate of 20 rpm and traveled through the hot zone at a rate of 10 mm/h. The crystal structure of the HMS samples was characterized via X-ray powder diffraction (XRD) with a Phillips X'pert diffractometer and the Cu K_{α} radiation on the powder sample made by crushing an HMS crystal. The morphology and chemical compositions of finely-polished HMS samples were analyzed with a Quanta 650 environmental scanning electron microscope (SEM) with an energy-dispersive X-ray (EDX) spectrometer. Transmission electron microscopy (TEM), high-resolution TEM (HRTEM), and selected area electron diffraction (SAED) of the samples were performed in a FEI Titan aberration-corrected scanning TEM electron microscope. The low-temperature thermal conductivity was measured by a steady-state method. The temperature dependent specific heat data were collected using a 14 Tesla Quantum Design Physical Properties Measurement System in the temperature interval 1.9 K $\leq$ T $\leq$ 300 K. Raman measurements were performed on a HMS crystal sample with 532 nm laser excitation focused through a 100× objective lens (WiTec Alpha300). The far infrared (IR) absorption measurements were obtained at room temperature with a Fourier

transform infrared (FT-IR) Spectrometer (Nicolet iS50R). Measurements were taken on a polyethylene pellet of 20 mm diameter. The pellets were prepared by mixing 15 mg of sample with 1 g of polyethylene.

2.2.2 Neutron scattering

Neutron scattering measurements were conducted with the Wide Angular-Range Chopper Spectrometer (ARCS) at the Spallation Neutron Source at Oak Ridge National Laboratory (ORNL). The measurements were carried out together with Olivier Delaire from ORNL and Annie Weathers from UT Austin. The incident neutron energy was 40 or 30 meV with the sample maintained at room temperature and the beam incident on an HMS crystal mounted with the (*H*,*K*,0) crystallographic plane horizontal to the beam. Additional measurements were performed with the triple-axis spectrometer (HB1) at the High-Flux Isotope Reactor (HFIR), ORNL. We used a pyrolitic graphite monochromator and analyzer [in the (0,0,2) reflection condition], and worked in constant final energy mode, with E_f = 13.5 meV. The horizontal collimation angles were 48, 80, 80, and 240 minutes of arc for the Soller collimators prior to the monochromator, between monochromator and sample, between samples and analyzer, and between analyzer and detector, respectively. The sample was mounted with the (*H*,*K*,0) plane approximately horizontal, and data was collected at T = 300 K. The phonon peaks were extracted from the constant-$\boldsymbol{q}$ or constant-*E* scans by Gaussian fitting. The phonon DOS of a powder sample synthesized by solid-state reaction was measured with ARCS.

2.3 Synthesis and TE properties of HMS crystals

An HMS crystal rod with approximately 6 mm diameter and 10 mm length was grown by the Bridgman method. It has been reported that local variations of the HMS

structure exist due to the incommensurate nature of Nowotny Chimney Ladder phases.[67,108] Therefore, the XRD results (Figure 2.3) obtained on the powder sample crushed from a HMS crystal may consist of contributions from different phases. The main phase of our HMS crystal can be indexed with the structural model of the $Mn_{27}Si_{47}$ phase with the space group $P\bar{4}n2$.

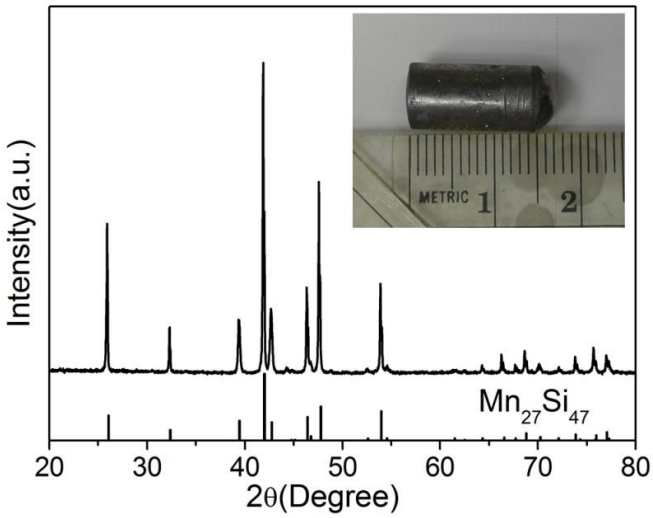

Figure 2.3: X-ray powder diffraction pattern of the pulverized HMS single crystal in this work. The inset shows a photograph of HMS single crystal prepared by the Bridgeman method.

As shown in Figure 2.4a, scanning electron microscopy (SEM) measurements reveal the presence of metallic MnSi lamellae, approximately 600 nm wide and spaced ~20 μm apart, which precipitate perpendicular to the *c* axis.[10] The presence of the MnSi phase has previously been reported in crystalline HMS samples, [10,12] and is caused by a peritectic decomposition of HMS. In order to better understand the crystal structure, a transmission electron microscopy (TEM) study of our HMS crystal sample was performed by Song Jin's group at University of Wisconsin-Madison. The high-resolution TEM (Figure 2.4b) shows modulated lattice fringes that are characteristics of the NCL

superlattice.[68,80] The corresponding selected-area electron diffraction (SAED) pattern (Figure 2.4c) reveals parallel arrays of closely packed satellite peaks aligned along [001]. Each bright "basic" spot due to the diffraction from the Mn sublattice is superimposed with a series of more closely spaced "satellite" spots due to the larger *c* axis of Si sublattice. Usually, the sequences of satellites associated with different basic spots do not match where they meet. In addition, the sequences of satellites may have directions which enclose a small angle with the direction of the basic spots.[68] Such spacing and orientation anomalies have also been observed in our samples. In addition, the satellite peaks are also discernible in the elastic neutron diffraction pattern shown in Figure 2.4d.

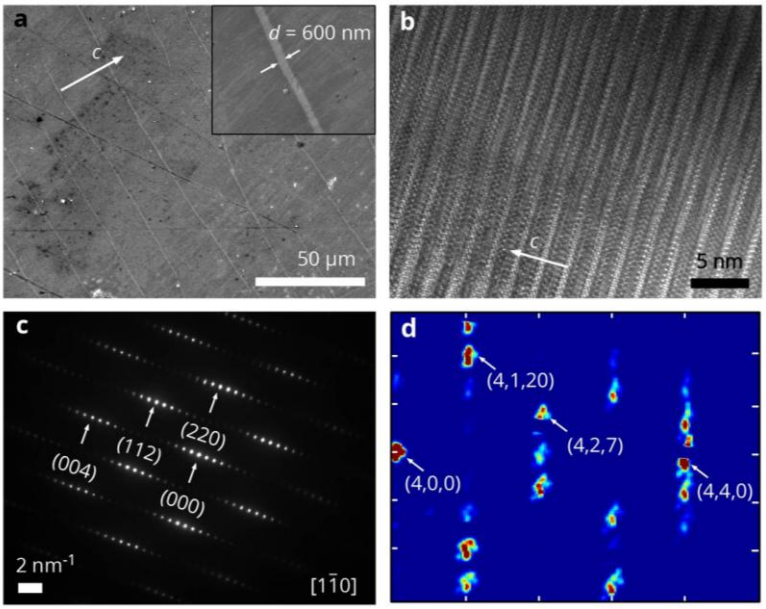

Figure 2.4: (a) Scanning electron microscopy (SEM) image of the HMS crystal synthesized in this work. (b) High-resolution transmission electron microscopy (HRTEM) lattice fringe image of the HMS region of the crystal. (c) Selected area electron diffraction (SAED) of the HMS crystal along the [1$\bar{1}$0] zone axis indexed with respect to the Mn sublattice. (d) Neutron diffraction pattern of the HMS crystal indexed with respect to the $Mn_{27}Si_{47}$ phase. In both (d**)** and (d), the Si sublattice of a long c_{Si} produces characteristic satellite reflections along the [001] direction of the HMS crystal.

The orientation and crystal quality were examined with Laue back reflection, as shown in Figure 2.5. Seebeck coefficient, electrical conductivity, and thermal conductivity were measured along the *a* axis and *c* axis, respectively. It is clear that all three TE properties show anisotropic behavior in the entire measured temperature range (Figure 2.6). The κ along the *c* axis is about twice lower than that along the *a* axis at room temperature. Moreover, one can see a typical temperature dependence determined by long-wave acoustic phonons with a maximum at about 20 K and an unusual plateau starting from about 130 K. In the range of the plateau, the thermal conductivity is low and deviates from the T^{-1} behavior shown by the thermal conductivity of simple crystals at high temperatures. The Seebeck coefficient is positive and increases linearly with increasing temperature, exhibiting the characteristics of a degenerate *p*-type semiconductor. The electrical conductivity decreases with increasing temperature, showing metallic behavior.

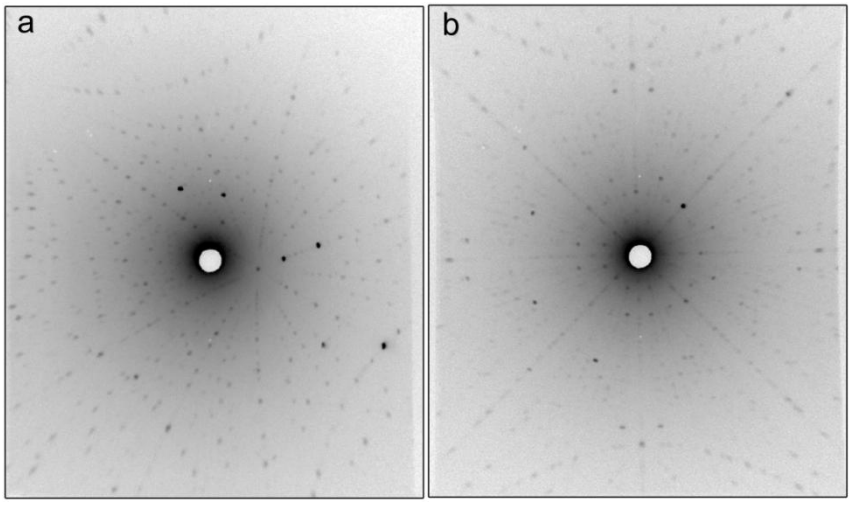

Figure 2.5: The Laue back reflection patterns of the HMS crystal (a) before and (b) after orienting along the *c* axis.

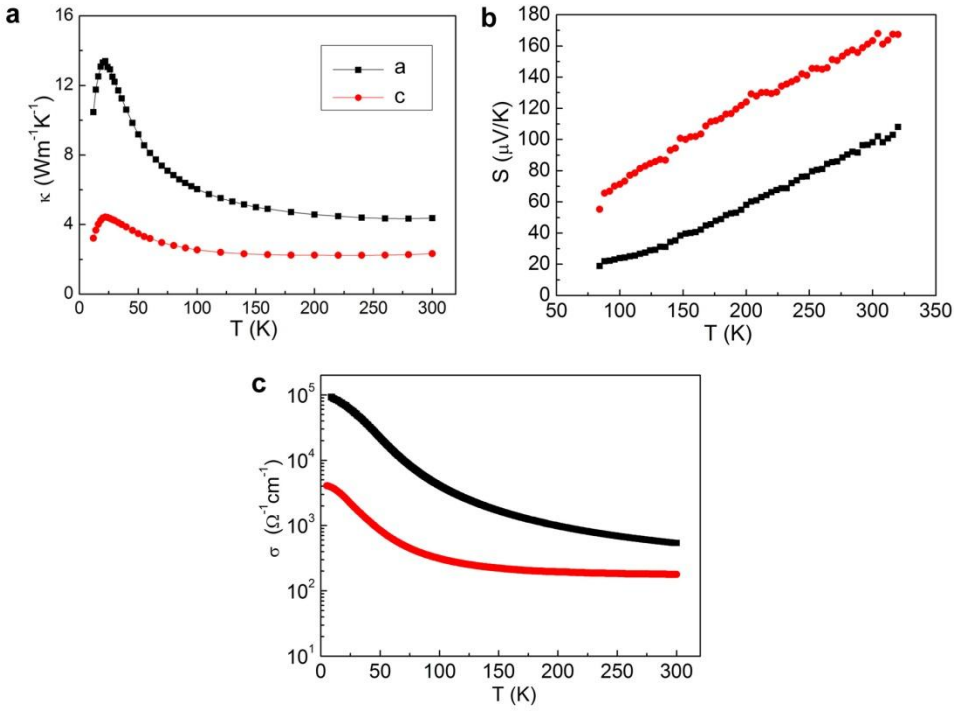

Figure 2.6: Thermoelectric transport properties of HMS single along the *a* and *c* axes: (a) thermal conductivity, (b) Seebeck coefficient, and (c) Electrical conductivity.

2.4 MEASURED PHONON DISPERSION OF HMS

INS measurements of the four-dimensional scattering function, $S(\boldsymbol{Q},E)$, were performed on an HMS crystal sample at 300 K with both a time-of-flight wide angular-range chopper spectrometer (ARCS)[109] and a triple-axis spectrometer. Figure 2.7 shows the experimental INS ARCS signal obtained from the HMS crystal with either 40 meV (Figure 2.7a, 2.7b, 2.7c) or 30 meV (Figure 2.7d, 2.7e, 2,7f) incident neutron energy along the phonon wave vector $\boldsymbol{q}$ = [*H*00], [0*K*0], and [00*L*] from different Brillouin zones, which are indexed by the reciprocal lattice vector $\boldsymbol{G_{HKL}}$ = (4,0,0), (4,2,0), (4,2,7), and $(4,1,\overline{20})$ with respect to the $Mn_{27}Si_{47}$ phase. The white solid lines in Figure 2.7 are the calculated harmonic dispersions of Mn_4Si_7. This simplest HMS phase (Figure 2.1a) has nearly seven times fewer atoms per unit cell than $Mn_{27}Si_{47}$, the majority phase

determined for our HMS samples, which would require orders of magnitude more computation time than for the Mn_4Si_7 phase. Nevertheless, the crystal structures of these two phases are still rather similar, except for minute differences in the Si ladder structure.

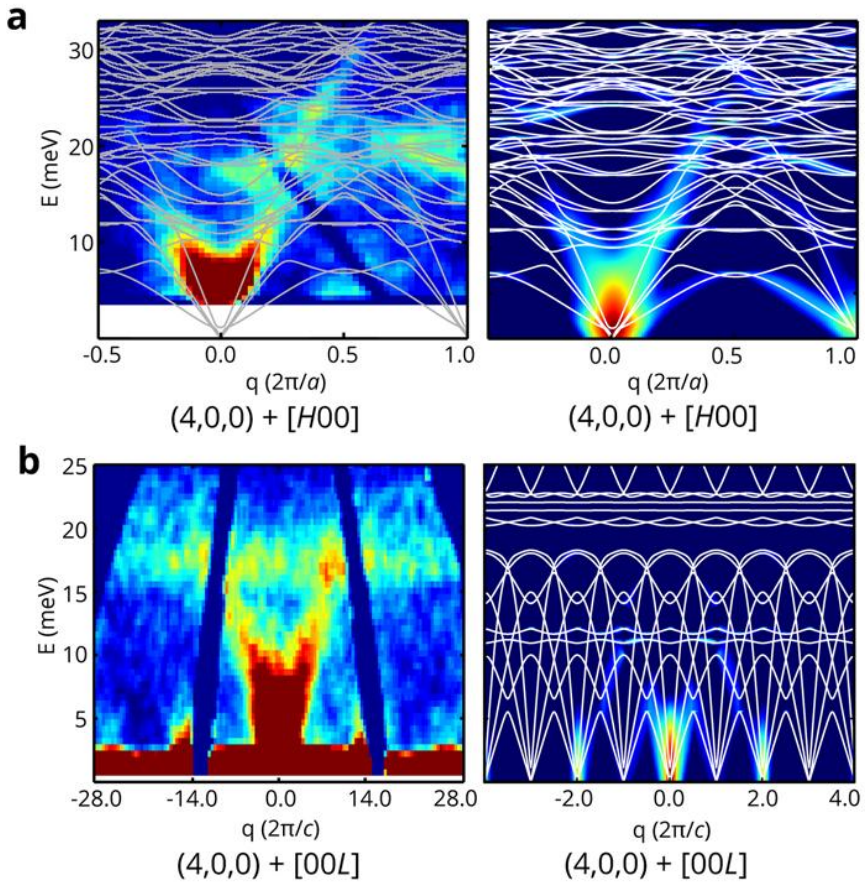

Figure 2.7 continued.

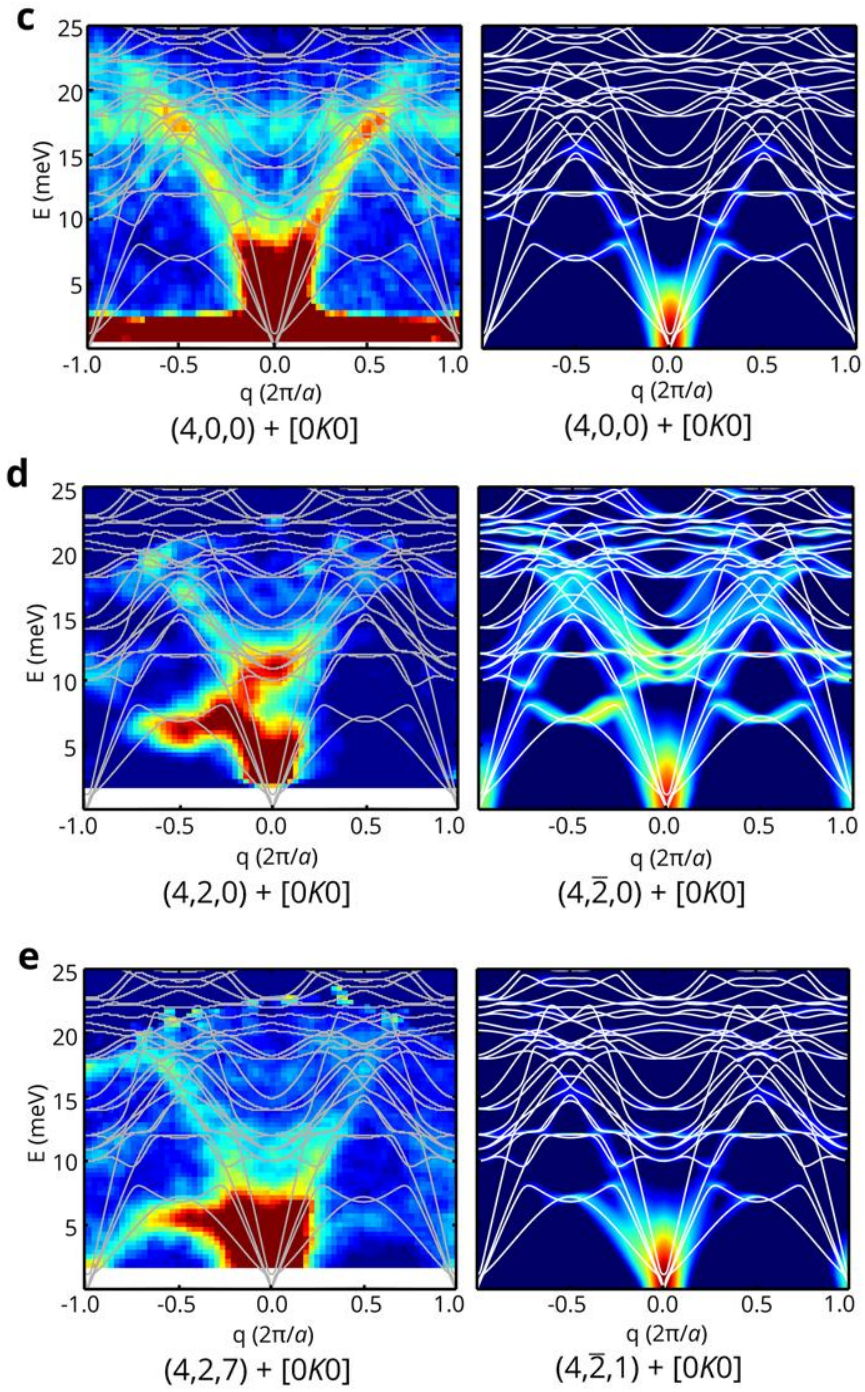

Figure 2.7 continued.

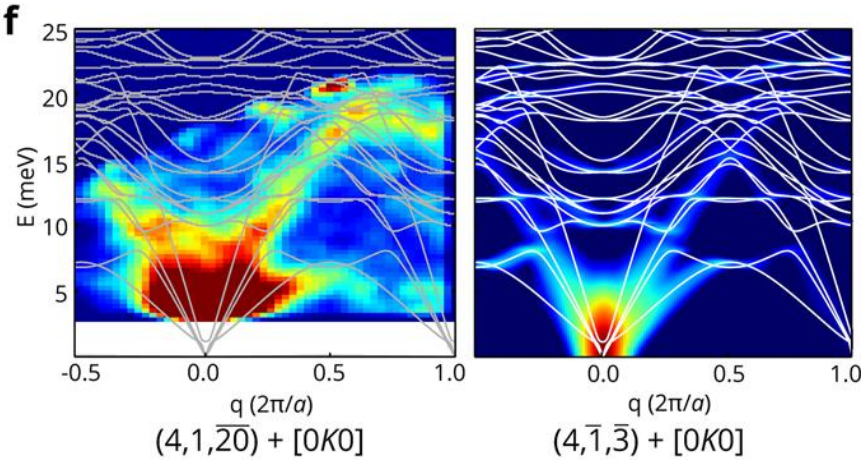

Figure 2.7: Measured INS (ARCS) signal in comparison with simulated dynamical structure factor for the HMS crystal at 300 K. $S(\boldsymbol{Q},E)$ data obtained by ARCS (on the left of each panel) for the HMS crystal and simulated dynamical structure factor (on the right of each panel) for Mn_4Si_7, (a**)** along [*H*00] in the (4,0,0) Brillouin zone, showing the LA and LO modes, (b) along [00*L*] in the (4,0,0) zone, showing mainly the TA and TO modes, (c) along [0*K*0] in the (4,0,0) zone, showing mainly the *a*-*b* polarized TA and TO modes, (d) along [0*K*0] in the (4,2,0) zone, showing mainly the *a*-*b* polarized TA and low lying optical modes, (e) along [0*K*0] in the (4,2,7) zone of $Mn_{27}Si_{47}$, showing the twisting and TA modes, and (f) along [0*K*0] in the $(4,1,\overline{20})$ zone of $Mn_{27}Si_{47}$, showing mainly the twisting and TA modes. The white solid lines in all figures are the calculated harmonic dispersions of Mn_4Si_7. Because m =1 and 7 for the Mn_4Si_7 and $Mn_{27}Si_{47}$ phases, respectively, the appropriate comparisons with the (4,2,7) and (4,1, $\overline{20}$) zones for $Mn_{27}Si_{47}$ are the (4,2,1) and $(4,1,\overline{3})$ zones for Mn_4Si_7. In addition, the simulations of the (4,2,0), (4,2,1) and $(4,1,\overline{3})$ exhibit a mirror reflection with respect to the experimental data along [0*K*0]. As such, Figure (d), (e) and (f) show the simulations of the $(4,\overline{2},0)$, $(4,\overline{2},1)$ and $(4,\overline{1},\overline{3})$ zones of Mn_4Si_7, the reason for this is still unclear.

For a net momentum transfer from the incident neutron of $\boldsymbol{Q} = \boldsymbol{G_{HKL}}+\boldsymbol{q}$, the measured neutron scattering intensity increases with $|\boldsymbol{Q}\cdot\boldsymbol{\varepsilon_i^{\alpha}}|^2$, where $\boldsymbol{\varepsilon_i^{\alpha}}$ is the polarization vector of the i^{th} atom in the unit cell for a particular phonon mode α. For a

net momentum transfer from the incident neutron of $\boldsymbol{Q} = \boldsymbol{G_{HKL}}+\boldsymbol{q}$, the measured neutron scattering intensity scales as

$$S(\boldsymbol{Q},E)\sim\sum_{\alpha}\frac{1}{E_{\alpha}}\,F_{\alpha}(\boldsymbol{Q},E)\times(n_{\alpha}+1)\;\delta(E-E_{\alpha})\;\delta(\boldsymbol{Q}-\boldsymbol{q}-\boldsymbol{G_{HKL}}) \tag{2.1a}$$

$$F_{\alpha}(\boldsymbol{Q},E)=\left|\sum_{i}\frac{b_i}{\sqrt{m_i}}e^{i\boldsymbol{Q}\cdot\boldsymbol{r_i}}e^{-W_i}\left(\boldsymbol{Q}\cdot\boldsymbol{\varepsilon}_{i,\alpha}\right)\right|^2. \tag{2.1b}$$

Here, α sums over all phonon modes in the Brillouin zone, i sums over all atoms in the Mn_4Si_7 unit cell, and b_i, m_i, r_i, and $\boldsymbol{\varepsilon}_{i,\alpha}$, are the coherent neutron scattering cross section, mass, atomic position, and polarization vector for atom i at mode α, respectively. The Bose-Einstein distribution, n_{α}, is taken at 300 K. The Debye-Waller factor, W_i, is equal to the thermally averaged displacement of the atoms from equilibrium.

Consequently, the neutron scattering intensity can vary considerably for phonons with the same $\boldsymbol{q}$ and α when measured in different Brillouin zones (different $\boldsymbol{G_{HKL}}$).These systematic variations can be analyzed to separate intensity contributed by longitudinal and transverse modes. For example, from the (4,0,0) zone along the [*H*00] direction (Figure 2.7a), $\boldsymbol{Q}$ = (4,0,0) + [*H*00] is parallel to the [*H*00] direction, which also happens to be the direction of the polarization vector of a longitudinal acoustic (LA) mode. Therefore, the product $\boldsymbol{Q}\cdot\boldsymbol{\varepsilon_i}$ in equation (2.1) ensures that only LA modes are visible from the zone along this direction. Likewise, in Figure 2.7c, $\boldsymbol{Q}$ = (4,0,0) + [0*K*0] is dominated by the component along the [*H*00] direction, with a small contribution along [0*K*0]. Along this direction the polarization vector for the *a*-*b* polarized transverse acoustic (TA) mode points along [*H*00], while the polarization vector for the LA mode points along [0*K*0]. Therefore, in Figure 2.7c, we expect to see the largest contribution from the *a*-*b* polarized TA mode. As we increase the component of $\boldsymbol{Q}$ along the *c* axis

towards the (4,2,7) and $(4,1,\overline{20})$ zones, we obtain a non-zero dot product between $\boldsymbol{Q}$ and the *c*-polarized TA mode along [0*K*0].

For all three crystal directions in the (4,0,0) zone, the INS data show both the presence of approximately linear acoustic branches and flat optical branches. The flat optical branches appear in the energy (*E*) range between 10 and 25 meV, which is rather low compared to an optical phonon energy of ~40 meV in Si.[110] Along [*H*00] (Figure 2.7a), the LA branch intercepts longitudinal optical (LO) branches about halfway between the zone center and zone boundary at ~15 meV. In comparison, Figure 2.7c shows that the *a*-*b* polarized TA branch along [0*K*0], extends to ~15 meV and intercepts the *a*-*b* polarized transverse optical (TO) branches near the zone boundary. Remarkably, a broad linear band along [00*L*] (Figure 2.7b) appears to extend to roughly $27\pi/c$ or π/c_{Mn}, the zone boundary of the Mn sublattice instead of that of Mn_nSi_{2n-m}.

As the component of $\boldsymbol{Q}$ in the *a*-*b* plane is increased towards the (4,2,0) zone (Figure 2.7d), the measurement data along [0*K*0], which is expected to contain mainly *a*-*b* polarized transverse polarizations, reveals another branch which bends down to about 6 meV at the zone boundary. As the component of $\boldsymbol{Q}$ along the *c* axis is increased towards the (4,2,7) zone, modes with polarizations in both the *a*-*b* plane and *c* axis can contribute to the measurement data along [0*K*0] and [*H*00], namely Figure 2.7e and Figure 2.8a, respectively, both of which clearly reveal an additional low energy branch extending to the zone boundary at roughly 5 meV. As the component of $\boldsymbol{Q}$ along the *c* axis increases further towards the $(4,1,\overline{20})$ zone so that the measurement data are increasingly sensitive to *c*-polarized modes, the measurement data along [0*K*0] mainly contain two branches, one similar to the low energy branch shown in Figure 2.7e and 2.8a and the other with energy close to the *a*-*b* polarized TA branch of Figure 2.7c.

We have further compared the experimental INS results with the simulated neutron scattering intensity (to the right of each panel in Figure 2.7) calculated by Natalio Mingo's group at Commissariat à l'Énergie Atomique Grenoble and Derek A. Stewart's group at Cornell University. In good agreement with the simulated results, the observed linear branch in Figure 2.7a is the LA polarization along [*H*00]. Similarly, the broad linear band observed in Figure 2.7b is due to TA and TO phonons along [00*L*]. In addition, the nearly linear branch observed from the (4,0,0) zone along the [0*K*0] direction in Figure 2.7c contains only the *a*-*b* polarized TA modes, which exist on two separate branches before and after the avoided crossing with an optical branch at 9 meV (Figure 2.7c). In comparison, for the (4,2,0) zone (Figure 2.7d), the simulations suggest that the branch observed to bend down toward the zone boundary at 6 meV is an *a*-*b* polarized TO branch, which encounters an avoided crossing with the *a*-*b* polarized TA branch.

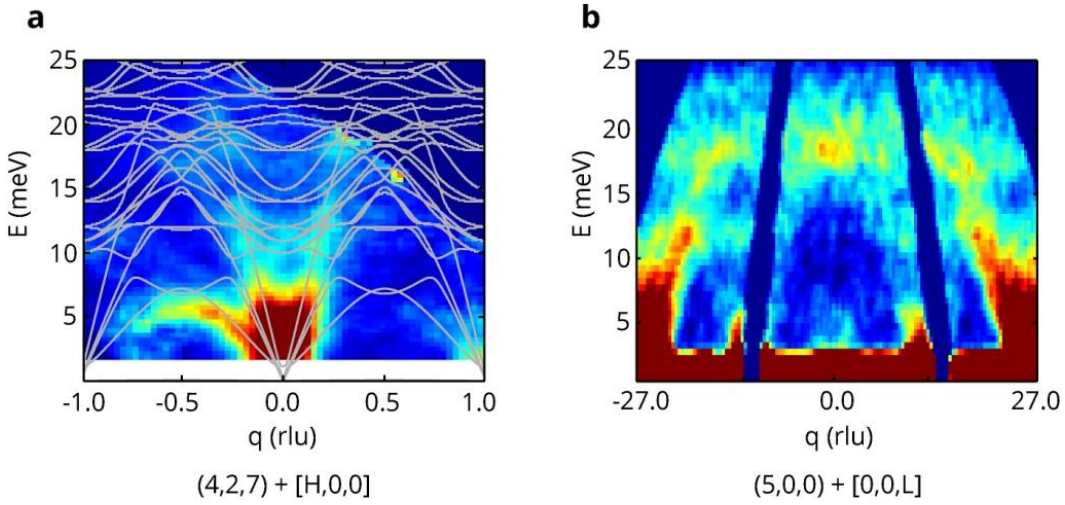

Figure 2.8: *S*(***Q***,*E*) ARCS data from (a**)** the (4,2,7) zone along [*H*00], and (b) (5,0,0) zone along [00*L*]. Gray lines are the harmonic dispersions calculated from density functional theory (DPT) for the Mn_4Si_7 phase.

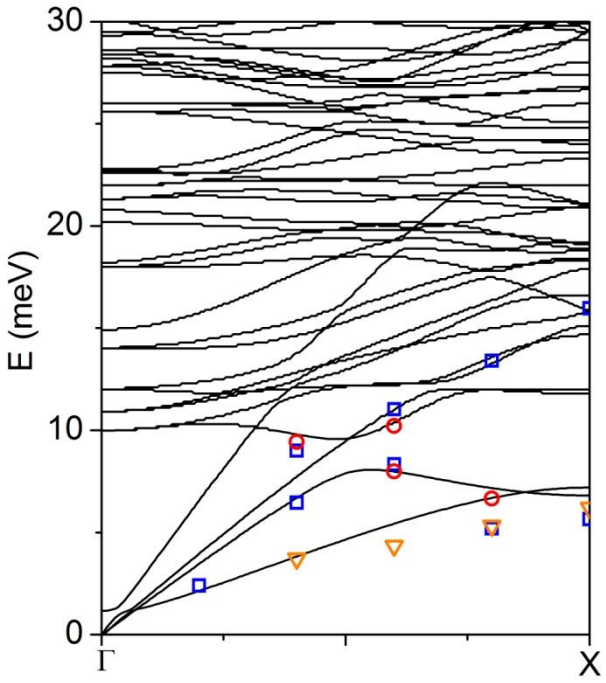

Figure 2.9: Triple-axis data for HMS single crystal at 300 K. The open symbols in (b) are the Gaussian fitting of the peak position of the INS line width measured with the triple-axis instrument at 300 K in the (2,0,0) zone (blue squares), $(2,\bar{2},0)$ zone (red circles) and $(2,\bar{2},7)$ zone (orange triangles) along [0*K*0]. Solid black lines are calculated harmonic dispersions of Mn_4Si_7.[107]

For the (4,2,7) zone along [0*K*0] (Figure 2.7e) and along [*H*00] (Figure 2.8a) as well as the $(4,1,\overline{20})$ zone along [0*K*0] (Figure 2.7f), the observed lowest-energy branch matches best the calculated twisting polarization, the simulated neutron intensity of which is one order of magnitude higher than that for the closest *a*-*b* polarized TA polarization. In addition, the *a*-*b* polarized TA branch has been observed experimentally in the (4,0,0) zone along [0*K*0] (Figure 2.7c) at a higher energy than the low-energy branch observed in Figure 2.7e-f and Figure 2.8a. It is important to note that because the *c* lattice parameter in the HMS unit cell is much larger than the *a* or *b* lattice parameter, a factor of 20 for $Mn_{27}Si_{47}$, a momentum transfer of $\boldsymbol{Q} = (4,1,\overline{20}) + \boldsymbol{q}$ still represents a fairly small momentum transfer in the [00*L*] direction. As a result, the *c*-polarized TA

modes from this zone are expected to be masked by the much stronger intensity of the nearby *a*-*b* polarized TA modes. Hence, the lowest-energy branch observed in Figure 2.7e-f along [0*K*0] and in Figure 2.8a along [*H*00] must be the twisting polarization. This conclusion is further supported by the additional triple-axis neutron scattering measurement results (Figure 2.9), where the observed phonon peaks follow the calculated TA and twisting modes quite well.

The group velocity of the acoustic modes near $\boldsymbol{q} = 0.1(2\pi/a)$ from LA and the TA branches from INS results along the principal axes are presented in Table 2.1 as well as the group velocity from the theoretical dispersion. The measurement results agree well with the calculated results.

Table 2.1: Group velocities of acoustic modes near $\boldsymbol{q} = 0.1(2\pi/a)$ or $\boldsymbol{q} = 0.1(2\pi/c)$ from the experimental data compared to the theoretical results. The measured v_g is obtained from the slope of the experimental INS (ARCS) peaks.

Branch	Calculated v_g (km s^{-1})	Measured v_g (km s^{-1})
[*H*00] and [0*K*0]		
LA	8.51	8
ab-TA	5.05	5
c-TA	4.52	
[00*L*]		
LA	8.76	
TA	5.08	5

We note that the measured twisting mode frequencies are slightly lower than those calculated for the Mn_4Si_7 phase. This difference can be attributed to the difference in the *c* lattice parameters of the HMS phases measured by INS and considered in the DFT calculation. The low frequencies of the twisting modes are associated with the large total mass of the long Si helices and can decrease with increasing *c* lattice parameter or mass of the Si helices.

We also note that INS measurements do not have sufficient resolution to reveal the fine features of the avoided crossing between the twisting polarization and the LA and *c*-polarized TA branch along the Γ-X direction. In an attempt to detect the zone center energy of the twisting polarization, far-infrared spectroscopy or Raman scattering measurements were performed. As shown in Figure 2.10a, two peaks at about 37 meV and 58 meV were found in the Raman spectra, which is consistent with the measured phonon density of states (Figure 2.11a). Phonon modes below 10 meV, especially the twisting polarization with ~1 meV energy at Γ, cannot be detected because of the strong elastic scattering near the zone center as a result of the finite line width of the excitation laser. Figure 2.10b shows the far IR spectra of HMS. The sharp peak is observed at about 60 meV along with some small peaks at 53 meV, 48 meV, 44 meV, 38 meV, 35 meV and 33 meV. It should be noted that phonon modes below 20 meV were not resolved because the signals are all within the detector fluctuation. This uncertainty is further amplified by the normalization process.

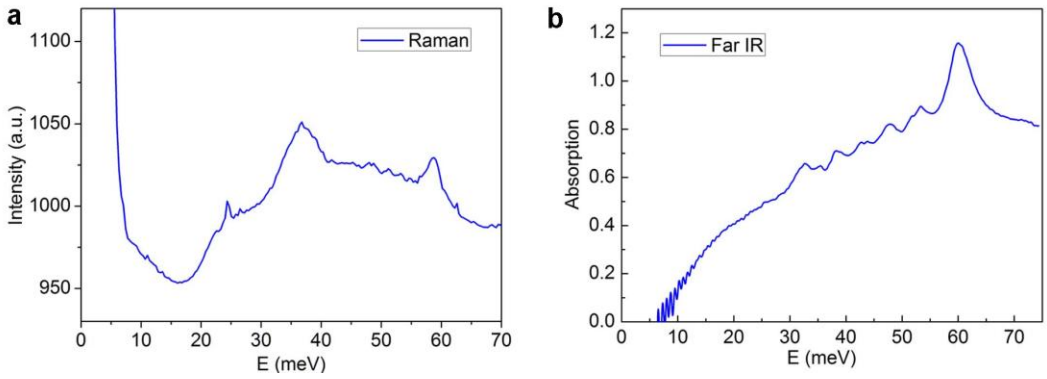

Figure 2.10: (a) Raman scattering spectra of HMS single-crystal at 300 K. (b) far IR absorption spectra of HMS polycrystal at 300 K.

Despite these limitations in existing experimental techniques, the presence of the lowest lying twisting polarization has been clearly identified by both the ARCS (Figure 2.7e-f, and 2.8a) and triple-axis measurement results (Figure 2.9b). The twisting mode together with other low-lying optical modes have low group velocities, and can provide a large phase space for scattering of acoustic phonons. These features could explain the inherently low thermal conductivity of HMS. Moreover, the DFT calculations and additional thermal conductivity analysis reveal the anisotropic average group velocity and anisotropic relaxation time along *a* and *c* axes, which are responsible for the anisotropic κ behavior. The more intense phonon scattering along the *c* axis could result from the incommensurate nature of crystal structure. It is found that the a special solid-state, which is called soliton system, can exist in HMS due to the weak interaction of Mn and Si sublattices along the *c* axis.[59] A regular system of regions of commensurate structure is separated by the soliton walls along the *c* axis, which can lead to unique physical properties. For example, the scattering of phonons along the *c* axis could be enhanced by such soliton walls. Similar low and anisotropic thermal conductivity behavior is also found in the misfit layered structures, such as $(LaS)_{1+m}TS_2$ (T=Cr, Nb)[111] and $Ca_3Co_4O_9$[112], which are attributed to their modulated crystal structures. In addition, the scattering of phonons by the MnSi layers along the *c* axis could also play an important role on the anisotropic κ_L at low temperatures.

2.5 PHONON DENSITY OF STATES AND SPECIFIC HEAT OF HMS CRYSTAL

Figure 2.11a shows the phonon density of states (DOS) measured with INS on HMS powder samples. The measured DOS show two optical phonon peaks at ~37 and ~55 meV, and a cut-off energy of ~ 65 meV. The experimental data is in good agreement with the calculated DOS of Mn_4Si_7 by Natalio Mingo's group and Derek A. Stewart's

group. However, in the high-energy range between 50 and 60 meV, the calculated DOS does not reveal the broad peak shown in the INS data in the HMS sample. One possible cause of this discrepancy is the variation in the high-energy optical modes associated with the slightly different Si ladder sublattices considered by the calculation and encountered in the experiment. Moreover, the strong anharmonicity can make the high-energy phonon spectrum deviate from the harmonic lattice dynamical calculation.

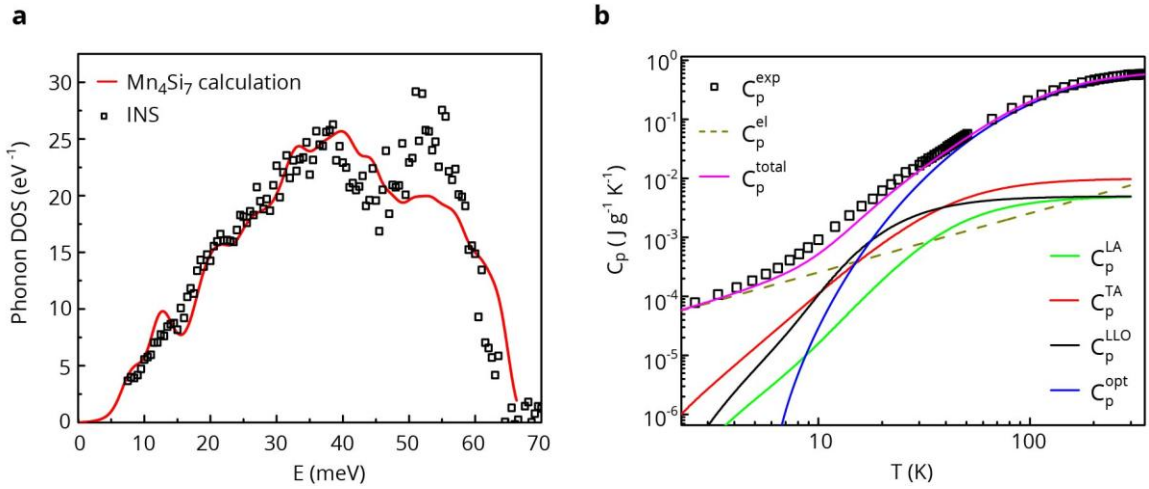

Figure 2.11: Phonon DOS and specific heat. (a) Neutron weighted phonon DOS of HMS polycrystalline sample at 300 K compared with the calculated phonon DOS of Mn_4Si_7, which was corrected for neutron weighting. (b) Measured specific heat (C_p^{exp}) of an HMS crystal compared with the calculated specific heat (C_p^{total})of Mn_4Si_7. The calculated specific heat consists of the contributions from electron (C_p^{el}), LA modes (C_p^{LA}), TA modes (C_p^{TA}), twisting or LLO modes (C_p^{LLO}), and other optical modes (C_p^{opt}).

Figure 2.11b shows the measured specific heat (C_p) of HMS crystal from 2 K to 300 K. The total C_p for the HMS-system consists of contributions from the phonons (C_p^{ph}) as well as from the electrons (C_p^{el}). C_p^{ph}, the phonon contribution, consists of the contributions from LA modes (C_p^{LA}), TA modes (C_p^{TA}), LLO twisting modes (C_p^{LLO}), and

optical modes (C_p^{opt}). They were calculated from the knowledge of the phonon band structure over the complete Brillouin zone at equilibrium and near equilibrium configurations. The electronic contribution, on the other hand, may be calculated from the electronic density of states. These calculation results were obtained by Natalio Mingo's group and Derek A. Stewart's group. Because of the low energy of the numerous optical polarizations, their contribution to the specific heat is found to be dominant above 20 K. In comparison, for $T < 8$ K, the total specific heat is dominated by the electronic specific heat. The measured values compares well with the calculated total specific heat.

2.6 SUMMARY

The phonon dispersion of an HMS crystal was measured via inelastic neutron scattering measurements in order to understand the phonon dynamics in such complex NCL system. The HMS crystal with approximately 6 mm diameter and 10 mm length was grown by the Bridgman method. A minority phase of MnSi layers with thickness of about 600 nm were found in the HMS matrix. The Seebeck coefficient, electrical conductivity, and thermal conductivity of HMS crystal were measured along the *a* and *c* axes at temperature below ~300 K. It is found that these properties show anisotropic behavior in the entire measured temperature range due to the anisotropic crystal structure.

The inelastic neutron scattering measurements were performed on the HMS crystal at 300 K with both the time-of-flight wide angular-range chopper spectrometer and triple axis spectrometer. Acoustic modes and a number of low-lying optical vibration modes were observed in our study, which agrees with the DFT calculations obtained by our collaborators. In the (4,0,0) zone along [*H*00], LA branch intercepts a TO branch

about halfway between the zone center and zone boundary at ~15 meV. The *a*-*b* polarized TA branch along [0*K*0] extends to ~15 meV and intercepts the *a*-*b* polarized TO branches near the zone boundary. A broad linear band along [00*L*] appears to extend to roughly $27\pi/c$ or π/c_{Mn}, the zone boundary of the Mn sublattice instead of that of Mn_nSi_{2n-m}. The flat optical branches were observed between 10 and 25 meV, which is rather low compared to that of Si. Among them, a lowest-lying-optical branch extends to the zone boundary at roughly 5 meV in the (4,2,7) zone as well as in $(4,1,\overline{20})$, which is in good agreement with the predicted twisting mode in the calculated phonon dispersion of Mn_4Si_7. These low-lying optical modes provide a large phase space for scattering of acoustic phonons, which leads to the inherently low thermal conductivity of HMS.

Far-infrared spectroscopy or Raman scattering measurements were performed on HMS samples in attempt to detect the zone center energy of the twisting polarization. However, neither of these techniques provides sufficient spectral range and resolution to determine the unusually low energy (<1 meV) of the twisting polarization at the zone center.

Measured phonon DOS shows two optical peaks at ~37 and ~55 meV, and a cut-off energy of ~65 meV. These features qualitatively agree with the calculated phonon DOS of Mn_4Si_7. In addition, the specific heat of HMS was measured from 2 K to 300 K. The values compare well with calculated specific heat with contributions from phonons and electrons.

Chapter 3: Effects of (Al,Ge) double doping on the microstructure and thermoelectric properties of HMS*

3.1 INTRODUCTION

Recently, a number of studies have been focused on tuning the electric transport properties of HMS by chemical substitutions.[66,78,82,84-86,112] *ZT* values of 0.6-0.65 at about 850 K were achieved by single element doping, such as Ge doping[86] and Al doping[78] in polycrystalline HMS. Although an even higher *ZT* of ~0.7 at about 800 K has been reported in complex doped HMS,[59] the dopants were not specified in the report. The power factor of a TE material usually peaks at certain carrier concentration level. However, the optimized carrier concentration for HMS is not well studied.

In this chapter, the effects of Al doping and (Al,Ge) doping on the TE properties of HMS are discussed in order to study the optimized carrier concentration in HMS. Al and Ge dopants are chosen because either Al or Ge doping alone has been found to result in enhanced *ZT*.[78,86] The synthesis and TE properties of Al-doped HMS are first presented. The synthesis and TE properties of (Al,Ge) doped HMS is then followed. The microstructures of these samples are also investigated in detail.

3.2 EXPERIMENTAL METHODS

3.2.1 Preparation of HMS

HMS samples were synthesized through three steps, *i.e.* the solid-state reaction (SSR), ball milling (BM), and spark plasma sintering (SPS). The starting materials, Mn

* **X. Chen**, A. Weathers, D. Salta, L.B. Zhang, J.S. Zhou, J.B. Goodenough, L. Shi, "Effects of (Al,Ge) double doping on the thermoelectric properties of higher manganese silicides", *Journal of Applied Physics*, 114, 173705 (2013)
X.C., L.S., J.S.Z. and J.B.G. designed the research. X.C. synthesized the materials and did the measurements. A.W., L.S. and X.C. calculated the electronic contribution of the thermal conductivity. D.S and L.B.Z. helped with the thermal properties measurements. X.C., A.W. and L.S. wrote the manuscript and all authors commented on and edited the manuscript.

(purity, 99.95%), Si (purity, 99.999%), Ge (purity, 99.999%) and Al (purity, 99%) powders, were purchased from Alfa Aesar. The procedure of solid-state reaction has been reported previously.[76] In a typical sample-preparation procedure, the powders with nominal chemical composition $Mn(Al_xSi_{1-x})_{1.8}$ (x = 0, 0.0015, 0.003, 0.0045, 0.006) and $Mn(Al_{0.0035}Ge_ySi_{0.9965-y})_{1.8}$ (y = 0.003, 0.006, 0.01, 0.015, 0.025) were weighed, and then hand-ground with an agate mortar and pestle for 1 h. Subsequently, the powder was sealed in a vacuumed quartz tube. The quartz tube was placed in a furnace and sintered at 900 ^oC for 48 h. The as-sintered HMS powder was loaded into a tungsten-carbide jar and ball milled for 90 minutes in argon by a SPEX 8000M Mixer/Mill (SPEX SamplePrep). Finally, the ball milled powders were consolidated into dense bulk materials by SPS at 1123 K for 5 minutes under 60 MPa.

3.2.2 Characterization of HMS

The crystal structure of the samples was investigated by X-ray diffraction (XRD) with a Phillip X'pert diffractometer and Cu K_α radiation. The morphology and chemical compositions of the HMS samples were analyzed by using a Quanta 650 environmental scanning electron microscope (SEM) with an energy-dispersive X-ray (EDX) spectrometer. The actual compositions of the samples were analyzed by electron probe microanalysis (EPMA). In order to detect the MnSi phase in the HMS samples, the pellets for SEM were polished and chemically etched by a solution of $HF:HNO_3:H_2O$ (1:6:13). The resistivity was measured in the temperature range between 300 K and 823 K with a four-probe method. The Seebeck coefficient was measured in the temperature range 80-823 K with a home-made setup. The thermal diffusivity, λ, was measured with the laser flash diffusivity method in a Netzsch LFA 457. The specific heat, C_p, was obtained by a differential scanning calorimetry (DSC) system (Netzsch DSC 404). The

density, ρ, was measured by the Archimedes' method. The thermal conductivity was calculated as $\kappa = \lambda C_p \rho$. The Hall coefficient measurements were carried out on the Physical Properties Measurement System (PPMS, Quantum Design). All three transport properties were measured along the direction of the SPS pressing force.

3.3 Effect of Al doping on the microstructure and TE properties of HMS

3.3.1 Phase and microstructures of Al-doped HMS

Figure 3.1a shows the XRD patterns of the products after SSR, BM, and SPS. It can be seen that a pure HMS phase was formed after solid-state reaction. The peaks become significantly broader after BM owing to either residual strain or finer particle size.[113] Figure 3.1b shows a typical disc after SPS in this study, as well as the bar and plate samples that were used for the measurement of electrical and thermal transport properties, respectively. The XRD patterns of Al-doped samples after SPS are shown in Figure 3.1c. Besides the HMS phase, no impurity phases were detected. The HMS powders are usually a mixture of several phases with different *c* lattice parameters.[96] Here, the lattice parameters of all samples were calculated on the premise that the material was a single phase ($Mn_{27}Si_{47}$). As shown in Figure 3.1d, the lattice parameters of HMS do not change significantly by small amounts of Al doping.

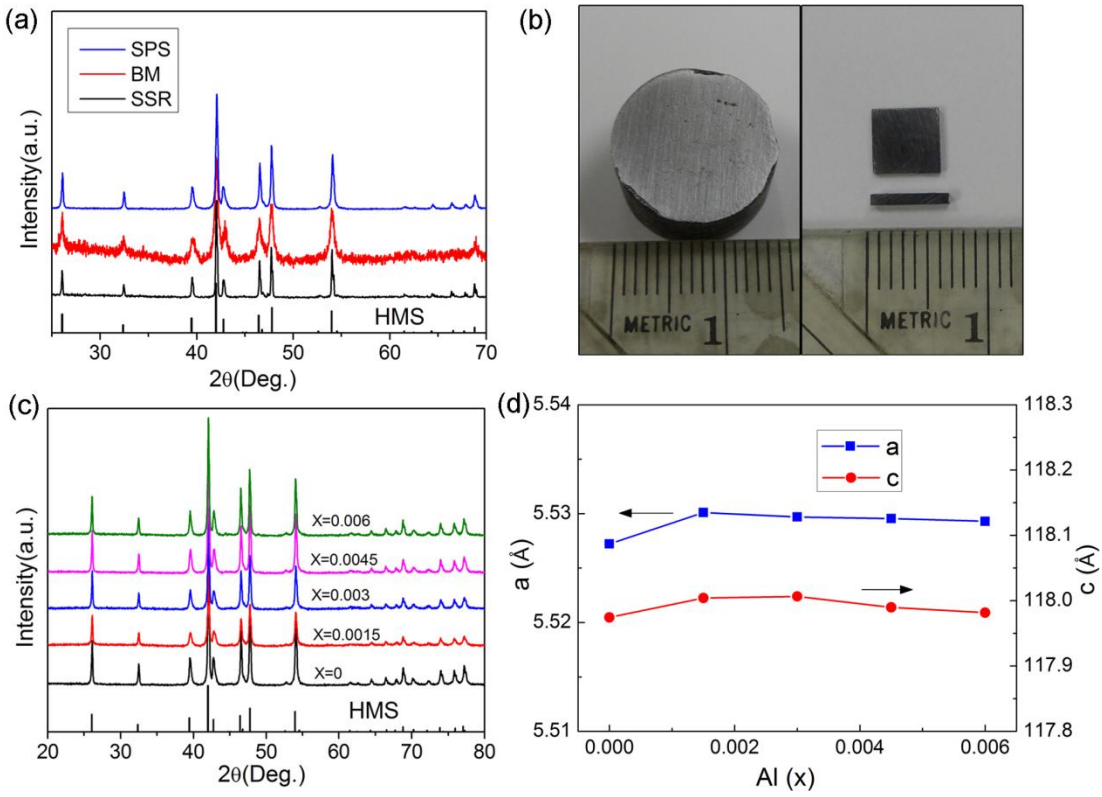

Figure 3.1: (a) XRD patterns of undoped HMS after SSR, BM and SPS. (b) Photographs of a 15 mm diameter, 8 mm thick disc made by SPS, a 1 mm × 1 mm × 6 mm bar for electrical measurements that was cut along the direction of the SPS pressing force, and a 6 mm × 6 mm × 1 mm plate for thermal conductivity measurement that was cut normal to the direction of the SPS pressing force. Therefore, all TE properties were measured along the same direction. (c) XRD patterns of $Mn(Al_xSi_{1-x})_{1.8}$ ($0 \leq x \leq 0.006$) after SPS. (d) The measured lattice parameters of $Mn(Al_xSi_{1-x})_{1.8}$ as a function of x.

The morphologies of Al-doped samples before and after etching are shown in Figure 3.2. Pores of less than 1 μm can be found in the sample after SPS and before etching, as shown in Figure 3.2a. It can be seen that HMS samples consist of both large grains with diameters of several microns and smaller grains. It should be noted that these grains may be agglomerates of smaller crystallites. Figures 3.2b-e show the SEM images of Al-doped samples after polishing and etching by HF solution. Aoyama *et al.*[66] and

Zhou *et al.*[86] have observed the MnSi phase by etching HMS samples with a hydrofluoric acid (HF) solution. Owing to the faster etching rate of MnSi than that of HMS, MnSi striations can be found in the HMS matrix. Here, MnSi striations (Figure 3.2b) can also be observed after etching as compared to the SEM image before etching (inset of Figure 3.2b). The MnSi layers are about 0.1 μm in width and 1-3 μm in length. Layers of the MnSi phase are arranged parallel to each other in different grains with different orientations. The distance between adjacent layers is about 350 nm, which is much smaller than the ~20 μm value in single-crystals as shown in Chapter 2. With an increase of Al doping, no obvious change in the morphology of MnSi can be observed, as shown in Figures 3.2b-e. In the sample with x = 0.006, the presence of some Al-rich phases (Figure 3.2f) suggests the solid-solution limit of Al in HMS is less than 0.006.

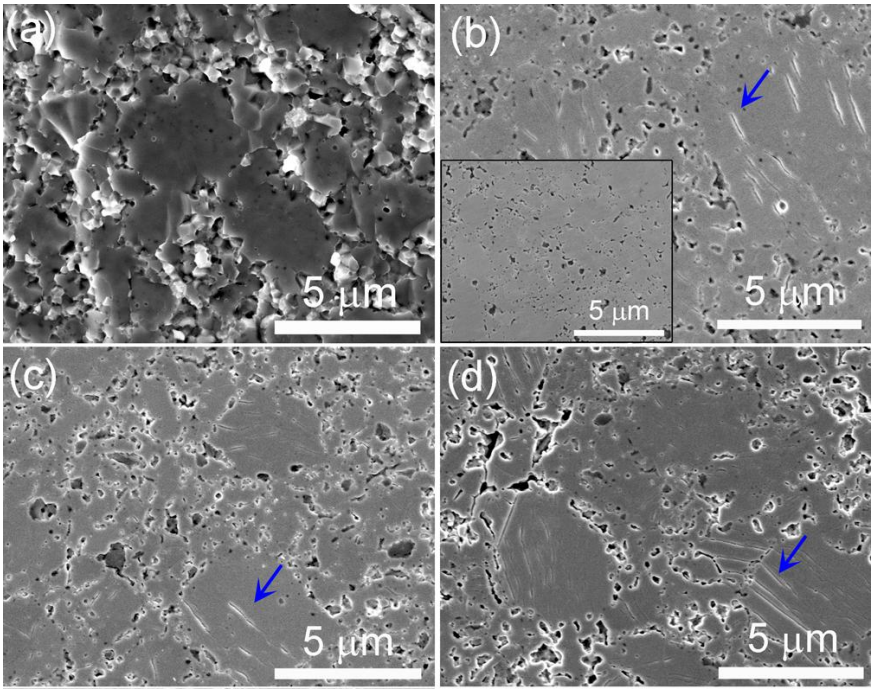

Figure 3.2 continued.

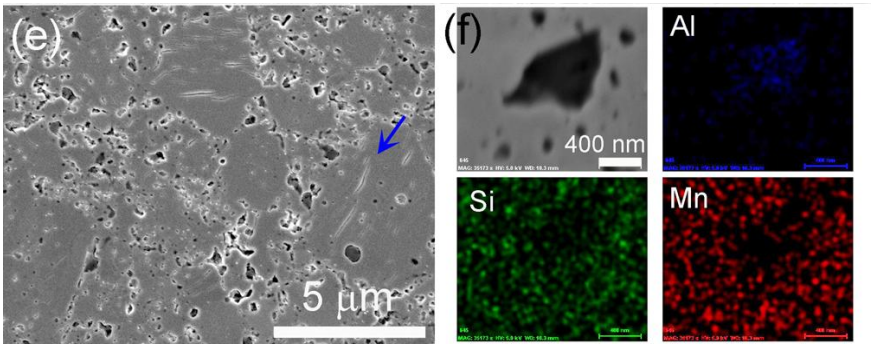

Figure 3.2: (a) SEM image of the fracture surface of the udoped HMS after SPS. (b)-(e) SEM images of $Mn(Al_xSi_{1-x})_{1.8}$ with x = 0, 0.0015, 0.0045, 0.006 respectively, after polishing and etching. (f) SEM image of the HMS sample with x = 0.006 and elemental maps of this sample. The inset of Figure (b) is a SEM image of a HMS sample before etching. The MnSi striations are pointed out by blue arrows.

3.3.2 TE properties of Al-doped HMS

Table 3.1 shows the actual composition, density and electrical transport properties of the Al-doped HMS at room temperature. The measured composition by EPMA is approximately similar to the nominal composition. The densities of all samples exceed 93% of the theoretical value. Hall coefficient measurements were carried out for Al-doped HMS at room temperature, and the results are also listed in Table 3.1. The Hall coefficients of all samples are positive, confirming that the Al-doped HMS remains a *p*-type semiconductor. The Hall carrier concentration increases with increasing Al doping up to x = 0.0045, and then decreases with a further increase of Al to x = 0.006. Since Al has less valence electrons than Si, the hole concentration of HMS increases when Si is substituted by Al.[78,114] However, the Al-rich phase precipitates when the solid solution limit of Al is exceeded. The Al-rich phase may donate electrons to HMS, similar to the modulation doping concept,[30,31,115] and thus reduce the hole concentration of HMS. The

decrease of hole concentration with increased Al doping concentration is also observed in the Al-doped HMS prepared by melt-spinning and SPS.[78] In contrast, the mobility of Al-doped samples does not change much. As a consequence, doping with Al effectively increases the electrical conductivity.

Table 3.1: Measured composition, density and room temperature electrical transport properties of $Mn(Al_xSi_{1-x})_{1.8}$ samples.

Nominal composition	Measured composition	Density (g/cm^3)	σ (Ω^{-1} cm^{-1})	R_H (10^{-9} m^3 C^{-1})	p (10^{21} cm^{-3})	μ_h (cm^2 V^{-1} s^{-1})
x=0	$Mn_{1.023}Si_{1.800}$	4.79	470	4.11	1.52	1.93
x=0.0015	$Mn_{1.026}(Al_{0.001}Si_{0.999})_{1.800}$	4.81	510	3.62	1.73	1.84
x=0.003	$Mn_{1.077}(Al_{0.002}Si_{0.998})_{1.800}$	4.82	531	3.58	1.75	1.90
x=0.0045	$Mn_{1.067}(Al_{0.003}Si_{0.997})_{1.800}$	4.85	545	3.46	1.81	1.88
x=0.006	$Mn_{1.073}(Al_{0.006}Si_{0.994})_{1.800}$	4.84	480	4.04	1.55	1.94

The temperature dependences of the electrical conductivity (σ) and the Seebeck coefficient (S) for Al-doped samples are displayed in Figures 3.3a and 3.3b, respectively. All Al-doped samples exhibit the characteristics of a degenerate *p*-type semiconductor with positive *S*. The electrical conductivity at 300 K increases from 470 $\Omega^{-1}cm^{-1}$ in the undoped HMS to 545 $\Omega^{-1}cm^{-1}$ in the sample with x = 0.0045. At 823 K, the conductivities of the undoped and the Al-doped HMS are 280 $\Omega^{-1}cm^{-1}$ and 320 $\Omega^{-1}cm^{-1}$, respectively. However, the sample with x = 0.006 shows a much lower electrical conductivity than other doped samples, which is even lower than that of the undoped HMS at high temperatures. According to SEM observation and Hall measurements, some Al-rich phases form in the sample with x = 0.006 as the solid solution limit is exceeded. As a result, the effective carrier concentration is reduced so that the electrical conductivity decreases. The Seebeck coefficient increases linearly until 600 K, and reaches a

maximum of ~240 μV/K at 750 K. The higher electrical conductivity and a similar Seebeck coefficient give rise to increased power factors of Al-doped samples with x between 0.0015 and 0.0045, as shown in Figure 3.3c. The sample with x = 0.0045 shows a maximum power factor value of 1.8×10^{-3} $Wm^{-1}K^{-2}$ at 823 K, which is about 20% higher than undoped HMS. The measured average specific heat of ten of the undoped, Al-doped and (Al,Ge)-doped HMS samples is shown in the inset of Figure 3d. Because the doping concentration is low, the specific heat is not expected to vary considerably among the HMS samples. Hence, we have used the measured average specific heat value to calculate the thermal conductivity of all samples. The inset of Figure 3.3d shows the temperature dependence of thermal conductivity κ. The typical thermal conductivity shows a plateau between 300 K and 700 K, and starts to increase with $T > 700$ K. The Al-doped samples exhibit similar values in the measured temperature range, which are about 4% lower than that of undoped HMS at 800 K. However, this is within the uncertainty of the thermal conductivity measurement.

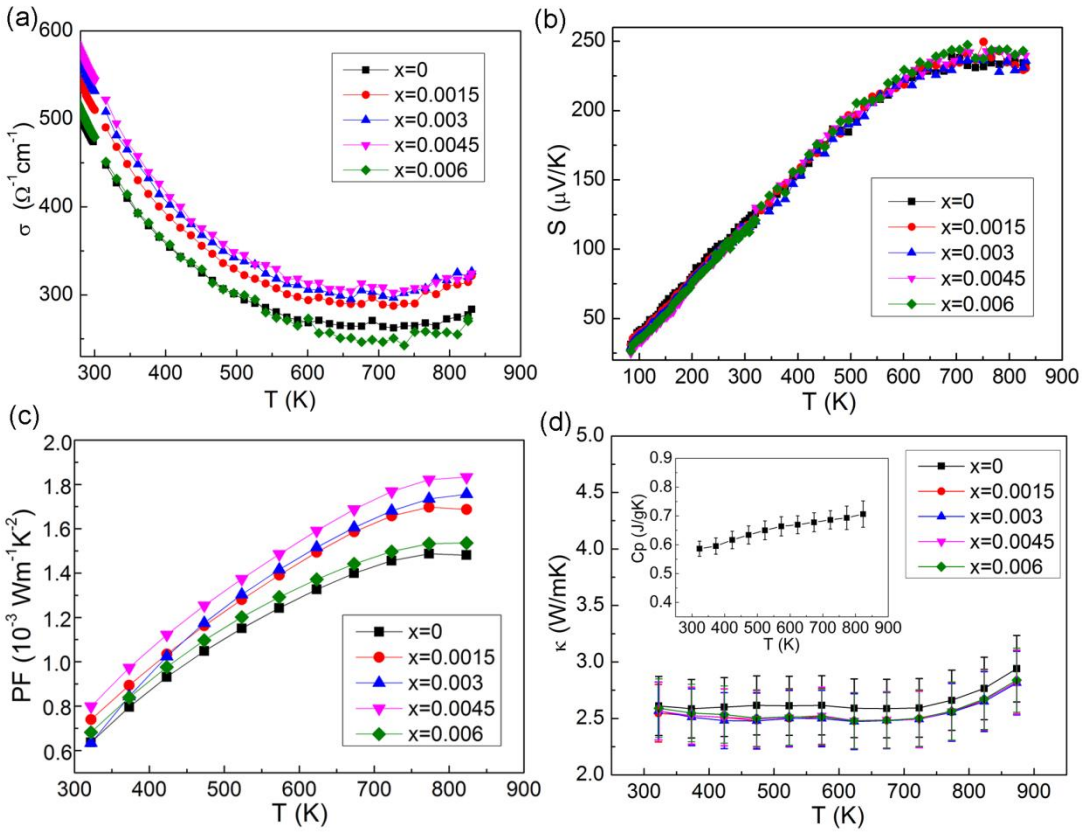

Figure 3.3: Temperature dependence of transport properties for $Mn(Al_xSi_{1-x})_{1.8}$: (a) electrical conductivity with 5% uncertainty, (b) Seebeck coefficient with 5% uncertainty, (c) power factor with 11% uncertainty, and (d) thermal conductivity with 10% uncertainty. The power factors of the doped HMS were obtained by a polynomial fitting to the measured Seebeck coefficient and electrical conductivity which were measured at slightly different temperatures. The inset of Figure (d**)** is the average specific heat value of six different samples, with 4-7% uncertainty.

Luo *et al.*[78] prepared Al-doped HMS, $Mn(Al_xSi_{1-x})_{1.8}$, by melt-spinning and SPS. They found that the Al dopant can improve the electrical conductivity and reduce the thermal conductivity due to an increase of carrier concentration and defects within the solid solution limit, which was found up to x = 0.0015. They have also reported that the electrical conductivity starts to decrease and the thermal conductivity increases for

samples with x > 0.0015. In comparison, a higher solid-solution limit of x = 0.003 is found in the current investigation. The Al-rich phase forms when the Al concentration exceeds this limit, which is accompanied by the decrease of electrical conductivity. Hence, the solid solution limit of Al and the formation of the secondary Al-rich phase appear to depend on the sample synthesis procedure.

3.3.3 Electronic thermal conductivity and *ZT* of Al-doped HMS

To understand better the increase in the thermal conductivity above 700 K and the effect of Al doping on the lattice thermal conductivity, it is necessary to determine the electronic contribution to the thermal conductivity. HMS is a highly degenerate *p*-type semiconductor at room temperature. However, a plateau in the Seebeck coefficient at approximately 750 K suggests the possibility of increased minority charge transport and bipolar heat conduction.

The electronic thermal conductivity of HMS was calculated according to the two-band model discussed in Chapter 1. Several previous works have reported the ratio of electron to hole mobility in HMS to be approximately 0.02,[116,117] the density of states electron effective mass, $(m_{xx}m_{yy}m_{zz})^{1/3}$, to be 6.61,[14] and the band gap of pure HMS to be 0.77 eV.[14] With the use of these three values, equations (1.13), (1.16), and (1.17) can then be reduced to functions of three variables, the hole effective mass, m_h^*, the Fermi level, ξ_e, and the hole mobility μ_h, which are solved based on the measured *S*, σ, and R_H at room temperature from equations (1.13), (1.16), and (1.17). At higher temperatures, the effective mass and the mobility ratio are assumed to be constant, and equations (1.13) and (1.16) are used to solve for the Fermi level and the Hall mobility based on the measured *S* and σ as a function of temperature. The room-temperature m_h^*, μ_h and E_F determined from the model are 9.3 m_0 (m_0 is the free electron mass), 1.7 $cm^2V^{-1}s^{-1}$, and

-0.82 eV measured from the conduction band edge or 0.05 eV below valence-band edge, respectively. These values are comparable to the literature values reported by Nishida,[117] namely, $m_h^* = 12\ m_0$, $\mu_h = 2.3\ \mathrm{cm^2V^{-1}s^{-1}}$, and Migas *et al.*,[14] i.e.0.05-0.07 eV below the valence-band edge.

Figure 3.4 shows the different contributions to the thermal conductivity for undoped HMS. The bipolar term and the electron contribution were found to be negligibly small for all samples, owing to an electron concentration several orders of magnitude lower than the hole concentration of $1.5 \times 10^{21}\ \mathrm{cm^{-3}}$ even at temperatures up to 823 K, where the electronic thermal conductivity is dominated by the hole contribution. The finding is in good agreement with another calculated electronic contribution in a nanostructured HMS sample.[90]

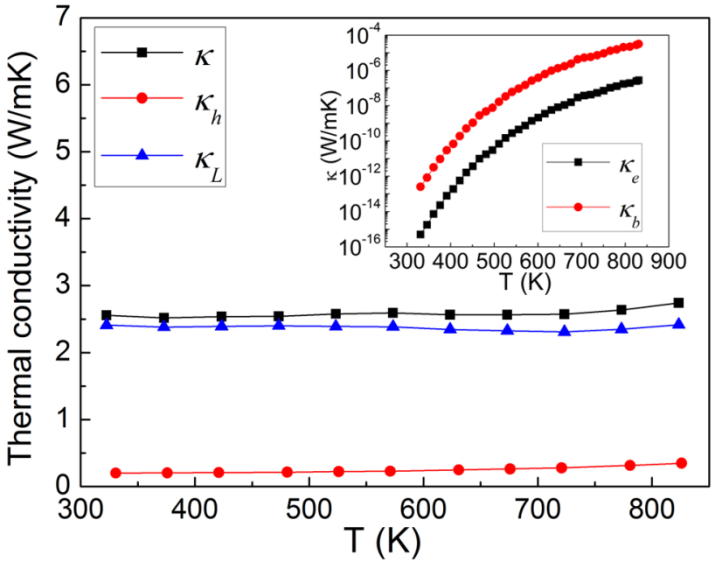

Figure 3.4: The total thermal conductivity (κ), lattice thermal conductivity (κ_L), and hole thermal conductivity (κ_h) of undoped HMS. The inset shows the bipolar contribution (κ_b) and electron contribution (κ_e) of undoped HMS.

The lattice thermal conductivity found from this analysis is approximately constant in the temperature range between 300 K and 823 K for the undoped sample. In comparison, for single-crystal semiconductors with a relatively simple crystal structure[118] and for amorphous materials[119] in the same temperature range, the lattice thermal conductivity usually decreases and increases with increasing temperature, respectively. The nearly constant lattice thermal conductivity observed here can be attributed to the polycrystalline HMS with a very complex structure. In such a structure, grain boundary scattering, which can result in increased lattice thermal conductivity with increasing temperature,[120] is as important as umklapp scattering, which results in the opposite temperature dependence. Moreover, thermal excitation of numerous optical phonon modes at high temperatures can also increase the lattice thermal conductivity with temperature.[121]

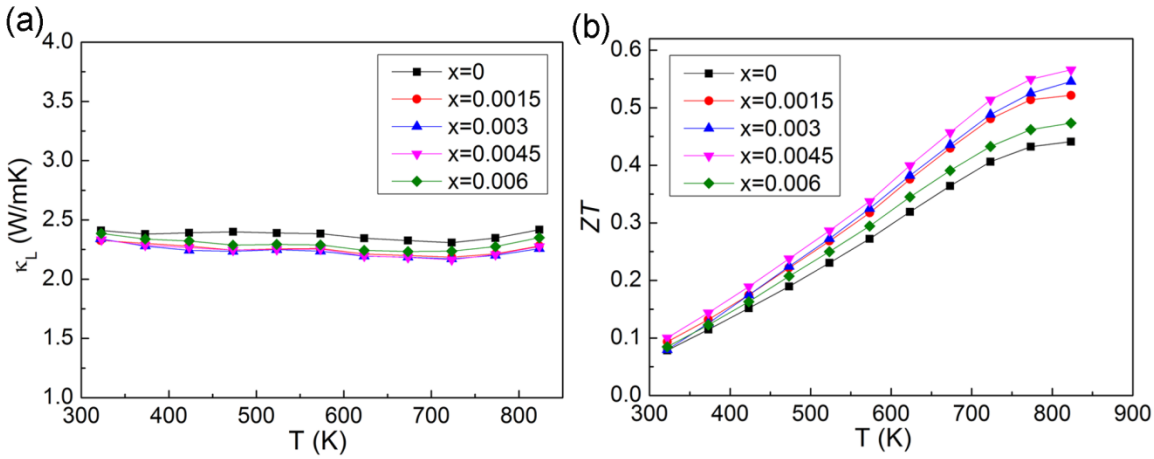

Figure 3.5: (a) The lattice thermal conductivities (κ_L) and (b) the dimensionless figure of merit (ZT) of the $Mn(Al_xSi_{1-x})_{1.8}$. The relative uncertainty in the ZT value is 15%.

Figure 3.5a shows the lattice thermal conductivities found for Al-doped samples according to a similar analysis. Considering the 10% uncertainty of the thermal conductivity measurement, the lattice thermal conductivity is not effectively suppressed by a small amount of Al doping. Figure 3.5b shows the dimensionless figure-of-merit (*ZT*) of Al-doped samples. The Al doping effectively increases the power factor of HMS. Therefore, the *ZT* values are enhanced compared to the undoped HMS. The maximum *ZT* of 0.57 at 823 K is achieved in the sample with x = 0.0045, which is about 25% higher than that of the undoped sample.

3.4 Effect of (Al,Ge) double doping on the microstructure and TE properties of HMS

3.4.1 Phase and microstructures of (Al,Ge) double doped HMS

The (Al,Ge) double doped HMS, i.e. $Mn(Al_{0.0035}Ge_ySi_{0.9965-y})_{1.8}$, were prepared by the same method as for the Al-doped samples. The XRD patterns of the (Al,Ge)-doped samples after SPS are shown in Figure 3.6a, which indicates that the main phase of the samples is HMS. The samples with y = 0.025 and 0.035, show a small peak belonging to an alloy in the Si-Ge phase diagram. A small peak from MnSi can be found in the sample with the highest amount of Ge (y=0.035). The calculated lattice parameters increase with Ge doping as shown in Figure 3.6b.

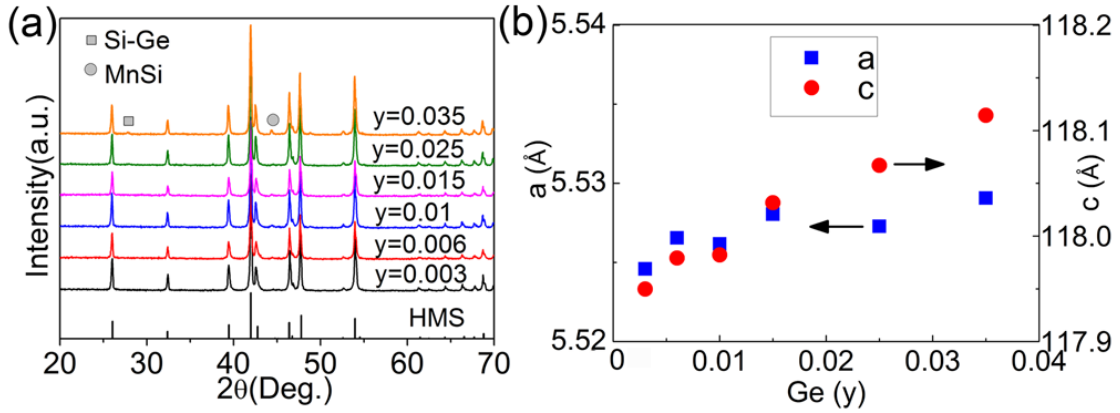

Figure 3.6: (a) XRD patterns and (b) lattice parameters of $Mn(Al_{0.0035}Ge_ySi_{0.9965-y})_{1.8}$ ($0.003 \leq y \leq 0.035$).

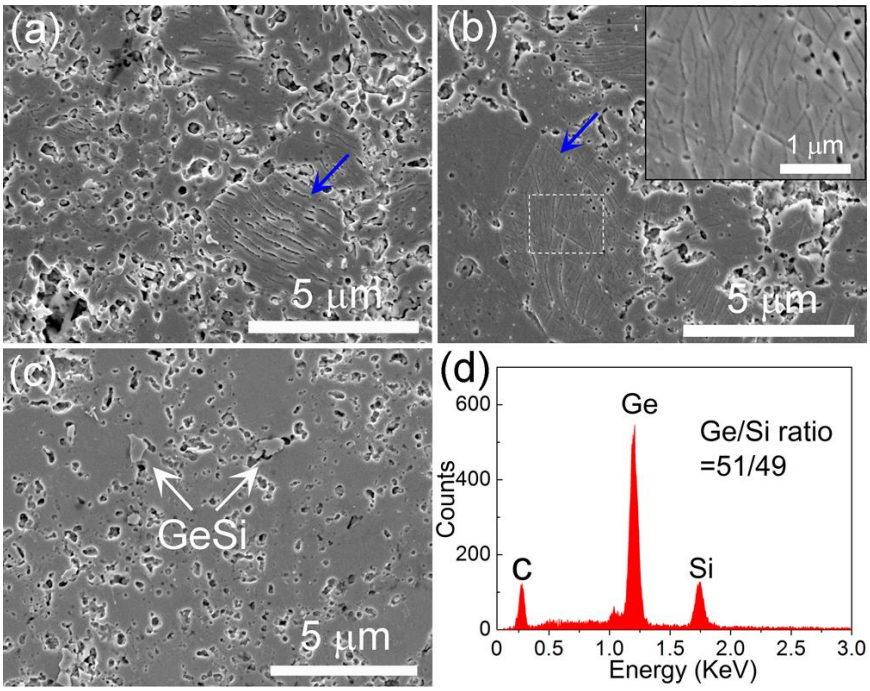

Figure 3.7: (a)-(c) SEM images of $Mn(Al_{0.0035}Ge_ySi_{0.9965-y})_{1.8}$ with y = 0.003, 0.01, 0.025 respectively, after etching. (d) EDX pattern of the precipitations in the sample with y = 0.025. The inset of Figure (b) shows the magnification of the area marked by square. The MnSi striations are pointed out by blue arrows. The GeSi phase is pointed out by white arrows.

Figure 3.7 shows the morphologies of (Al,Ge)-doped samples after polishing and etching. A small amount of Ge decreases the interval of MnSi layers (Figure 3.7a). The interval of MnSi layers in the sample with y = 0.003 is reduced to ~200 nm from about ~350 nm for the Al-doped samples. For the sample with the Ge content of y = 0.01, layers of the MnSi phase become curved and nonparallel to each other (Figure 3.7b). In accordance with the XRD results, the Si-Ge precipitations were observed in the sample with y = 0.025, as indicated by arrows in Figure 3.7c. The composition of the Si-Ge phase was studied by EDX, and the ratio of Si and Ge is determined to be about 1:1 (GeSi). Zhou *et al.*[86] investigated the micromorphology of MnSi in Ge-doped polycrystalline HMS prepared by melting and hot-pressing; they also found the MnSi phase becomes curved and a Si-Ge phase forms at high Ge concentration (> 1.6%).

3.4.2 TE properties of (Al,Ge) double doped HMS

The actual composition, density and room-temperature electrical transport properties of the (Al,Ge)-doped HMS are listed in Table 3.2. The measured composition by EPMA is similar to the nominal composition. The carrier concentration increases with increasing Ge content. The (Al,Ge)-doped samples show even higher carrier concentrations ($2.14\text{-}2.51\times10^{21}$ cm^{-3}) than the highest value for Al-doped sample (1.81×10^{21} cm^{-3}), suggesting that the double doping further increases the carrier concentration. The carrier concentration of the sample with y = 0.035 does not further increase as compared to the sample with y=0.025, suggesting the solid solution limit may be reached in this sample. The mobility of the (Al,Ge)-doped samples decreases monotonically with increasing Ge doping, which is opposite to that of the hot-pressed Ge-doped HMS.[86] This discrepancy may be due to the enhanced ionized impurity scattering in (Al,Ge)-doped HMS.

Table 3.2: Measured composition, density and room temperature electrical transport properties for $Mn(Al_{0.0035}Ge_ySi_{0.9965-y})_{1.8}$

Nominal composition	Measured composition	Density (g/cm^3)	σ (Ω^{-1} cm^{-1})	R_H (10^{-9} m^3 C^{-1})	p (10^{21} cm^{-3})	μ_h (cm^2 V^{-1} s^{-1})
y=0.003	$Mn_{1.046}(Al_{0.003}Ge_{0.004}Si_{0.993})_{1.800}$	4.89	587	2.92	2.14	1.71
y=0.006	$Mn_{1.042}(Al_{0.003}Ge_{0.007}Si_{0.990})_{1.800}$	4.93	585	2.90	2.16	1.70
y=0.01	$Mn_{1.070}(Al_{0.003}Ge_{0.015}Si_{0.982})_{1.800}$	4.92	580	2.73	2.29	1.58
y=0.015	$Mn_{1.051}(Al_{0.002}Ge_{0.018}Si_{0.980})_{1.800}$	4.95	586	2.62	2.38	1.54
y=0.025	$Mn_{1.124}(Al_{0.002}Ge_{0.034}Si_{0.964})_{1.800}$	4.94	610	2.49	2.51	1.52
y=0.035	$Mn_{1.047}(Al_{0.002}Ge_{0.043}Si_{0.955})_{1.800}$	4.98	598	2.71	2.31	1.62

The temperature dependence of carrier concentration and mobility of the undoped sample and the (Al,Ge)-doped sample with x = 0.0035, y = 0.035 are shown in Figure 3.8. The temperature-independent carrier concentration of HMS indicates it is a degenerate *p*-type semiconductor. The (Al,Ge)-doped HMS shows higher carrier concentration than that of undoped HMS in the entire measured temperature range. For undoped HMS, the mobility varies approximately as $T^{3/2}$ from 50 K, suggesting that the acoustic phonon scattering is the dominant scattering mechanism compared to ionized impurity scattering, which shows an opposite trend in mobility with temperature.[14,89,117] However, boundary scattering limited mobility is expected to show a similar trend with $T^{-1/2}$, suggesting that boundary scattering could also play a role as an important scattering mechanism in these polycrystalline samples. For (Al,Ge)-doped HMS, the relationship of $\mu_h \propto T^{-3/2}$ starts at a higher temperature (~200 K) due to enhanced ionized impurity scattering. The temperature dependences of mobility for both undoped and doped samples validate the assumption of dominant acoustic phonon scattering for the calculation of electronic thermal conductivity above 300 K.

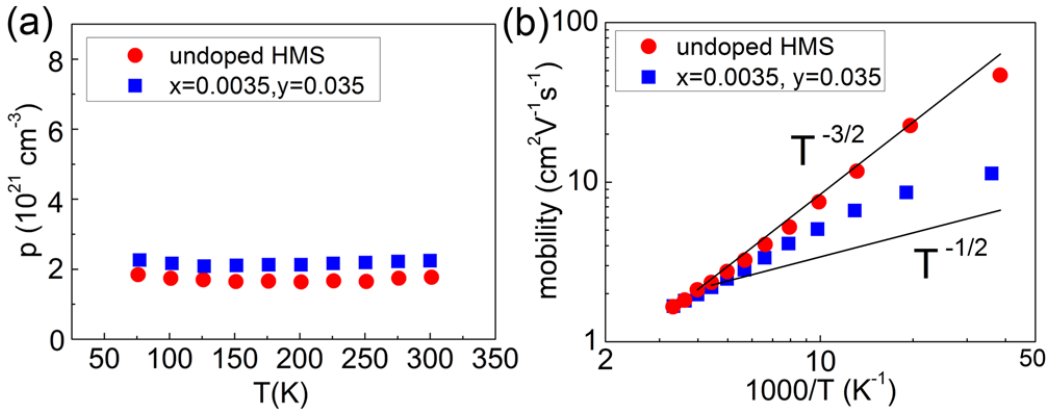

Figure 3.8: Temperature dependence of (a) carrier concentration and (b) mobility of undoped HMS and the $Mn(Al_xGe_ySi_{1-x-y})_{1.8}$ with x = 0.0035, y = 0.035.

The temperature dependence of the TE properties of (Al,Ge)-doped samples are displayed in Figure 3.9. The (Al,Ge)-doped samples show even higher electrical conductivities than the Al-doped HMS. The electrical conductivity increases monotonically with an increase in Ge content, which could be attributed to the increase of carrier concentration by the Ge doping. The sample with y = 0.025 shows the highest electrical conductivity of 610 $\Omega^{-1}cm^{-1}$at room temperature. The Seebeck coefficient of (Al,Ge)-doped samples decreases with increasing Ge doping. As a consequence, the peak power factor of (Al,Ge)-doped samples are lower than that of Al-doped HMS with x = 0.0045. The maximum power factor of the samples with y = 0.025 and 0.035 are about 15% and 30% lower than that of Al-doped HMS with x=0.0045, respectively. The thermal conductivity of (Al,Ge)-doped samples first increases with increasing Ge doping, and reaches a maximum at y = 0.006. Further increase of the Ge content suppresses the thermal conductivity. Aoyama *et al.*[66] reported the thermal conductivity of HMS single-crystals along *c*-axis first increases and then decreases with Ge doping. They attributed the initial increase of thermal conductivity to the increase of MnSi, and subsequent decrease of thermal conductivity to the increased scattering by Ge impurity and interfaces

between HMS and MnSi. Although the measured thermal conductivity in this study shows a similar trend as that in Ge-doped single-crystals, the variation of thermal conductivity is within the measurement uncertainty.

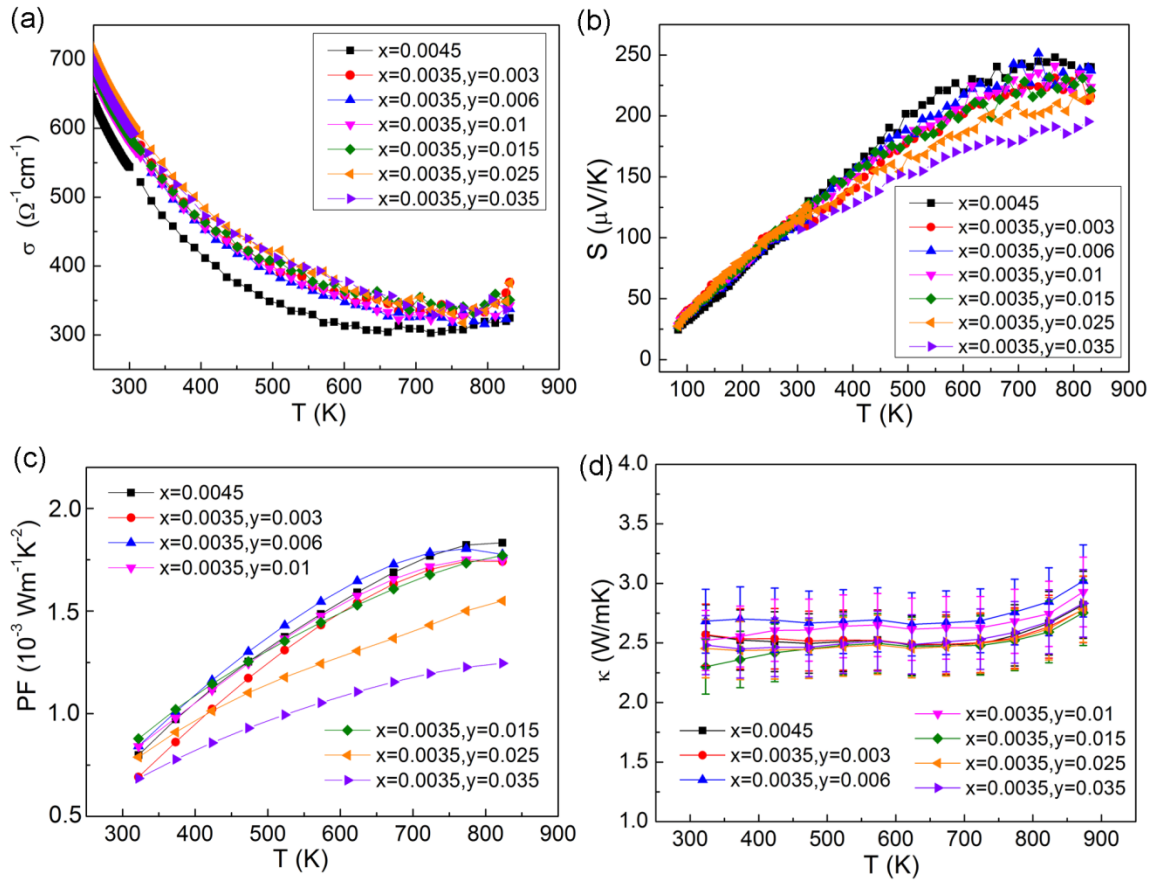

Figure 3.9: Temperature dependence of transport properties for $Mn(Al_xGe_ySi_{1-x-y})_{1.8}$: (a) electrical conductivity with 5% uncertainty, (b) Seebeck coefficient with 5% uncertainty, (c) power factor with 11% uncertainty, and (d) thermal conductivity with 10% uncertainty.

To understand the role of Ge doping on TE properties of the (Al,Ge)-doped HMS, it is necessary to consider two effects: (1) Ge substitution;[66] (2) secondary phases. It is reported that Ge substitution may disturb the arrangement of the Si subcell and form stacking faults, which can change the density of states near the Fermi level and increase

the electrical conductivity according to first-principle calculations.[14,86] In this work, the increase of electrical conductivity in (Al,Ge)-doped HMS is due to an increase of the hole concentration by Ge substitution. In addition, the microstructure of MnSi changes with Ge doping. A GeSi phase appears in the samples with $y \geq 0.025$. These secondary phases may also affect the conduction behavior in HMS.

Figure 3.10a shows κ_L determined by using the aforementioned two-band approach for the (Al,Ge)-doped samples as a function of temperature together with those of the undoped HMS for comparison. All the (Al,Ge)-doped samples show lattice thermal conductivities similar to those of undoped HMS; the difference of the lattice thermal conductivity is within the measurement uncertainty. Figure 3.10b shows the *ZT* of the (Al,Ge)-doped HMS. The (Al,Ge)-doped sample with y = 0.015 exhibits a maximum *ZT* of 0.57 at 823 K, which is comparable to the *ZT* of the optimized Al-doped HMS at 823 K. The *ZT* values decrease with increased Ge concentration, which is due to the reduced power factor. The (Al,Ge)-doped HMS with y = 0.035 shows a ~30% reduction of *ZT* at 800 K as compared to the Al-doped HMS.

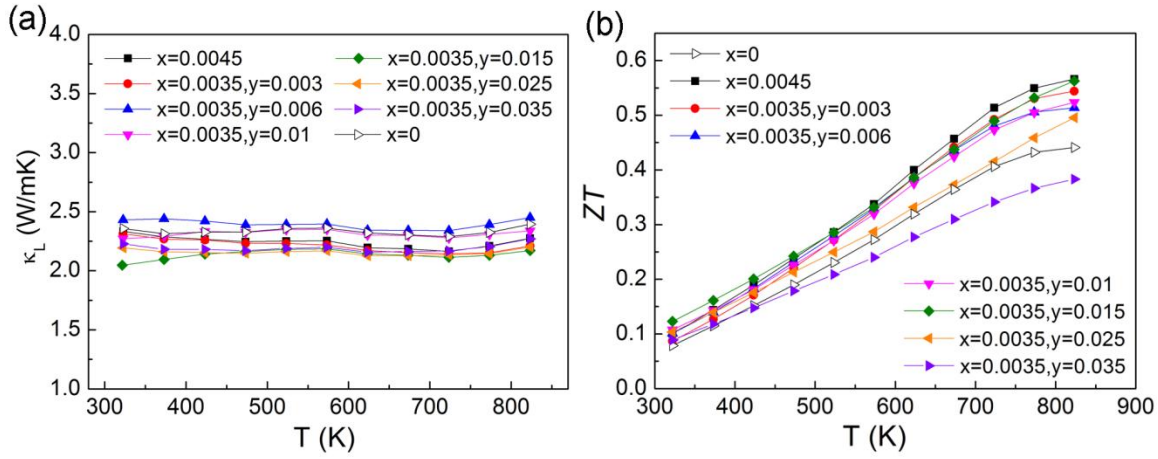

Figure 3.10: (a) The lattice thermal conductivities (κ_L) and (b) the dimensionless figure of merit (*ZT*) of $Mn(Al_xGe_ySi_{1-x-y})_{1.8}$. The relative uncertainty in the *ZT* value is 15%.

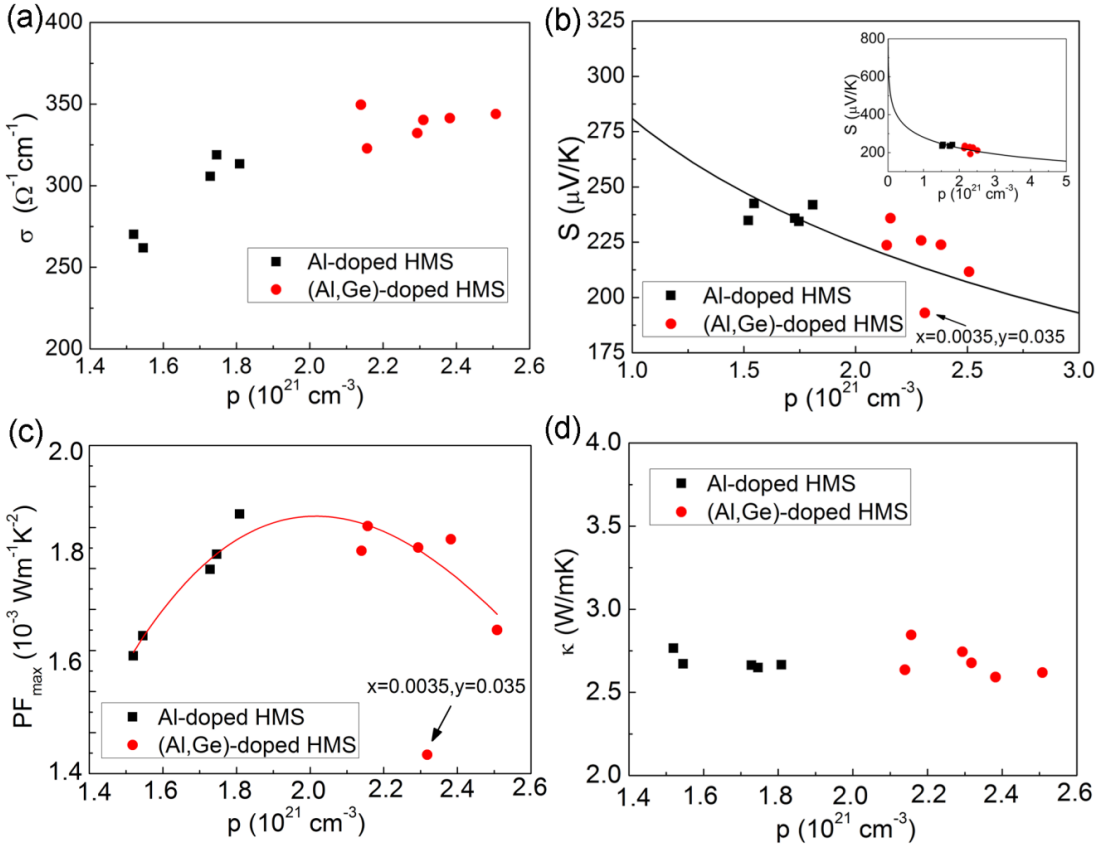

Figure 3.11: (a) Electrical conductivity at 800 K, (b) Seebeck coefficient at 800 K, (c) Peak power factor, and (d) thermal conductivity at 823 K as a function of the hole concentration at room temperature in $Mn(Al_xSi_{1-x})_{1.8}$ and $Mn(Al_{0.0035}Ge_ySi_{0.9965-y})_{1.8}$. The black solid curve in Figure b is the calculated Seebeck at 800 K based on a one-band model with the effective hole mass of HMS $m_h^* = 9\ m_0$. The red solid curve in Figure (c) is the polynomial fitting of the measured data.

In order to better understand the effect of double doping on the TE properties of HMS, electrical conductivity, Seebeck coefficient, peak power factor and thermal conductivity were plotted as a function of the hole concentration (p) in Figure 3.11. The overall trends of the data indicate the electrical conductivity increases with p, whereas the Seebeck coefficient decreases with the p. It is worth noting that the above model would yield the measurement data if the extracted m_h^* and mobility values for each samples are

used. Figure 3.11b shows the calculated Seebeck coefficient based on the one-band model at 800 K with constant $m_h^* = 9\ m_0$ instead of the extracted m_h^*. The experimental data follow the same trend as the model predicts, with the difference likely caused by a variation of m_h^* among the samples of different carrier concentration. In addition, the calculation result indicates that the Seebeck coefficient is a weak function of the carrier concentration where p is higher than 2×10^{21} cm^{-3}. Figure 3.11c shows the maximum power factor as a function of room-temperature hole concentration. It is found that the optimized carrier concentration for HMS is between 1.8×10^{21} and 2.2×10^{21} cm^{-3}. The (Al,Ge)-doped HMS samples show lower power factors because their hole concentrations are higher than the optimum value. It should be pointed out that the unusually low power factor of the (Al,Ge)-doped sample with x=0.0035 and y=0.035 may be related to the formation of GeSi and the increased amount of MnSi as seen from XRD and SEM analysis (Figure 3.6 and 3.7). The thermal conductivity does not change appreciably with carrier concentration in the doped HMS.

3.5 SUMMARY

$Mn(Al_xSi_{1-x})_{1.8}$ and $Mn(Al_{0.0035}Ge_ySi_{0.9965-y})_{1.8}$ were prepared by solid state reaction, followed by ball-milling, and consolidated by SPS. The solid-solution limit of Al is found to be less than x = 0.006, and the solid-solution limit of Ge is less than y = 0.025. Secondary phases (Al-rich or Si-Ge phases) form if the doping concentration exceeding the limits. In addition, the microstructure of MnSi phases was studied on the etched samples. It is found that Al doping does not change the morphology of MnSi significantly. However, the layers of MnSi become curved and nonparallel to each other in the (Al,Ge) doped samples.

Al doping can effectively increase the electrical conductivity and power factor of polycrystalline HMS owing to increased hole concentrations. By adding Ge as the second dopant into Al-doped HMS, the electrical conductivity can be further improved while the Seebeck coefficient is decreased. The thermal conductivities of Al-doped and (Al,Ge)-doped HMS do not change appreciably compared to the undoped HMS. The maximum *ZT* of Al-doped HMS was improved to 0.57 at 823 K for the x = 0.0045 sample. Because increased hole concentration results in a reduction in the power factor, (Al,Ge) doping does not effectively improve the TE performance of HMS as compared to Al doping. The peak power factor of HMS appears to occur at a hole concentration in the range of $1.8\sim2.2\times10^{21}$ cm^{-3}.

The mobility of (Al,Ge)-doped HMS with x=0.0035 and y=0.035 varies approximately as $T^{-3/2}$ above 200 K, suggesting that acoustic phonon scattering is the dominant scattering mechanism. The two-band analysis further shows that the obtained bipolar and electron contributions to the thermal conductivity are negligible compared to the hole contribution at temperatures up to 823 K, the latter of which accounts for about 12% of the total thermal conductivity at 800 K.

Chapter 4: Effects of Re doping on the microstructure and thermoelectric properties of HMS*

4.1 INTRODUCTION

Partial substitution of elements with heavy atoms can reduce the lattice thermal conductivity due to increased alloy scattering resulting from the mass and strain fluctuations.[122,123] This approach has been explored in several recent experimental works on $Mn_{1-x-y}Cr_xRu_ySi_{1.74,}$[124] $Mn_{0.9}Ru_{0.1}Si_y$,[82] and an Rhenium (Re)-substituted HMS sample with an un-specified Re content.[125] Despite the observed reduced thermal conductivity in the reported Re-substituted HMS sample,[125] critical questions remain on the solubility limit of Re in HMS, the correlations between the Re content, the power factor, and lattice thermal conductivity, and most importantly, the extent that the lattice thermal conductivity can be reduced in comparison to the theoretical minimum thermal conductivity of HMS.

In this chapter, a systematic study of the structure–TE property relationship of $Re_xMn_{1-x}Si_{1.8}$ (x = 0-0.24) is presented. In conjunction with the experimental results, theoretical analysis is used to develop a better understanding of the effects of heavy-element substitution on the TE properties. The lattice thermal conductivity for $Re_{0.12}Mn_{0.88}Si_{1.8}$ is effectively suppressed due to increased alloy scattering of phonons to be about 30% lower at 723 K than that of pure HMS samples prepared by the same method. The minimum thermal conductivity model[126] is used to determine that the reduced lattice thermal conductivity has approached the theoretical minimum of Re-

* **X. Chen**, S. N. Girard, F. Meng, E. Lara-Curzio, S. Jin, J. B. Goodenough, J.S. Zhou, and L. Shi, "Approaching the Minimum Thermal Conductivity in Rhenium-substituted Higher Manganese Silicides", *Advanced Energy Materials*, 4, 14, 1400452 (2014)
X.C., L.S., J.S.Z. and J.B.G. designed the research. X.C. synthesized the materials and did the TE measurements. S.N.G., F.M. S.J. did the TEM study. E.L.-C. measured the elastic properties of the sample. X.C. and S.N.G. wrote the manuscript and all authors commented on and edited the manuscript.

substituted HMS. In comparison, the power factor is not affected by the Re substitution at $x \leq 0.04$. These results lead to a 25% *ZT* increase in pure $Re_xMn_{1-x}Si_{1.8}$ with $x = 0.04$ compared to pure HMS.

4.2 EXPERIMENTAL METHODS

4.2.1 Preparation of HMS

Re-substituted HMS, $Re_xMn_{1-x}Si_{1.8}$ ($x = 0$-0.24), were synthesized by solid-state reaction (SSR) with subsequent ball milling (BM) and densification by spark plasma sintering (SPS). The starting materials, Mn (99.95%), Si (99.999%) and Re (99.99%) powders, were purchased from Alfa Aesar. In a typical sample preparation, the powders with nominal chemical composition were sealed in a quartz tube under a vacuum of $\sim 10^{-4}$ Torr. The quartz tube was placed in a furnace and sintered at 1173 K for 48 h. The as-sintered HMS powder was then loaded in a tungsten-carbide jar and ball milled for 60 minutes under argon in a SPEX 8000M Mixer/Mill (SPEX SamplePrep). Subsequently, the ball-milled powders were consolidated into dense bulk samples by SPS at 1123 K for 5 minutes under 60 MPa.

4.2.2 Phase identification and microstructure characterization

The phase purity and crystal structure of the samples were studied by powder X-ray diffraction (PXRD) with a Phillip X'pert diffractometer with Cu K_α radiation ($\lambda = 1.54184$ Å). Several samples were ground to particle size <20 μm and analysed by high-resolution synchrotron PXRD at Argonne National Laboratory on the Advanced Photon Source (APS), beamline 11-BM, having a 12-analyzer Si detector and calibrated radiation wavelength of 0.412455 Å. The morphology and chemical compositions of finely-polished HMS samples were analyzed with a Quanta 650 environmental scanning electron microscope (SEM) with an energy-dispersive X-ray (EDX) spectrometer. A

Zeiss Crossbeam focused ion beam (FIB)/SEM was used to prepare samples that were analyzed by transmission electron microscopy (TEM) in a FEI Titan aberration-corrected (S)TEM electron microscope, operating at 200 kV. The TEM study was carried out by Song Jin's group.

4.2.3 Thermoelectric transport properties measurements

The electrical resistivity and Seebeck coefficient of samples with average dimensions of 1 × 1 × 6 mm and 4 × 4 × 0.5 mm, respectively, were measured in the temperature range of 10–823 K and 80–823 K, respectively, with home-built setups that have been independently calibrated.[11] The thermal diffusivity, α, was measured on disc-shaped samples with dimensions of 6 × 6 × 1 mm by using the laser flash diffusivity method in a Netzsch LFA 457 instrument. The specific heat, C_p, was obtained with a Netzsch 404 differential scanning calorimeter (DSC) with a sapphire standard. The density, ρ, was measured by Archimedes' method. The total thermal conductivity in the range of 320 K to 850 K was calculated as $\kappa = \alpha C_p \rho$. The thermal conductivity below 300 K was measured by a steady-state method on rectangular specimens (0.5 × 0.5 × 3 mm). All three transport properties were measured along the direction parallel to the SPS pressing direction. The room-temperature Hall coefficient measurements were performed with a Physical Properties Measurement System (PPMS, Quantum Design) with the magnetic field sweeping between ±2 T. Because of the high carrier concentration of the degenerately doped HMS samples, the carrier concentration p and Hall mobility were calculated as $p = -(1/eR_H)$ and $\mu_H = \sigma R_H$, respectively, without accounting for the minority carriers. The sound velocities and elastic modulus were measured by resonant ultrasound spectroscopy at Oak Ridge National Laboratory (ORNL).

4.3 PHASE AND MICROSTRUCTURES OF RE-DOPED HMS

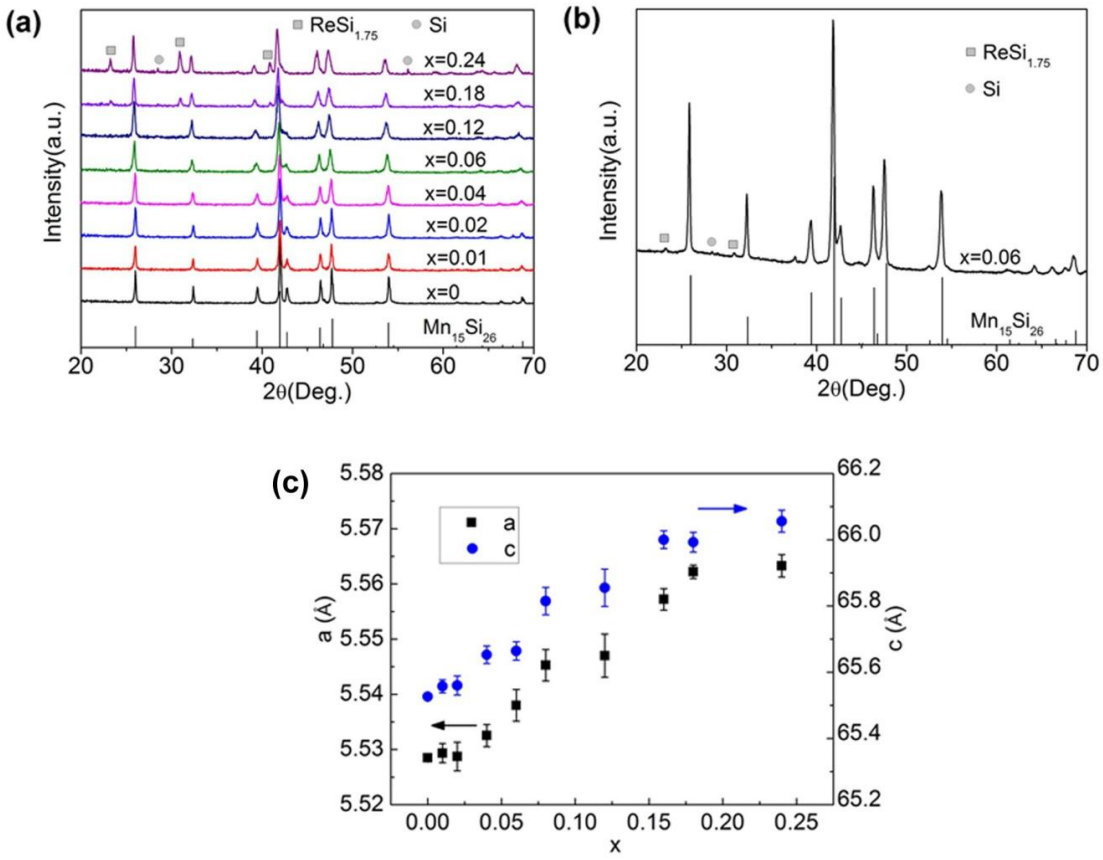

Figure 4.1: (a) The XRD patterns of various $Re_xMn_{1-x}Si_{1.8}$ samples after SPS. (b) High resolution synchrotron XRD of the $Re_{0.06}Mn_{0.94}Si_{1.8}$ sample. (c) The measured mean lattice parameters of $Re_xMn_{1-x}Si_{1.8}$ as a function of x.

Figure 4.1a shows the XRD patterns of the bulk samples obtained after SPS. It can be seen that Re readily substitutes for Mn to obtain $Re_xMn_{1-x}Si_{1.8}$ for $x \leq 0.12$. Diffraction peaks from Si and $ReSi_{1.75}$ can be discerned in the samples with higher Re concentrations ($x \geq 0.18$). However, high-resolution synchrotron XRD performed on the

sample with x = 0.06 (Figure 4.1b) reveals that the second phase $ReSi_{1.75}$ is formed even in the samples with low Re concentrations. With increasing Re concentration, the diffraction peaks from HMS become increasingly broad. As discussed below, such broadening is attributed to locally inhomogeneous compositions in the material. In addition, the intensity of the (11γ) peak at $2\theta = 42.8^{o}$ decreases with increasing Re content, where γ is the number of Si atoms in the formula of different HMS phases. It has similarly been reported that the intensity and position of this peak are sensitive to the doping concentration in Ge-doped HMS.[86] The HMS powders synthesized are usually a mixture of several HMS phases with different *c* lattice parameters rather than a pure single HMS phase.[96] Because of this reason, the lattice parameters of all samples were calculated from the XRD peak positions on the premise that the material was an average phase of $Mn_{15}Si_{26}$. It should be noted that the as-obtained lattice parameters are the mean values of a locally inhomogeneous material.[84] Both *a* and *c* lattice parameters increase monotonically up to x = 0.18 as shown in Figure 4.1c, which is due to the larger radius of Re (r_{Re}= 1.37 Å) as compared to that of Mn (r_{Mn}= 1.27 Å).[127] Since the mean lattice parameters do not change as the Re concentration is increased beyond x = 0.18, as is shown in Figure 4.1c, it can be concluded that the solubility limit of Re in HMS is reached at x = 0.18 according to the Vegard's law.

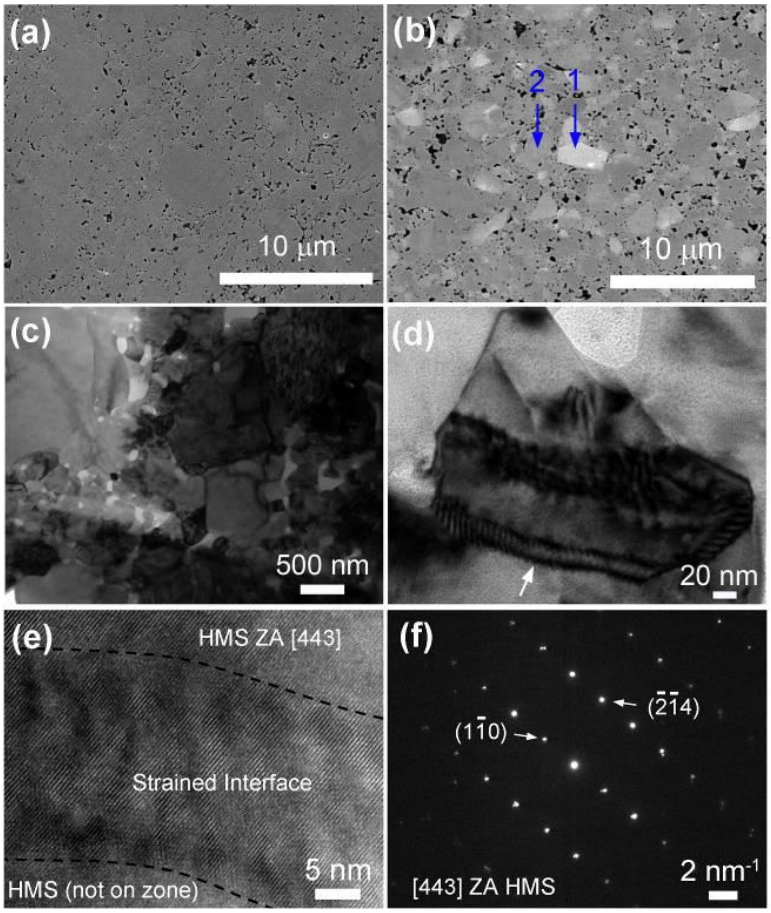

Figure 4.2: SEM images of (a) the pure HMS and (b) the $Re_{0.04}Mn_{0.96}Si_{1.8}$ sample after SPS. The blue arrows in (b) point to the regions where the EDS analysis was performed. (c) and (d) Zero-beam bright-field TEM images of the $Re_{0.04}Mn_{0.96}Si_{1.8}$ sample. The white arrow in (d) points to the strain locations. (e) High-resolution TEM of the $Re_{0.04}Mn_{0.96}Si_{1.8}$ sample. (f) The selected area electron diffraction of (e) obtained along the [443] zone axis (ZA). The SAED pattern was indexed based on the structure of the simplest HMS phase, Mn_4Si_7.

Figure 4.2 shows the microstructures of the bulk samples prepared by SPS. In Figure 4.2a and 4.2b, the comparison of SEM micrographs of pure HMS with Re-substituted HMS (x = 0.04) reveals an increased compositional inhomogeneity in the Re-substituted HMS samples as evidenced by differences in contrast resulting primarily from the incorporation of Re. EDS analysis reveals that the contrast differences are related to a

compositional variation. The atomic ratio in region 1 (bright area) of Figure 4.2b contains a higher concentration of Re, with the atomic ratio between Re, Mn and Si being Re: Mn: Si = 7: 22: 71, whereas the composition of the region 2 (dark area) of Figure 4.2b is relatively Re deficient, Re: Mn: Si = 2: 31: 67. Analysis of multiple grains reveals that the Re substitution is essentially the same within a grain, but that the Re concentration can vary considerably between grains. As a result, the observed broadening of the XRD peaks with increasing Re incorporation (Figure 4.1a) has been attributed to the inhomogeneous distribution of Re within the collection of HMS grains in the SPS samples. It should be noted that such inhomogeneous distribution of substitution elements has also been observed in several other doped NCL phases, such as $Ru_{1-x}Re_xSi_y$,[128] $Mn_{1-x}Cr_xSi_{\sim 1.7}$,[84] and $Ru_{1-x}Mn_xSi_y$.[82]

To better understand the microstructure, the Re-substituted sample with x = 0.04 was examined with transmission electron microscopy (TEM). Figure 4.2c is a typical low-magnification TEM image of the sample. The sample exhibits a broad particle size distribution, ranging from ~50 nm to ~5 μm. The highly energetic process of ball milling and SPS introduces considerable strain on the surface of the HMS grains, which become randomly distributed throughout the sample (Figure 4.2c). Strain is alleviated at the interfaces between HMS grains by regularly spaced dislocations, as shown in the strain fields around the particle in Figure 4.2d and 4.2e. Figure 4.2e shows the interface between two HMS grains and strain dislocations at higher resolution. The top portion of the sample is along the [443] zone axis of HMS, shown in the selected-area electron diffraction (SAED) in Figure 4.2f. The total thickness of the interfacial strain-field region between HMS grains is observed to be ~25 nm. The adjacent HMS grain, shown at the bottom of the image in Figure 4.2e, lies on a different crystallographic zone axis, resulting in a loss of lattice contrast at the bottom of the image.

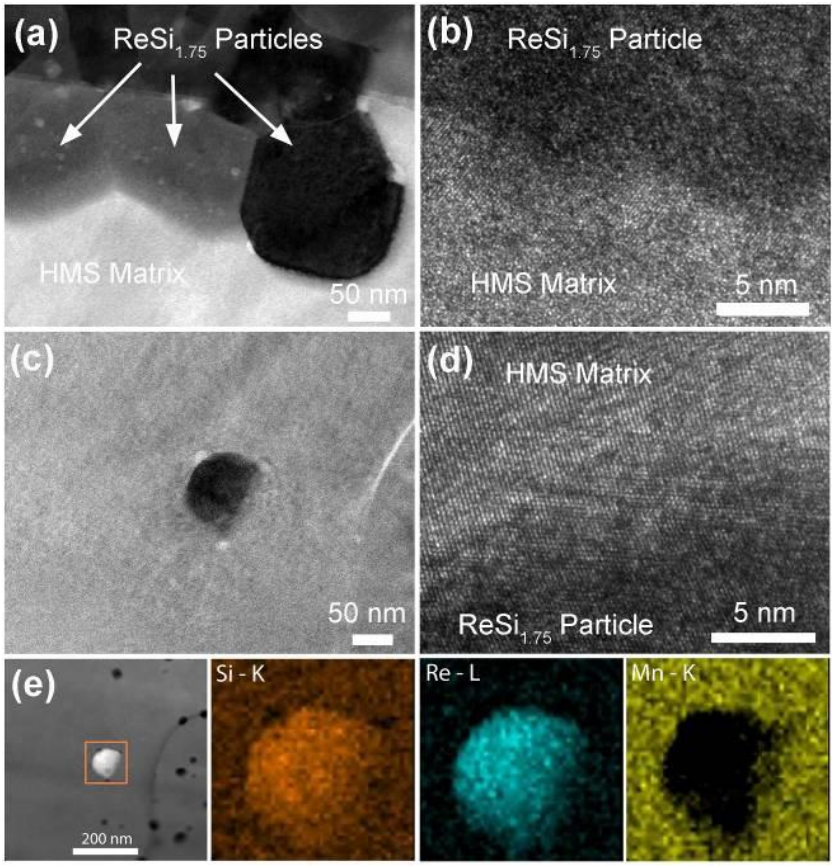

Figure 4.3: (a) TEM image of $Re_{0.04}Mn_{0.96}Si_{1.8}$ showing the embedded $ReSi_{1.75}$ nanoparticles. (b) The high-resolution TEM of the interface between $ReSi_{1.75}$ and HMS. (c) TEM image of an embedded $ReSi_{1.75}$ nanoparticle. (d) The high-resolution TEM of the interface between $ReSi_{1.75}$ and HMS. (e) Elemental maps of $ReSi_{1.75}$ nanoparticle.

$ReSi_{1.75}$ particles with size generally in the range of 50-200 nm can be observed to be dispersed within the matrix of samples with x as low as 0.04 (Figure 4.3), in agreement with high-resolution XRD results indicating that while Re does alloy with HMS, there also exists some phase immiscibility that produces small inclusions of $ReSi_{1.75}$. The larger $ReSi_{1.75}$ particles observed in Figure 4.3a and 4.3b are randomly oriented with respect to each other and the HMS matrix. Smaller $ReSi_{1.75}$ particles with size less than ~50 nm show improved alignment within the HMS matrix, evidenced by

lattice contrast observed along the same zone in the $ReSi_{1.75}$ particle as in the HMS matrix, Figure 4.3c and 4.3d. The coherency and epitaxy of the $ReSi_{1.75}$ cannot be determined, resulting from the completely random orientations of the grains from sample preparation and the relatively small area afforded by the focused ion beam (FIB) preparation of the TEM sample. EDS spectra confirm that the small inclusions are rich in Re and deficient in Mn, according to Figure 4.3e.

4.4 ELECTRONIC TRANSPORT PROPERTIES OF RE-DOPED HMS

Hall coefficient measurements were carried out for the Re-substituted samples. As shown in Figure 4.4a, the measured room-temperature hole concentration (p) appears to increase slightly with Re substitution, although the difference is comparable to the measurement uncertainty. Since Re is isoelectronic with Mn, the increase of p is unexpected. Several first-principles calculations[14] indicate that the band structure of HMS strongly depends on the atomic arrangement and the existence of stacking faults. Recently, Allam *et al.*[87] found that the density of states (DOS) of HMS changes by Re substitution according to a first-principles calculation. Moreover, Zhou *et al.*[86] reported that the hole concentration was increased in Ge-doped HMS even though Ge is isoelectronic with Si. They found that Ge substitution can disturb the arrangement of the Si subcells and possibly form stacking faults in the HMS. Thus, Re substitution is likely to alter the band structure and possibly the Fermi level or DOS near the Fermi level, potentially increasing the hole concentration. It should also be noted that the formation of defects at a higher concentration of Re could also change the hole concentration of HMS. However, a detailed first-principles calculation is needed to better understand the cause of the increased hole concentration in Re-substituted HMS. In addition, Figure 4.4c

shows that the hole concentration is essentially independent of temperature for the samples with x = 0, 0.04 and 0.12. This feature is characteristic of a degenerate *p*-type semiconductor.

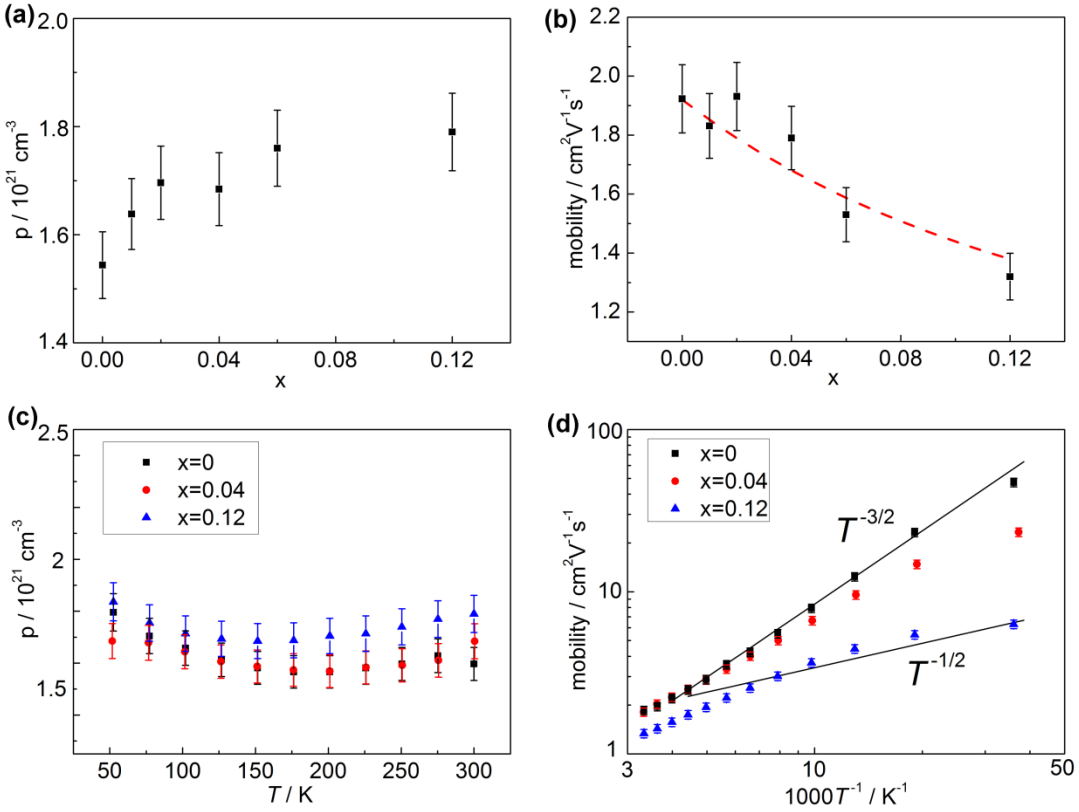

Figure 4.4: (a) Carrier concentration and (b) mobility of $Re_xMn_{1-x}Si_{1.8}$ as a function of x at room temperature. (c) Carrier concentration and (d) mobility of $Re_xMn_{1-x}Si_{1.8}$ with x = 0, 0.04 and 0.12 as a function of temperature. The red dashed line in (b) is the fitting of the measured mobility according to equation (4.1).

As shown in Figure 4.4b, the room-temperature mobility (μ_H) of Re-substituted samples decreases with the increase of Re content, which can be attributed to enhanced alloy scattering. In comparison, carrier scattering by $ReSi_{1.75}$ particles is not considered to be important here because the carrier mean free path of HMS is reported to be about

several nm,[90] which is much smaller than the size or inter particle spacing of $ReSi_{1.75}$ particles. Alloy scattering adds a neutral impurity scattering term (μ_{alloy}) to the ionized impurity and phonon scattering. Thus, the total mobility (μ) is given by[129]

$$\frac{1}{\mu} = \frac{1}{\mu_o} + \frac{1}{\mu_{alloy}} \quad , \tag{4.1}$$

where the μ_o is the mobility in pure HMS with x = 0 due to scattering by phonons, grain boundary, and ionized impurities, and μ_{alloy} is the additional alloy scattering in $Re_xMn_{1-x}Si_{1.8}$, and is proportional to $[x/(1-x)]^{-1}$ for $Re_xMn_{1-x}Si_{1.8}$, where *x* is the mole fraction of the substitution element in the alloy.[130] By fitting the composition dependence of mobility at room temperature (Figure 4.4b) with equation (4.1), the alloy scattering mobility term at room temperature is determined to be about $\mu_{alloy} = 0.52/[x(1-x)]$ $cm^2 V^{-1} s^{-1}$.

Figure 4.4d shows the mobility of the Re-substituted samples as a function of temperature. For pure HMS, the mobility μ_H varies approximately as $T^{-3/2}$ for temperatures above 50 K. This result indicates that acoustic phonon scattering[131] is the dominant carrier scattering mechanism in HMS above 50 K compared to alloy scattering and ionized impurity scattering, which yield $\mu_H \propto T^{-1/2}$ [131] and $\mu_H \propto T^{3/2}$,[14,117,129,132] respectively. For the Re-substituted sample with x = 0.12, the mobility varies approximately as $T^{-1/2}$ for temperatures below 100 K, suggesting that both phonon scattering and alloy scattering are important in this temperature range. Nevertheless, the mobility of all samples follows the relationship of $\mu_H \propto T^{-3/2}$ above 200 K, which suggests that acoustic phonon scattering is dominant at high temperatures.

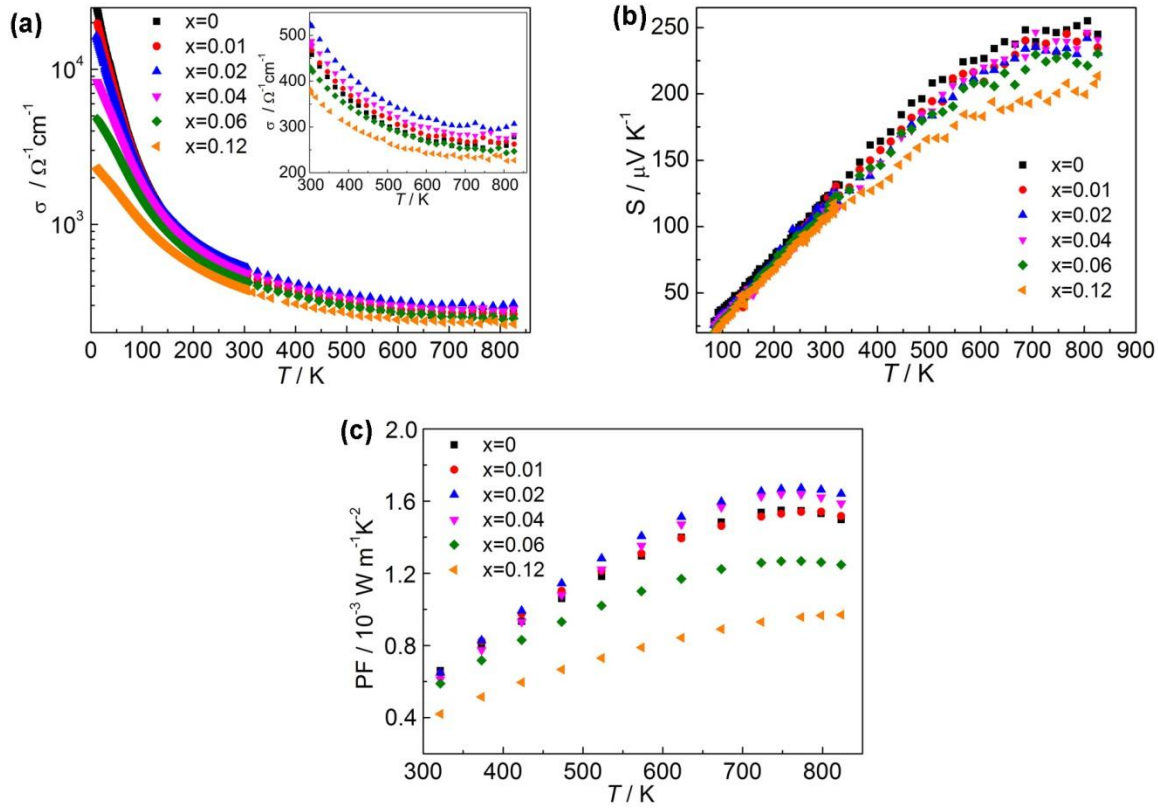

Figure 4.5: Temperature dependence of transport properties of various $Re_xMn_{1-x}Si_{1.8}$ samples: (a) electrical conductivity with 5% uncertainty, (b) Seebeck coefficient with 5% uncertainty, and (c) power factor with 11% uncertainty. The inset of (a) is the electrical conductivity in the temperature range of 300 to 850 K.

The temperature dependence of electrical conductivity (σ) and Seebeck coefficient (S) for $Re_xMn_{1-x}Si_{1.8}$ are plotted in Figure 4.5a and 4.5b, respectively. The room-temperature electrical conductivity increases with the Re content from 475 Ω^{-1} cm^{-1} in pure HMS to 524 Ω^{-1} cm^{-1} in the sample with x = 0.02. As the Re content increases further, the room-temperature electrical conductivity decreases. The initial increase of the room-temperature electrical conductivity is caused by the increased carrier concentration (Figure 4.4a); whereas the decrease of the room-temperature electrical conductivity at higher Re contents can be attributed to the reduced mobility (Figure 4.4b). In addition,

the electrical conductivity at temperatures below 100 K decreases with Re substitution, which results from enhanced alloy scattering (Figure 4.4d). The S of all samples decreases monotonically with an increase in the Re content, in agreement with the measured increase in the hole concentration. The power factor (PF) of $Re_xMn_{1-x}Si_{1.8}$ is calculated by using polynomial fits to the measured σ and S and is displayed in Figure 4.5c. For the samples with $x \leq 0.04$, the PF does not change significantly as compared to the pure HMS, which is a consequence of the improved σ and reduced S. However, the samples with higher Re content (x = 0.06 and 0.12) show lower a PF than other samples, which is due to the much reduced S.

In order to better understand the carrier transport features in Re-substituted HMS, the room-temperature Fermi level (E_F), hole density of states effective mass (m_h^*), and Lorenz number (L) are extracted from the measured electrical conductivity, the Seebeck coefficient, and Hall coefficient. These are listed together with other room-temperature properties in Table 4.1. This analysis is based on a two-band model where charge-carrier scattering is assumed to be dominated by acoustic phonon scattering and grain-boundary scattering. The Lorenz number is calculated from the model as $L=\kappa_E/\sigma T$ at room temperature. Here, the extracted m_h^* of pure HMS is $9.6m_o$, where m_o is the free-electron mass. This m_h^* value is comparable to the literature values of $12m_o$ reported by Nishida.[117] In addition, the extracted hole effective mass decreases with the increase of Re content, with the smallest $m_h^* = 8.7m_o$ found in the sample with x = 0.12. The Fermi level is measured from the conduction band edge and is negative when it is in the band gap or valence band. The Fermi level of pure HMS is 0.81 eV, which is 0.04 eV below the valence band edge as the band gap of HMS is 0.77 eV.[14] The extracted Fermi level decreases slightly as the Re content increases because the measured hole concentration increases with increasing Re content. The L values were calculated to be in

the range from 1.3 to 1.7 $\times 10^{-8}$ $V^2 K^{-2}$, which is lower than the Sommerfeld value of 2.44×10^{-8} $V^2 K^{-2}$ for a metal.

Table 4.1: Density and room temperature electrical transport properties of various $Re_xMn_{1-x}Si_{1.8}$ samples.

Nominal composition	Density ($g\ cm^{-3}$)	σ ($\Omega^{-1}\ cm^{-1}$)	S ($\mu V\ K^{-1}$)	R_H ($10^{-9}\ m^3\ C^{-1}$)	p ($10^{21}\ cm^{-3}$)	μ_H ($cm^2\ V^{-1}\ s^{-1}$)	m_h^* / m_o	E_F (eV)	L ($10^{-8}\ V^2\ K^{-2}$)
x=0	4.87	475	122	4.05	1.54	1.92	9.6	0.81	1.54
x=0.01	4.90	480	115	3.81	1.64	1.83	9.2	0.82	1.43
x=0.02	4.95	524	114	3.69	1.70	1.93	9.4	0.82	1.35
x=0.04	4.97	482	108	3.72	1.68	1.79	8.9	0.82	1.35
x=0.06	4.98	430	106	3.56	1.76	1.53	8.8	0.83	1.50
x=0.12	5.15	378	104	3.50	1.79	1.32	8.7	0.83	1.67

4.5 THERMAL PROPERTIES AND THERMOELECTRIC FIGURE OF MERIT

The heat capacity (C_p), thermal diffusivity (α), and total thermal conductivity (κ) for $Re_xMn_{1-x}Si_{1.8}$ are shown in Figure 4.6. The C_p at 800 K decreases from 0.69 J $g^{-1} K^{-1}$ in the pure HMS to 0.60 J $g^{-1} K^{-1}$ in the sample with x = 0.12. According to the Dulong-Petit Law, the high-temperature limit of heat capacity is $3Nk_B/M$, where N, k_B and M are the number of atoms per mole, the Boltzmann constant, and the molar mass of the compound, respectively. Since the atomic mass of Re (186.2 g mol^{-1}) is larger than that of Mn (54.9 g mol^{-1}), the Dulong-Petit limit of Re-substituted HMS should be lower than that of pure HMS, which is consistent with the experimental results. The α of all the samples decreases with increasing Re content. The total thermal conductivity is obtained as $\kappa = \alpha C_p \rho$, where ρ is the density of the as-prepared samples as shown in Table 4.1. Although ρ increases with the Re content, the total thermal conductivity was suppressed by Re substitution due to both decreased C_p and α. A low κ of 1.7 W $m^{-1} K^{-1}$ at 320 K was achieved in the sample with x = 0.12, which is about 30% lower than that of pure HMS prepared with the same method. It is noted that the κ at around 300 K measured by

the steady-state method is slightly higher than that obtained by the laser flash diffusivity method. This discrepancy is due to the measurement errors of these two methods. The uncertainties of the steady-state method and the laser flash method are about 15% and 7%, respectively. The larger uncertainty for the steady-state method is caused by radiation losses near room temperature and a low resolution of the thermocouples used at low temperatures , which can result in an overestimated thermal conductivity near room temperature,[132] in addition to the uncertainty in measuring the distance between differential thermocouples .

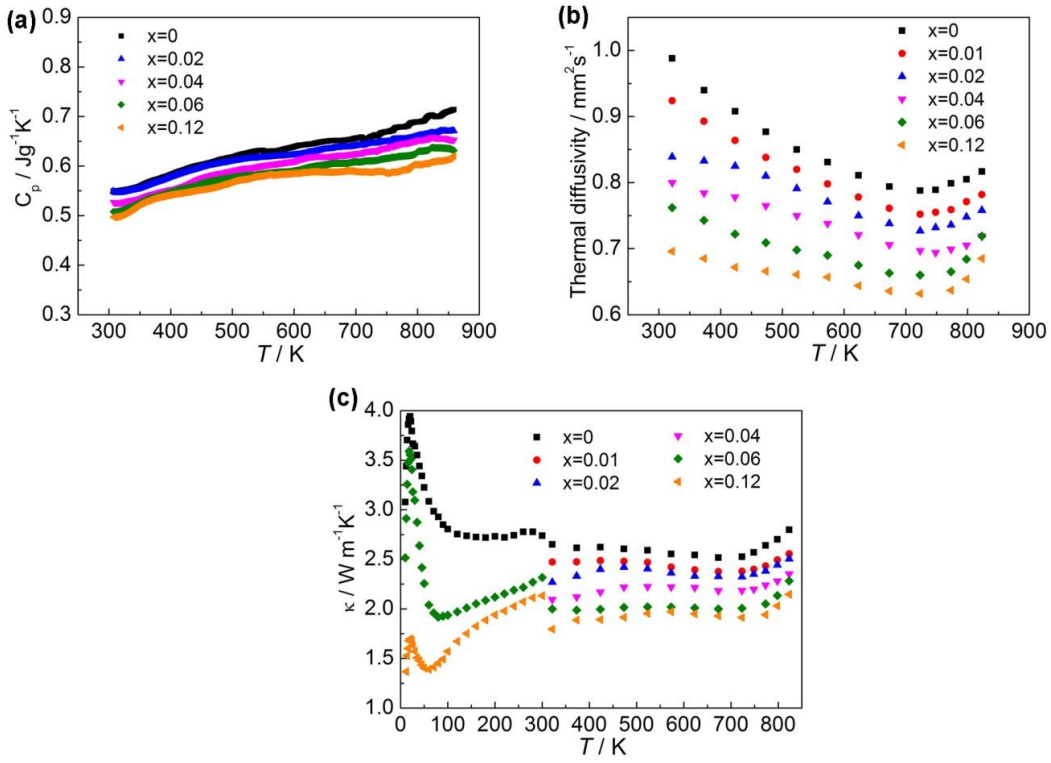

Figure 4.6: Temperature dependence of (a) specific heat with 6% uncertainty, (b) thermal diffusivity with 3% uncertainty and (c) total thermal conductivity, with 7% uncertainty for the laser flash method and 15% uncertainly for the steady-state method, of various $Re_xMn_{1-x}Si_{1.8}$ samples.

The lattice thermal conductivity (κ_L) can be obtained by subtracting the electronic thermal conductivity (κ_E) from the total thermal conductivity. For temperatures higher than 300 K, κ_E is calculated with the hole, electron, and bi-polar contributions included. For temperatures lower than 300 K, the room-temperature L values listed in Table 1 have been used to calculate κ_E via the Wiedemann-Franz Law $\kappa_E = L\sigma T$. The κ_L at 723 K as a function of the Re concentration and κ_L for $Re_xMn_{1-x}Si_{1.8}$ at all measured temperatures are shown in Figure 4.7a and 4.7b, respectively. It is clear that the κ_L is dominant in the HMS samples as compared to κ_E at temperatures up to 800 K. The κ_L decreases considerably with increasing Re content over the measured temperature range, indicating that alloying of Re at Mn sites is an effective approach to reducing the κ_L in HMS compounds. The lowest κ_L is obtained for $Re_{0.12}Mn_{0.88}Si_{1.8}$, yielding the value of 1.6 W m^{-1} K^{-1} at 723 K, which is about 30% lower than that of pure HMS synthesized with the same method. The reduction of κ_L is mainly due to the point defect scattering for phonons as a result of mass fluctuations and associated perturbation in the interatomic force constant. In addition, the reduction of κ_L may also have a contribution from the formation of $ReSi_{1.75}$ nanoparticles and the many nanoscale interfaces that can scatter low to mid-frequency phonons because the low-frequency phonons can make an appreciable contribution to the thermal conductivity of the HMS samples and can have a mean free path comparable to the size and separation between $ReSi_{1.75}$ nanoparticles.

To understand better the effect of Re substitution on the lattice thermal conductivity, the experimental result is compared with a calculation based on a model by Callaway *et al.*[133] At temperatures higher than the Debye temperature (θ_D), phonon grain boundary scattering may be ignored in polycrystalline materials with grain sizes larger than the phonon-phonon scattering mean free path. If only Umklapp and point defect

scattering are considered, the ratio of κ_L of the crystal with disorder to that without disorder (κ_{L0}) can be expressed as[134,135]

$$\frac{\kappa_L}{\kappa_{L0}} = \frac{\tan^{-1}(u)}{u}, \quad u^2 = \frac{\pi^2 \theta_D \Omega}{h v_a^2} \kappa_{L0} \Gamma, \tag{4.2}$$

where u, v_a, Ω, h, and Γ are the disorder scaling parameter, the average sound velocity, the average volume per atom, the Plank's constant, and the disorder scattering parameter, respectively. The disorder scattering parameter Γ can be calculated as $\Gamma_{calc} = \Gamma_M + \Gamma_S$, where Γ_M and Γ_S are scattering parameters due to mass and strain-field fluctuations, respectively. For $Re_xMn_{1-x}Si_{1.8}$, Γ_M and Γ_S are given by[122,134]

$$\Gamma_M = \frac{1}{2.8}\left(\frac{\overline{M}}{\overline{\overline{M}}}\right)^2 x(1-x)\left(\frac{M_1 - M_2}{\overline{M}}\right)^2, \tag{4.3}$$

$$\Gamma_S = \frac{1}{2.8}\left(\frac{\overline{M}}{\overline{\overline{M}}}\right)^2 x(1-x)\varepsilon\left(\frac{r_1 - r_2}{\bar{r}}\right)^2, \tag{4.4}$$

$$\overline{M} = M_1 x + M_2(1-x), \tag{4.5}$$

$$\overline{\overline{M}} = \frac{1}{2.8}\overline{M} + \frac{1.8}{2.8}M_3, \tag{4.6}$$

and

$$\bar{r} = r_1 x + r_2(1-x), \tag{4.7}$$

where M_1, M_2, and M_3 are the atomic mass values of Re, Mn, and Si, respectively, r_1 and r_2 are the atomic radius of Re and Mn, respectively, x is the Re content , and ε is a function of the Grüneisen parameter γ, as given below.

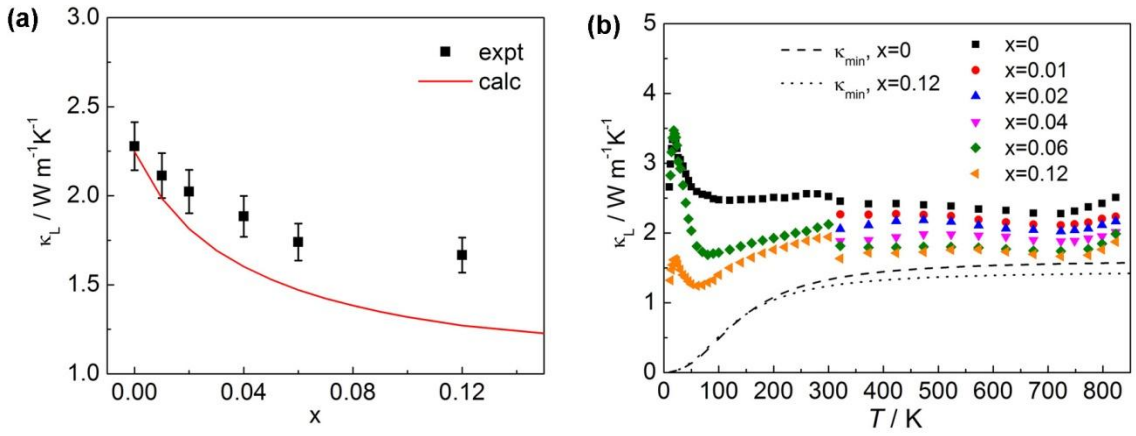

Figure 4.7: (a) Lattice thermal conductivity of various $Re_xMn_{1-x}Si_{1.8}$ samples at 723 K as a function of x. The red line is the calculated lattice thermal conductivity based on the Callaway model. (b) Temperature dependence of lattice thermal conductivity of $Re_xMn_{1-x}Si_{1.8}$. The dashed line and dotted lines are the calculated minimum lattice thermal conductivity of pure HMS and $Re_{0.12}Mn_{0.88}Si_{1.8}$, respectively.

Table 4.2: Elastic properties of HMS at room temperature.

Parameters	units	values
Longitudinal sound velocity (v_l)	m s^{-1}	7545
Shear sound velocity (v_s)	m s^{-1}	4615
Average sound velocity (v_a)	m s^{-1}	5095
Young's modulus (E)	Gpa	245
Debye temperature (θ_D)	K	660
Poisson ratio (υ_p)	/	0.2
Grüneisen parameter (γ)	/	1.29

In order to determine the Debye temperature, the sound velocity and the parameter ε, the elastic properties of HMS were measured and are listed in Table 4.2. The average sound velocity v_a can be calculated from the measured longitudinal (v_l) and shear (v_s) sound velocities by[136]

$$v_a = \left(\frac{1}{3} \left[\frac{1}{v_l^{\,3}} + \frac{2}{v_s^{\,3}} \right] \right)^{-1/3}, \tag{4.8}$$

The Debye temperature θ_D can be obtained as:[135]

$$\theta_D = \frac{h}{k_B} \left[\frac{3n}{4\pi} \right]^{1/3} v_a, \tag{4.9}$$

where n is the number density of atoms. The parameter ε of equation (4.4) is given by[135]

$$\varepsilon = \frac{2}{9} \left(\frac{6.4\gamma(1+\upsilon_p)}{(1-\upsilon_p)} \right)^2, \tag{4.10}$$

where υ_p is the Poisson ratio, and γ can be obtained from[137]

$$\gamma = \frac{3}{2} \left(\frac{1+\upsilon_p}{2-3\upsilon_p} \right). \tag{4.11}$$

As listed in Table 4.3, Γ_{calc} increases with Re substitution. In addition, the calculated Γ_M is much larger than Γ_S, suggesting that the mass-contribution dominates the

contribution resulting from the strain-field fluctuation. Using the measured κ_L of pure HMS, which is κ_{L0} = 2.3 W m^{-1} K^{-1}, and Γ_{calc}, the lattice thermal conductivity due to point defect scattering can be calculated from equation (4.2). The calculated result (Figure 4.7a) indicates that the κ_L value at 723 K can be reduced to about 1.2 W m^{-1} K^{-1} when x = 0.18, which is about half of the value for pure HMS prepared with the synthesis method reported here. The experimental data follow the same trend as the model prediction, although the experimental data are somewhat higher than the calculated results. If the measured κ_L are used to extract u, the experimental Γ (Γ_{expt}) values can be estimated from equation (4.2). The obtained Γ_{expt} is about a factor of two smaller than Γ_{calc}, as shown in Table 4.3. The discrepancy could be due to the Debye approximation used in this model, which is only valid if the temperature is much lower than θ_D. In addition, this model does not accurately account for the contribution of the optical phonon modes to the thermal conductivity, which can be important in the complex HMS structure at high temperatures. Nevertheless, the reduction of κ_L by Re substitution is confirmed by both experimental results and theoretical analysis.

Table 4.3: Calculated disorder parameter (u) and the scattering parameters of $Re_xMn_{1-x}Si_{1.8}$.

Nominal composition	u	Γ_{expt}	Γ_{calc}	Γ_M	Γ_S
x=0.01	0.47	0.022	0.044	0.042	0.002
x=0.02	0.59	0.034	0.084	0.081	0.003
x=0.04	0.78	0.060	0.158	0.151	0.007
x=0.06	1.05	0.108	0.222	0.212	0.010
x=0.12	1.22	0.145	0.367	0.347	0.020

We have further evaluated the minimum κ_L of HMS using the model of Cahill *et al.*[126]

$$\kappa_{\min} = \left(\frac{\pi}{6}\right)^{1/3} k_B n^{2/3} \sum_i v_i \left(\frac{T}{\theta_i}\right)^2 \int_0^{\theta_i/T} \frac{x^3 e^x}{\left(e^x - 1\right)^2} dx \,, \tag{4.12}$$

where the summation is over two transverse and one longitudinal polarizations, the cutoff frequency θ_i is expressed as $\theta_i = v_i(h/k_B)(3n/4\pi)^{1/3}$, and v_i is the sound velocity for each polarization. This equation is developed based on the Einstein model to calculate the minimum lattice thermal conductivity of highly disordered solids, where thermal transport is characterized by random walk of energy between localized oscillators of varying frequencies and the dominant energy transport is between nearest neighbors. The model is also based on the Debye approximation of the phonon dispersion. Although this model relies on overly simplified assumptions of the relaxation process, it has obtained thermal conductivity values consistent with measurement results of amorphous materials.[126]

With θ_D = 660 K and v_a = 5095 m s^{-1}, the $\kappa_{\min}$ for pure HMS is calculated to be about 1.6 W m^{-1} K^{-1} above 700 K as shown in Figure 4.7b (dashed line). For $Re_{0.12}Mn_{0.88}Si_{1.8}$, we have evaluated θ_D as[138]

$$\frac{\theta_D\left(\mathrm{Re}_{0.12}\mathrm{Mn}_{0.88}\mathrm{Si}_{1.8}\right)}{\theta_D\left(\mathrm{MnSi}_{1.8}\right)} = \left[\frac{\left(M_2\right)^{3/2} + 1.8(M_3)^{3/2}}{0.12(M_1)^{3/2} + 0.88\left(M_2\right)^{3/2} + 1.8(M_3)^{3/2}}\right]^{1/3}. \tag{4.13}$$

According to equations (4.9) and (4.13), the θ_D and v_a for $Re_{0.12}Mn_{0.88}Si_{1.8}$ are calculated to be 593 K and 4578 m s^{-1}, respectively. Therefore, the $\kappa_{\min}$ for $Re_{0.12}Mn_{0.88}Si_{1.8}$ yields about 1.4 W m^{-1} K^{-1} above 700 K as shown in Figure 4.7b (dotted line). This value is comparable to those of amorphous glass. Moreover, it is noted that the measured κ_L of $Re_{0.12}Mn_{0.88}Si_{1.8}$ approaches the calculated $\kappa_{\min}$.

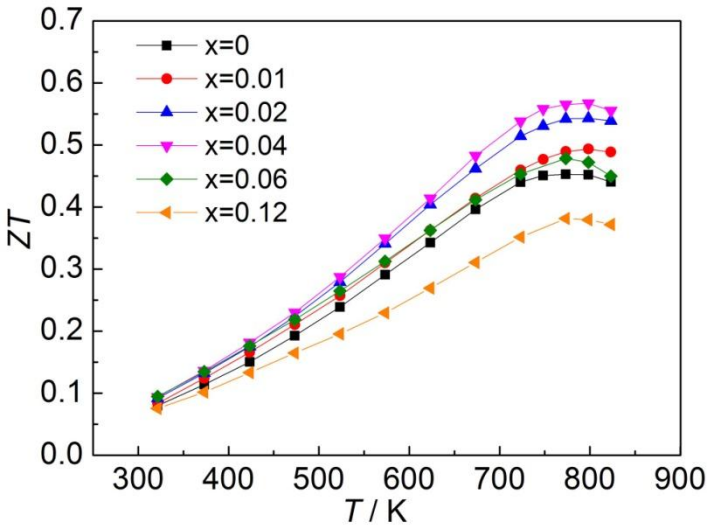

Figure 4.8: The dimensionless figure of merit (*ZT*) of various $Re_xMn_{1-x}Si_{1.8}$ samples with 13% uncertainty.

Finally, the figure of merit (*ZT*) of $Re_xMn_{1-x}Si_{1.8}$ is displayed in Figure 4.8. Re substitution suppresses the lattice thermal conductivity of HMS considerably and has relatively little influence on the power factor when the Re concentration is x = 0.04 and smaller. The *ZT* value is improved to 0.57±0.08 at about 800 K for x = 0.04. This *ZT* value of the pure $Re_xMn_{1-x}Si_{1.8}$ is ~25% higher than that of pure HMS. The *ZT* value decreases with further increase of the Re content ($x \geq 0.06$) because of a reduction in the power factors. Because the primary role of Re substitution is to reduce the lattice thermal conductivity instead of optimizing the carrier concentration for enhanced power factor, the maximum power factor of $Re_xMn_{1-x}Si_{1.8}$ is still lower than that of (Al,Ge)-doped HMS as discussed in Chapter 3. Since the hole concentration of $Re_{0.04}Mn_{0.96}Si_{1.8}$, 1.68×10^{21} cm^{-3}, is lower than the optimized value found in (Al,Ge)-doped HMS, $1.8\sim2.2 \times 10^{21}$ cm^{-3}, further improvement in *ZT* in Re-substituted HMS may be possible via rational choice of impurity doping elements to optimize the carrier concentration of the $Re_xMn_{1-x}Si_{1.8}$ system.

4.6 SUMMARY

Re-substituted HMS ($Re_xMn_{1-x}Si_{1.8}$) samples were synthesized by solid-state reaction followed by ball-milling and spark plasma sintering. The solubility limit of Re is found to be about x = 0.18 according the Vegard's law. Inhomogeneous distribution of Re were observed by SEM and EDX analysis. X-ray diffraction results indicate that a secondary phase of $ReSi_{1.75}$ was formed even in the sample with Re concentration much lower than the solubility limit. The $ReSi_{1.75}$ nanoparticles with size in the range of 50-200 nm were observed to be dispersed within the HMS matrix.

The carrier concentration and mobility were examined by Hall coefficient measurements. The room-temperature hole concentration increases slightly with Re substitution; while the Hall mobility decreases with increasing Re content due to the increased alloy scattering. The temperature dependence of the mobility for the Re-substituted samples varies approximately as $T^{-3/2}$ for temperatures above 200 K. This result indicates that acoustic phonon scattering is the dominant carrier-scattering mechanism above 200 K compared to alloy scattering and ionized impurity scattering.

The electrical transport properties are modified by isoelectronic alloying of Re at Mn sites. With increasing Re content, the hole concentration increases and the effective hole mass and the mobility decrease. As a consequence, the power factor does not change significantly at low Re concentration ($x \leq 0.04$), but it decreases with further increase of the Re content. Due to both the reduced thermal diffusivity and the reduced specific heat in Re-substituted samples, the lattice thermal conductivity is considerably suppressed. The lowest κ_L of about 1.6 W m^{-1} K^{-1} at 723 K is achieved in the sample with x = 0.12, which is about 30% lower than that of pure HMS. A model developed by Callaway *et al.*[133] was employed to calculate the lattice thermal conductivity of Re-substituted HMS. The experimental results generally follow the trend predicted by the model, suggesting

reduction of κ_L is mainly due to the point defect scattering for phonons as a result of mass fluctuations and associated perturbation in the interatomic force constant. In addition, the minimum κ_L was evaluated with the model of Cahill *et al.*[126] It is found that the experimental values approach the calculated minimum κ_L value of 1.4 W m^{-1} K^{-1} for T $\geq$ 700 K. Compared to pure HMS, the maximum *ZT* is increased by about 25% to 0.57±0.08 at about 800 K in the sample with x = 0.04, which is due to a nearly unchanged power factor and a suppressed thermal conductivity.

Chapter 5: Effects of nanostructuring on the microstructure and thermoelectric properties of HMS*

5.1 INTRODUCTION

Recently, *ZT* improvement has been reported in some nanostructured bulk materials.[23] The *ZT* of nanostructured TE materials can be enhanced as long as the reduction in thermal conductivity due to scattering of phonons from grain boundary exceeds the reduction in power factor due to the increased charge carrier scattering. This approach has been validated in several TE materials, such as $AgPb_mSbTe_{2+m}$,[26] Bi_2Te_3,[27,28] and $Si_{80}Ge_{20}$[29,139] nanostructured bulk materials as well as Bi_2Te_3/Sb_2Te_3 superlattice.[21] These nanostructued bulk materials are usually prepared by the hydrothermal method or high-energy ball milling followed by densification using hot-pressing or spark plasma sintering (SPS).

It is known that increasing phonon scattering at grain boundaries can be used to reduce the thermal conductivity. Early studies of Si-Ge based alloys by Goldsmid, Parrot and Rowe had showed that the thermal conductivity of poly-crystals could be reduced significantly when the grain size in the sample was decreased to several micrometers.[140-142] Recently, Kim *et al.*[143] investigated the grain size effect on the thermoelectric properties of hot-pressed Bi_2Te_3, and found that the lattice thermal conductivity for the sample with an average grain size of 1.2 μm was reduced by 60% compared to that of a single crystal. In one theoretical analysis based on a semi-classical two-band model and Debye approximation for calculating charge and phonon transport, respectively,[90] it is

---

* **X. Chen**, A. Weathers, A. Moore, J.S. Zhou, and L. Shi, "Thermoelectric Properties of Cold-Pressed Higher Manganese Silicides for Waste Heat Recovery", *Journal of Electronic Materials*, 41, 1564-1572 (2012).
X.C., L.S. and J.S.Z. designed the research. X.C. synthesized the materials and did the measurements. A.W., A.M., L.S. and X.C. analyzed the thermal conductivity. X.C. and A.W. wrote the manuscript and all authors commented on and edited the manuscript.

estimated that the *ZT* of HMS can be slight enhanced by reducing the grain size to about 10 nm. However, there is a lack of experimental results to study the size effects on the thermoelectric properties of nanostructured HMS.

In this chapter, the effects of nanostructuring on the TE properties of HMS are presented. The HMS samples with different grain sizes have been prepared by two different methods: (1) cold-pressing and post annealing; (2) ball milling and SPS. The microstructures and TE properties of these samples have been investigated in detail.

5.2 EXPERIMENTAL METHODS

5.2.1 Preparation of HMS

HMS samples were synthesized by solid-state reaction and then cold pressed into pellets. The starting materials, Mn (purity, 99.95%) and Si (purity, 99.999%) powders, were purchased from Alfa Aesar. In a typical procedure, a mixture of stoichiometrically weighed pure elements was first hand-ground with an agate mortar and pestle for 1 h. Subsequently, the powder was sealed in a vacuumed quartz tube. The quartz tube was put in a furnace and sintered at 900 ^{o}C for 48 h. The as-sintered HMS powder was transferred into a hole drilled in a high-density, hard cardboard gasket that was put between two tungsten carbide (WC) anvils of 12 mm in diameter (Figure 5.1) and cold pressed under the maximum non-hydrostatic pressure (P_{max}) of about 3 GPa. The cardboard was purchased from Strathmore Paper Company. Subsequently, the cold-pressed pellets were annealed at different temperatures (500 ^{o}C, 800 ^{o}C, and 1100 ^{o}C) for 6 h in a vacuum-sealed quartz tube. For comparison, HMS pellets were made with a regular die under a relatively low pressure of 300 MPa and annealed at 800 ^{o}C for 6 h.

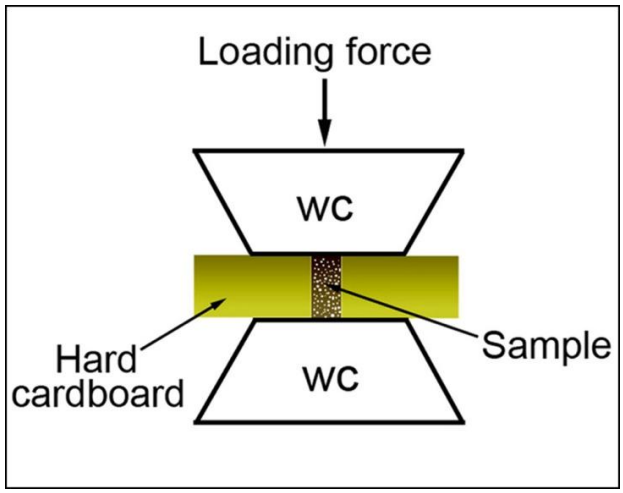

Figure 5.1: Schematic drawing of Bridgman anvils used for cold-pressing samples.

Another group of samples were synthesized through three steps, *i.e.* melting, ball milling (BM), and SPS. First, powders with nominal chemical composition $MnSi_{1.78}$ were mixed, sealed in a vacuumed quartz tube, and heat-treated in a furnace at 900 ^{o}C for 24 h, then at 1300 ^{o}C for 10 h. Subsequently, the obtained ingot was loaded into a WC jar and ball milled in argon by a SPEX 8000M Mixer/Mill (SPEX SamplePrep). The grain sizes were controlled by means of changing the BM time from 2 to 54 hours. Finally, the ball-milled powders were consolidated into dense bulk materials at 1050-1100 ^{o}C for 5 minutes under 60 MPa with a SPS 10-3 (Thermal Technology LLC). The samples ball milled for 2, 6, 18 and 54 h are denoted as BM2h, BM6h, BM18h, and BM54h, respectively.

5.2.2 Phase identification and microstructure characterization

The phase purity and crystal structure of the samples were studied by powder X-ray diffraction (PXRD) with a Phillip X'pert diffractometer with Cu K_{α} radiation (λ = 1.54184 Å). The morphology and chemical compositions of the samples were analysed

with a Quanta 650 environmental scanning electron microscope (SEM) with an energy-dispersive X-ray (EDX) spectrometer.

5.2.3 Thermoelectric transport properties

The electrical resistivity and Seebeck coefficient of samples were measured in the temperature range of 10–823 K and 80–823 K, respectively, with home-built setups that have been independently calibrated.[11] The thermal diffusivity, α, was measured on disc-shaped samples with dimensions of 6 × 6 × 1 mm by using the laser flash diffusivity method in a Netzsch LFA 457 instrument. The specific heat, C_p, was obtained with a Netzsch 404 differential scanning calorimeter (DSC) with a sapphire standard. The density, ρ, was measured by Archimedes' method. The total thermal conductivity in the range of 320 K to 850 K was calculated as $\kappa = \alpha C_p \rho$. The thermal conductivity below 300 K was measured by a steady-state method on rectangular specimens (0.5 × 0.5 × 3 mm). All three transport properties were measured along the direction parallel to the SPS pressing direction. The room temperature Hall coefficient measurements were performed with a Physical Properties Measurement System (PPMS, Quantum Design) with the magnetic field sweeping between ±2 T. Because of the high carrier concentration of the degenerately doped HMS samples, the carrier concentration p and Hall mobility were calculated as $p = -(1/eR_H)$ and $\mu_H = \sigma R_H$, respectively, without accounting for the minority carriers.

5.3 Microstructures and TE properties of cold-pressed HMS

5.3.1 Phase and microstructures of cold-pressed HMS

Figure 5.2 shows the XRD patterns of the HMS after solid-state reaction, the HMS cold-pressed under a high pressure (HP) of 3 GPa, and the HMS pressed under a

relatively low pressure (LP) of 300 MPa. All the samples were essentially single phase. A small amount of Si is noticeable in some samples. The HP HMS samples exhibit broader peaks due to either residual strain or fine grain size as a result of cold pressing. Cheng *et al.*[113] have demonstrated that the high-pressure cold-pressing method with the setup shown in Figure 5.1 can significantly reduce the grain size of the perovskite $CaIrO_3$. In this study, the high-pressure cold-pressing method also produced the HMS sample with significantly reduced grain size, which may contribute to the reduction of thermal conductivity.

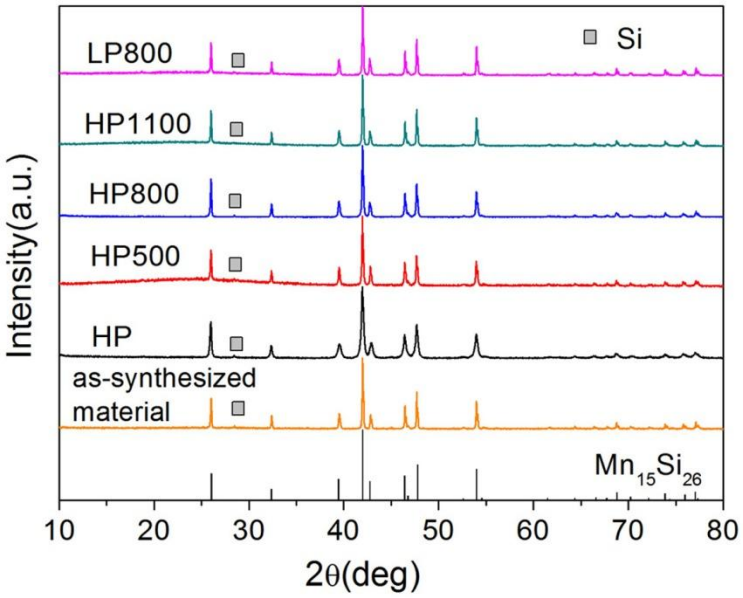

Figure 5.2: XRD patterns of as-synthesized HMS powders, the HP HMS samples sintered at different temperatures, and the LP HMS sample. The number following HP or LP in the legend is the post-press annealing temperature.

Table 5.1 summarizes the processing methods together with the measured average grain sizes and densities of all HMS samples used in this study. The average grain size was obtained by analyzing XRD patterns with the Scherrer equation.[113] With a 6%

uncertainty, the density was determined from the measured weight and volume of the sample. The average grain size was reduced from 1.5 μm to 120 nm by the HP cold-pressing process. The sample annealed at a higher temperature shows a larger grain size and higher density because of thermally activated grain growth and densification.[120,144] For the LP HMS sample, the grain size did not change after pressing, and it showed a much lower density than the HP HMS samples.

Table 5.1: Processing methods, measured average grain sizes, and measured densities of the HMS samples used in this study. The percentage given for density is the ratio of the measured density of the samples and the density for the single crystal.

Sample name	Pressure (MPa)	Annealing temperature (^{o}C)	Annealing time (h)	Average grain size (nm)	Density (g/cm^{-3})
As-synthesized materials	/	/	/	1548	/
HP	3000	/	/	120	3.84 (75%)
HP500	3000	500	6	300	3.99 (78%)
HP800	3000	800	6	450	4.06 (80%)
HP1100	3000	1100	6	3305	4.21 (83%)
LP800	300	800	6	1548	3.35 (66%)

SEM observation (Figure 5.3) yielded results consistent with the XRD analysis. After HP cold-pressing, the average grain size is several hundred nanometers (Figure 5.3a). As shown in Figure 5.3b, some small particles with a tetragonal shape were found among the large particles. The grain size in the sample after annealing at 500 ^{o}C for 6 h did not change noticeably (Figure 5.3c). The cold-pressed sample annealed at 800 ^{o}C for 6 h experienced grain growth and the texture of the grain boundaries changed remarkably, as shown in Figure 5.3d. After the annealing temperature was increased to 1100 ^{o}C, the grain size reached about 3.3 μm in the HP1100 sample which was prepared

with HP cold pressing followed by annealing at 1100 ^{o}C (Figure 5.3e). Figure 5.3f shows the SEM image of a sample prepared by LP cold pressing and annealed at 800 ^{o}C for 6 h. The grain size of the LP800 sample prepared by LP cold-pressing and subsequent annealing at 800 ^{o}C was several μm. More cavities were found in this sample than the samples prepared by HP cold pressing.

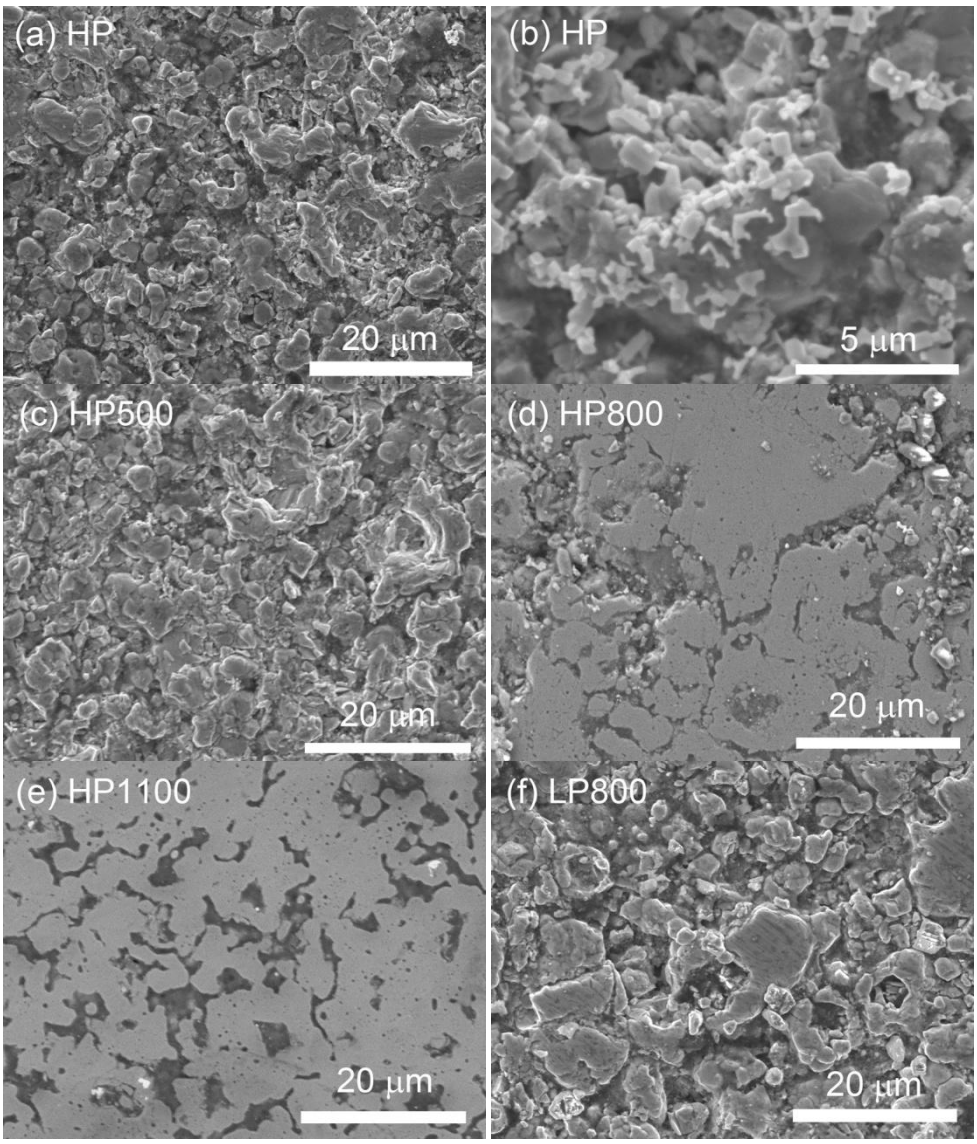

Figure 5.3: SEM images of various cold-pressed HMS samples.

5.3.2 TE properties of cold-pressed HMS

Figure 5.4 shows the measured thermoelectric properties of the cold-pressed HMS samples, in comparison with data reported for single-crystal HMS samples by Fedorov *et al.*[59] Figure 5.4a displays the temperature dependence of the electrical conductivity. The HP sample without annealing shows a very low electrical conductivity because of the small grain size and poor grain boundary connection. A peak at about 50 K was found for the HP sample. The electrical conductivity decreases dramatically when the temperature is lower than 50 K, which may be due to Anderson localization.[145] The electrical conductivity is improved by increasing the annealing temperature because of the reduction of the grain boundary density and the improvement of grain connectivity. The electrical conductivities of the HP800 and HP1100 samples, prepared by HP cold-pressing followed by annealing at 800 ^{o}C and 1100 ^{o}C, respectively, are between the single-crystal values along the [100] and [001] directions. The highest electrical conductivity is about 316 $\Omega^{-1}cm^{-1}$ at 300 K for the HP1100 sample. It is slightly lower than that of the polycrystalline HMS (400-500 $\Omega^{-1}cm^{-1}$ at 300 K with density >95%) reported by other groups.[78,146,147] The electrical conductivity of the LP800 sample, prepared by LP cold-pressing and subsequent annealing at 800 ^{o}C with a density of 66%, is much lower than that of the HP800 sample with a density of 80%. Although the HP800 sample has a much smaller grain size than the LP800 sample, the porosity of the sample appears to be another important factor influencing electrical conductivity.

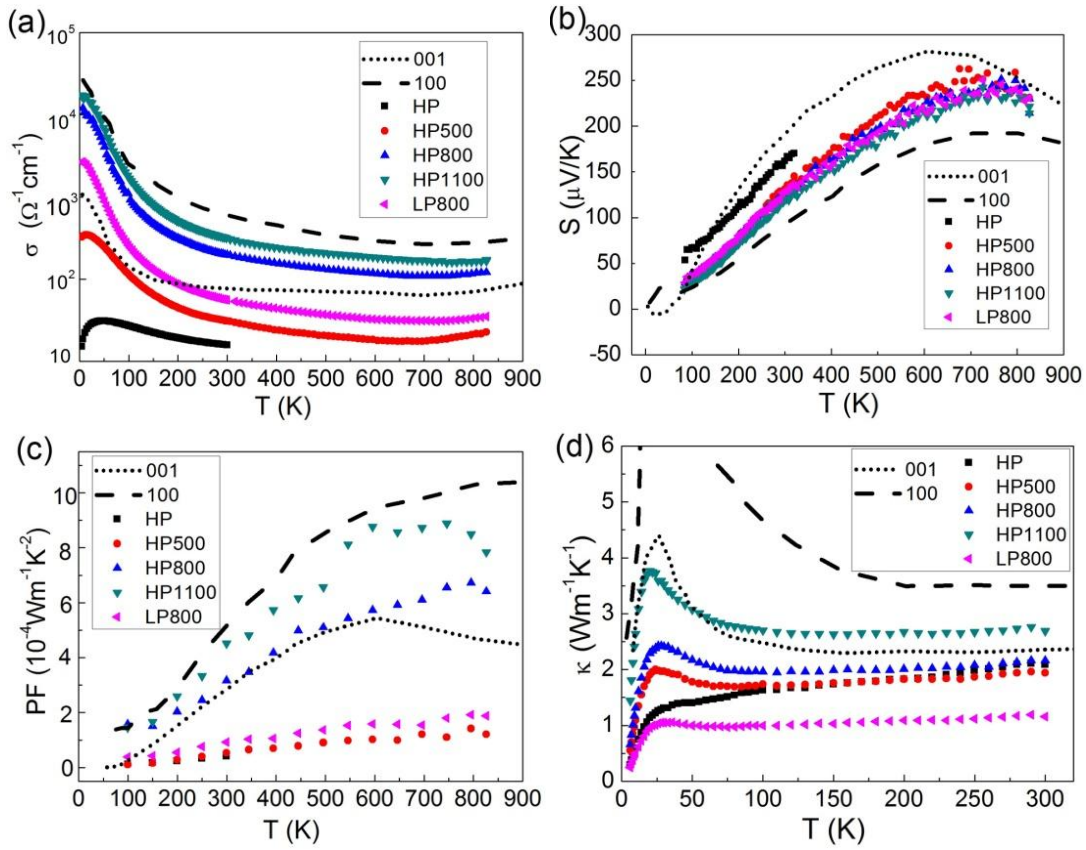

Figure 5.4: Temperature dependence of transport properties for the cold-pressed HMS samples: (a) electrical conductivity with 5% uncertainty, (b) Seebeck coefficient with 5% uncertainty, (c) power factor, and (d) thermal conductivity with 10% uncertainly. The dashed line and dotted line represent results reported for single-crystal HMS in the literature along [100] and [001], respectively.[59]

As shown in Figure 5.4b the positive Seebeck coefficient data confirm that all the samples are *p* type. All *S(T)* curves are between the two data sets reported for the single crystal along different crystal axes. The Seebeck coefficient decreases in the samples after the subsequent annealing treatment that releases the residual stress. It remains to be verified whether the slightly higher *S(T)* of the cold-pressed sample at $T < 300$ K compared to that of most polycrystalline samples was due to the effect of stress or a change in the carrier concentration. The maximum Seebeck coefficient of the HP500

sample is about 255 μV/K at 750 K, which is still higher than most results in the literature for polycrystalline HMS.[82,86] This may be attributed to the slightly excess of silicon in the starting materials. Despite their different porosities, the HP800 and LP800 samples have a nearly identical *S(T)*. Among the samples reported in Figure 5.4c, the HP1100 sample has the highest power factor, which is closest to that of the single crystal along [100].

Figure 5.4d presents the temperature dependence of thermal conductivity κ. The HP HMS sample without annealing shows a lower thermal conductivity than that of the single crystal due to enhanced grain boundary scattering and poor grain boundary connection in the cold-pressed sample. The as-measured thermal conductivities of Sample HP and HP500, prepared with HP cold pressing without annealing and with subsequent annealing at 500 ^{o}C, respectively, are about 2 W m^{-1} K^{-1} at room temperature, and are even lower than the single-crystal value along the [001] direction. The thermal conductivity increases with increasing annealing temperature. In the annealed HP samples, the thermal conductivity peaks at about 30 K. In addition, the LP sample prepared with a regular die shows the lowest κ among all the samples, which is about 1.2 W m^{-1} K^{-1} at 300 K.

Table 5.2: The room-temperature *ZT* values of all the samples in this study in comparison with literature values for single-crystal HMS in the along [100] and [001], respectively.[59]

Sample	HP	HP500	HP800	HP1100	LP800	[100]	[001]
ZT	0.006	0.008	0.044	0.051	0.024	0.044	0.036

The *ZT* values of all the samples at room temperature are listed in Table 5.2. The HP1100 sample shows a highest *ZT* at 300 K, which is mainly due to its highest electrical conductivity among all the samples investigated. The HP800 and HP1100 show a higher *ZT* than the undoped single crystal, because of a largely reduced thermal conductivity or a higher power factor. Further measurements of thermal conductivity of the samples at high temperature are in progress to obtain the *ZT* values at high temperatures.

We used the Wiedemann-Franz law to obtain the electronic thermal conductivity as $\kappa_E = L\sigma T$, with the Lorenz number taken to be 2.45×10^{-8} V^2 K^{-2} for the degenerate limit. Shown in Figure 5.6a, the lattice thermal conductivity was obtained as $\kappa_L=\kappa-\kappa_E$, The calculated κ_E contribution was found to be smaller than 10% of the total κ. Except for the HP sample without annealing, the low-temperature peak in the $\kappa_L(T)$ curve represents a typical acoustic phonon contribution in a crystal. The gradual κ_L increase with *T* at temperatures above that for the κ_L peak is a unique feature of some complex crystals. The HP sample without annealing shows a different $\kappa_L(T)$ behavior, which does not show an apparent peak at low temperatures. This behavior indicates a large suppression of the acoustic phonon contribution in this sample. Among the annealed HP samples, the HP500 and HP800 show nearly the same κ_L over the entire measured temperature range because of the similar grain sizes of 300 nm and 450 nm. The HP1100 sample with a much larger grain size (3305 nm) and likely better grain boundary connection shows a higher κ_L.

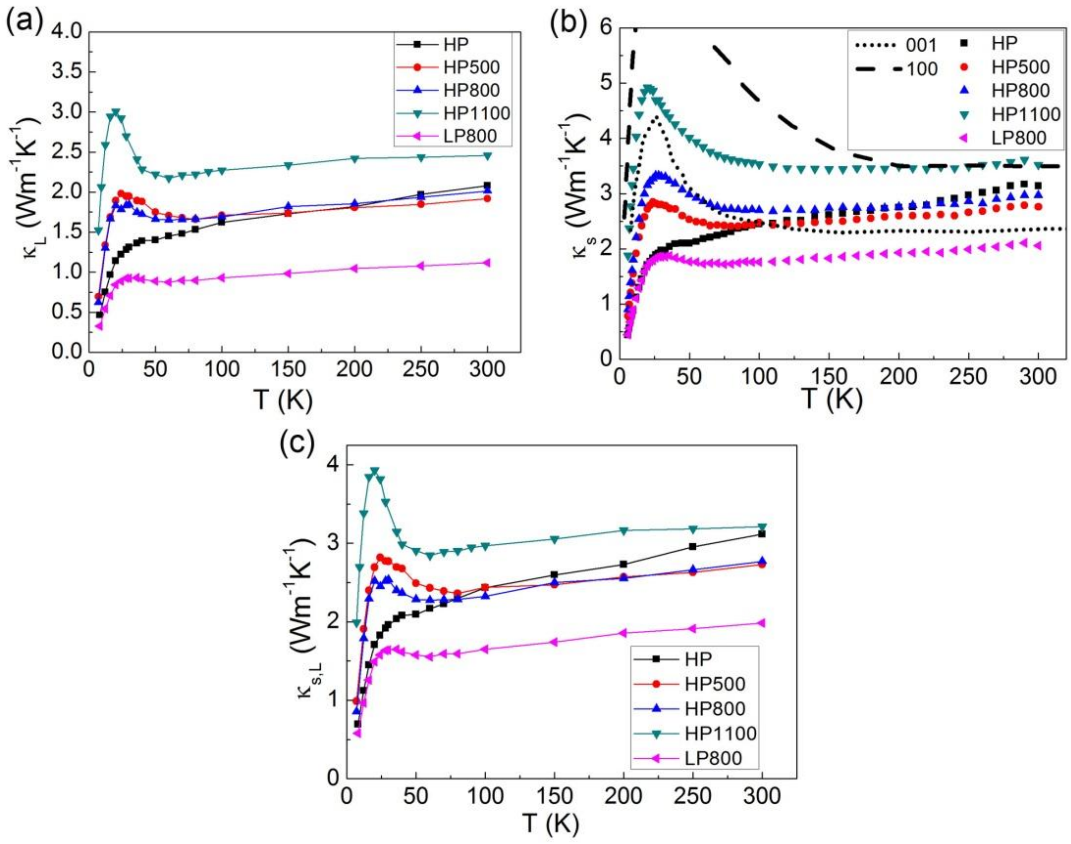

Figure 5.5: (a) The lattice thermal conductivities, (b) the solid thermal conductivities and (c) the solid lattice thermal conductivities of the cold-pressed HMS samples.

The as-measured thermal conductivity data have not been corrected for density differences due to porosity. From the known density of the sample we account for the effect of porosity by considering the sample to be a composite material composed of pure polycrystalline HMS interspersed with spherical vacuum voids of vanishing thermal conductivity. In this case, the solid thermal conductivity of bulk HMS is given by the effective medium approach (EMA)[148]

$$\kappa_s = \kappa\left[\frac{2-2f}{2+2f}\right]^{-1} \tag{5.1}$$

where f is fraction of the porosity, κ is the measured conductivity of the porous medium, and κ_s is the calculated solid thermal conductivity of polycrystalline HMS with $f = 0$. The solid thermal conductivity (κ_s) and the solid lattice thermal conductivity ($\kappa_{s,L}$) are corrected for porosity and shown in Figure 5.5b and 5.5c.

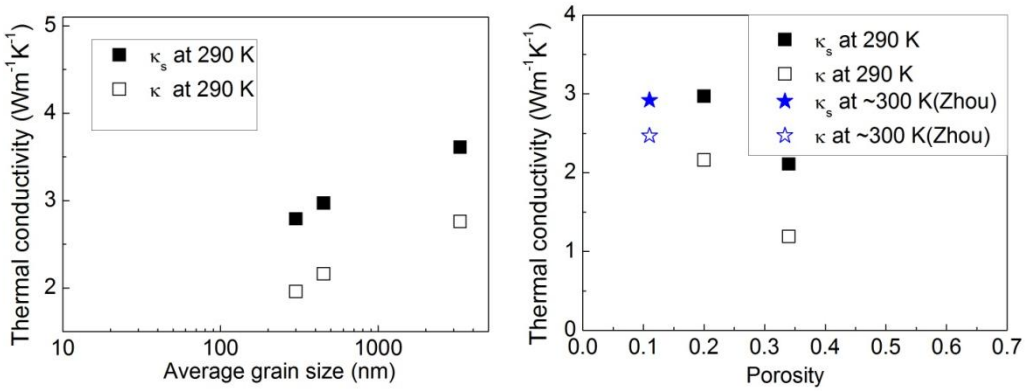

Figure 5.6: (a) Grain size dependence of the measured and solid thermal conductivity for the samples HP500, HP800, and HP1100 at 290 K; (b) porosity dependence of the measured and solid thermal conductivity for the samples HP800 and LP800 at 290 K. Shown for comparison is the thermal conductivity of hot-pressed polycrystalline HMS reported by Zhou *et al.*[88] with a porosity of ~0.11.

It is known that both increasing porosity and phonon scattering at grain boundaries can reduce the effective thermal conductivity.[28,120,149] Figure 5.6a shows the grain size dependence of the measured effective thermal conductivity and the solid thermal conductivity for HP HMS samples with nearly the same porosity (~20%). It can be seen that κ can be significantly reduced when the grain size reaches several hundred nanometers due to enhanced grain boundary scattering. Figure 5.6b shows the porosity dependence of the measured thermal conductivity and the solid thermal conductivity for the HP800 and LP 800 samples. The κ value of the LP800 sample with a porosity of 34%

is reduced by 50% compared to the HP800 sample with a porosity of 20%. Although the HP800 sample shows a smaller grain size than the LP800 sample, the porosity effect is much stronger than the grain-size effect. The solid thermal conductivity of the hot-pressed sample reported by Zhou *et al.*[88] is almost the same as that of our HP800 sample, indicating that similar grain-boundary scattering can be achieved by the two methods.

5.3.3 Thermal conductivity analysis

The solid lattice thermal conductivities were used in collaboration with Annie Weathers to calculate the mean free path (MFP) of acoustic phonons as well as the phonon transmission coefficient and Kapitza resistance across the grain boundary.[76] The Debye temperature for the acoustic branches is found to be about 660 K according to the sound velocity measurement. For $T < \theta_D/5$, we expect that the acoustic branches dominate the thermal conductivity. For this low temperature limit, the average acoustic phonon mean free path can be extracted with the Debye approximation of the acoustic branches according to

$$l = \kappa_{s,L}\left[\left(\frac{k_B{}^4 T^3}{2\pi^2 v^2 \hbar^3}\right)\int_0^{\theta_D/T}\frac{x^4 e^x dx}{\left(e^x-1\right)^2}\right]^{-1} \tag{5.2}$$

The obtained mean free path is plotted in Figure 5.7 up to a temperature of 30 K, together with the average mean free path of single-crystal HMS determined from Zaitsev *et al.*[59] In addition, the Wien's displacement law for acoustic phonons is used to calculate the dominant phonon wavelength as $\lambda_{\max} = (0.201)hv/k_B T$, the inverse of which is shown on the top axis of Figure 5.7. It is found that that the mean free path of the polycrystalline sample is up to five times lower than for single-crystal HMS. The effect of grain size on the mean free path is shown in the inset of Figure 5.7. As expected, the mean free path increases with the grain size for the HP HMS samples. However, the LP800 sample,

prepared by LP pressing and 800 ^{o}C annealing, shows a markedly low mean free path despite the large grain size.

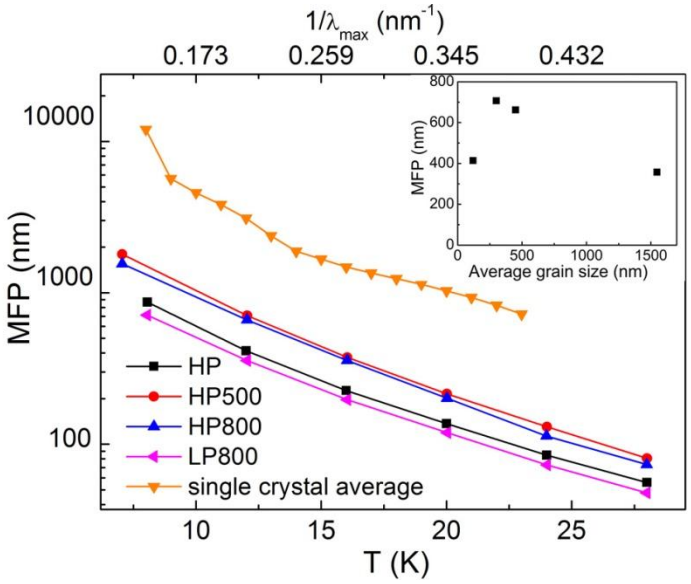

Figure 5.7: The phonon mean free path of the cold-pressed HMS samples at temperatures below 30 K. The inset shows the grain size dependence of the mean free path at 12 K.

To further investigate the effect of scattering at the grain boundaries, the transmission coefficient, *t*, across the grain interface was calculated following Wang *et al.*[120]

$$l_{bdy}^{-1} = d^{-1}\left[\left(\frac{3/2t}{1-t}\right)^{-1} + \left(\frac{1+p}{1-p}\right)^{-1}\right] \tag{5.3}$$

where *d* is the average grain size determined from the XRD pattern, l_{bdy} is the mean free path due to boundary scattering, and *p* is the specularity at the interface, taken as 0 and 1 as upper and lower bounds on *t*. We assume that boundary scattering is dominant in this regime, and thus $l^{-1} \approx l_{bdy}^{-1}$. The obtained transmission coefficient is plotted in Figure 5.8 for four prepared samples. The LP800 sample shows the lowest transmission

coefficient across the grain boundaries, consistent with the low κ and MFP, suggesting poor quality grain boundaries plays an important role in reducing the thermal conductivity.

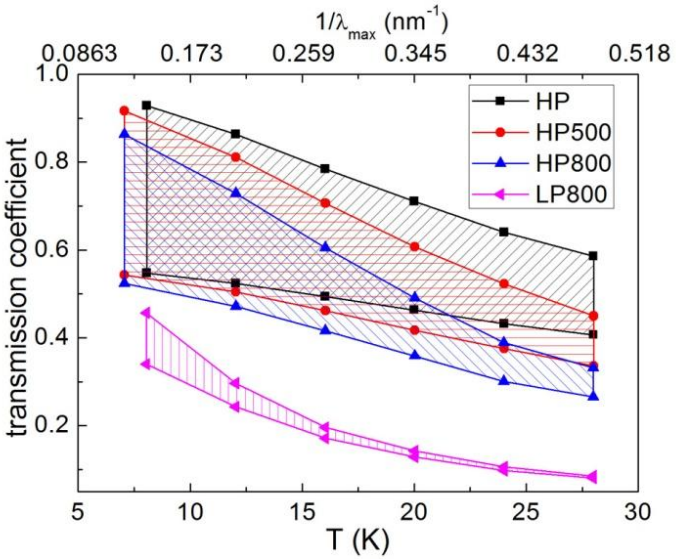

Figure 5.8: The transmission coefficient of the cold-pressed HMS samples at temperatures below 30 K for the specularity parameter range between $p = 1$ and $p = 0$.

The mean free path and phonon transmission coefficient may also be explained by considering the Kapitza resistance of the grain interface. We calculate the Kapitza resistance from[150]

$$R_K = \frac{d}{2}\left(\frac{1}{\kappa_{s,L}} - \frac{1}{\kappa_{xtal}}\right) \tag{5.4}$$

where κ_{xtal} is the average of the reported thermal conductivity of a single crystal along the two crystal directions. The result is plotted along with the characteristic length, $L_K = \kappa_{xtal} R_K$, in Figure 5.9. It is clear that in the limit of $d << L_K$, κ/κ_{xtal} is a minimum. Thus the low κ and MFP of the LP sample, particularly at temperatures above 100 K, can be explained by a greater Kapitza length relative to the grain size and therefore a greater

interface resistance at the boundary. We can expect a reduction in κ to be achieved by decreasing the grain size further, with the assumption that the Kapitza length will remain comparable at even smaller grain sizes.

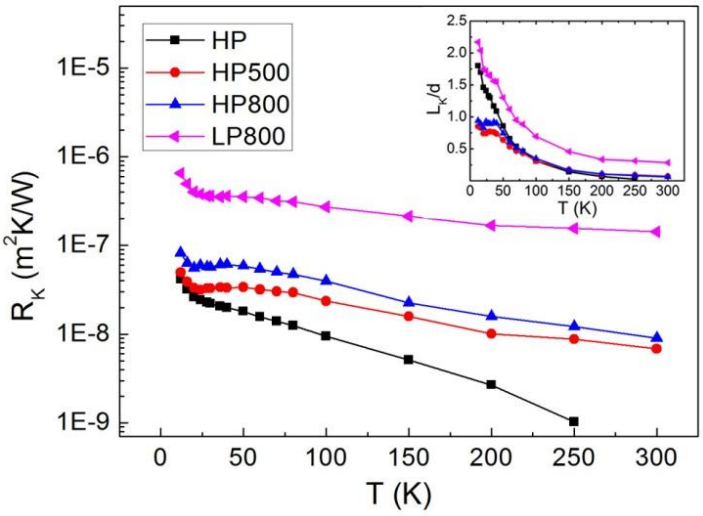

Figure 5.9: The Kapitza resistance and length of the cold-pressed HMS.

5.4 MICROSTRUCTURES AND TE PROPERTIES OF BALL MILLED HMS

Inspired by the results of the cold-pressed HMS samples, another group of nanostructured HMS samples was prepared by ball milling and SPS since the cold-pressed samples are too small for the high-temperature thermal conductivity measurement. The effects of ball milling time on the microstructures and thermoelectric transport properties of HMS are discussed in the following sections.

5.4.1 Phase and microstructures of ball milled HMS

The powder XRD patterns of products after melting, BM, and SPS are shown in Figure 5.10. It can be seen that HMS was formed after melting without detectable

secondary phases. After ball milling for 18 h, the XRD peaks become significantly broader without the presence of other impurity peaks. However, remarkable MnSi peaks were observed in the sample ball-milled for 54 h. Zhou *et al.*[151] reported that HMS decomposed into MnSi in the BM process. They proposed that chimney-ladder structures would undergo severe deformation and rearrange themselves into more stable MnSi with B20 structure according to HMS $\rightarrow$ MnSi + Si. Additional Si could be oxidized into amorphous SiO_2, although Si or SiO_2 peaks are not seen in the XRD spectra. A small peak from WC phase was found in the powders ball-milled for 54 h due to the abrasion of the milling tools. After SPS, a peak of WSi_2 was observed in the BM54h sample.

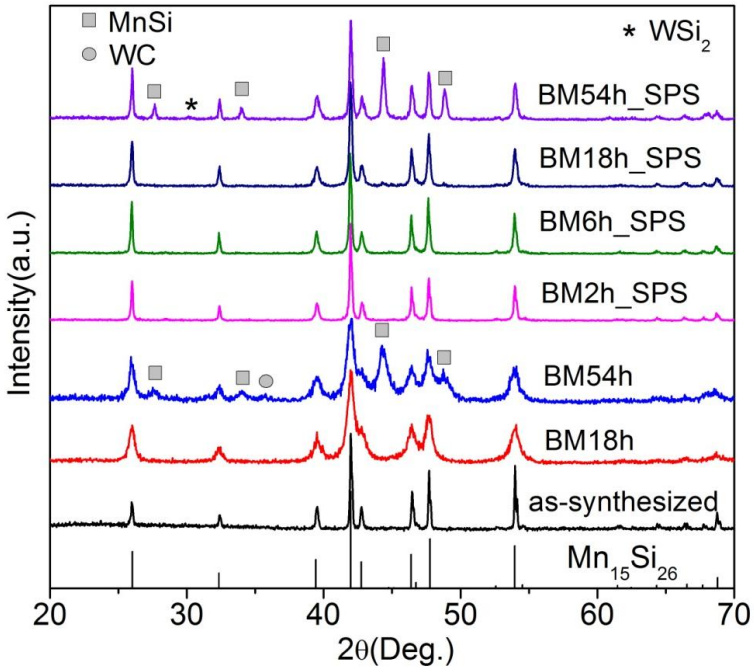

Figure 5.10: XRD patterns of various HMS samples after melting, ball-milling and SPS, respectively.

The average grain size after BM was obtained by analyzing the XRD pattern with the Scherrer equation.[113] The grain sizes are 33±9 and 50±23 nm for the sample ball-milled for 18 h and 54 h, respectively. This observation indicates that increasing the BM time does not further refine the grain size significantly, but it leads to the decomposition of HMS. As expected, the MnSi phase was only found in the BM54 h sample. The grain sizes after SPS are increased to 90±20 and 143±83 nm for the samples ball-milled for 18 h and 54 h, respectively.

Table 5.3: SPS temperature, density, crystallite size and room-temperature electrical and thermal transport properties of nanostructured bulk HMS samples after SPS.

Samples	BM time (h)	SPS temperature (^oC)	Density (g/cm^3)	Grain size (nm)	σ (Ω^{-1} cm^{-1})	R_H (10^{-9} m^3 C^{-1})	p_H (10^{21} cm^{-3})	μ_H (cm^2 V^{-1} s^{-1})
BM2h	2	1050	4.80	500	423	5.01	1.25	2.12
BM6h	6	1050	4.86	320	356	5.38	1.16	1.92
BM18h	18	1050	4.99	90	324	4.70	1.33	1.52
BM54h	54	1100	4.41	130	325	2.00	3.19	0.64

Figure 5.11 shows the SEM images of the fracture surface of the samples after SPS with different BM times. The grain size is reduced with the increase of BM time. The average grain size (L_d) is estimated from the SEM images to be about 500, 320, 90, and 130 nm for the bulk sample obtained by applying SPS to precursor powders ball milled for 2, 6, 18, and 54 h, respectively. The slightly larger grain size of the BM54h sample can be attributed to the higher SPS temperature, as shown in Table 5.3. It should be noted that some grains shown in SEM may be agglomerates of smaller crystallites. Nevertheless, the SEM results for the BM18h and BM54h samples are consistent with the calculated crystallite size based on the XRD results. Figure 5.12a shows a secondary phase of about 40 μm found in the BM54h sample. The magnified SEM image (Figure

5.12b) indicates that the secondary phase is a cluster made of many flower-like phases. Some individual secondary phases were observed as bright inclusions in the backscattered electron images (Figure 5.12c and d). The elemental mapping analysis further indicates that the bright inclusion consists of a carbon-rich core and a tungsten, silicon-rich shell. The formation of the secondary phase is attributed to the contamination of WC introduced from the WC jar/balls.

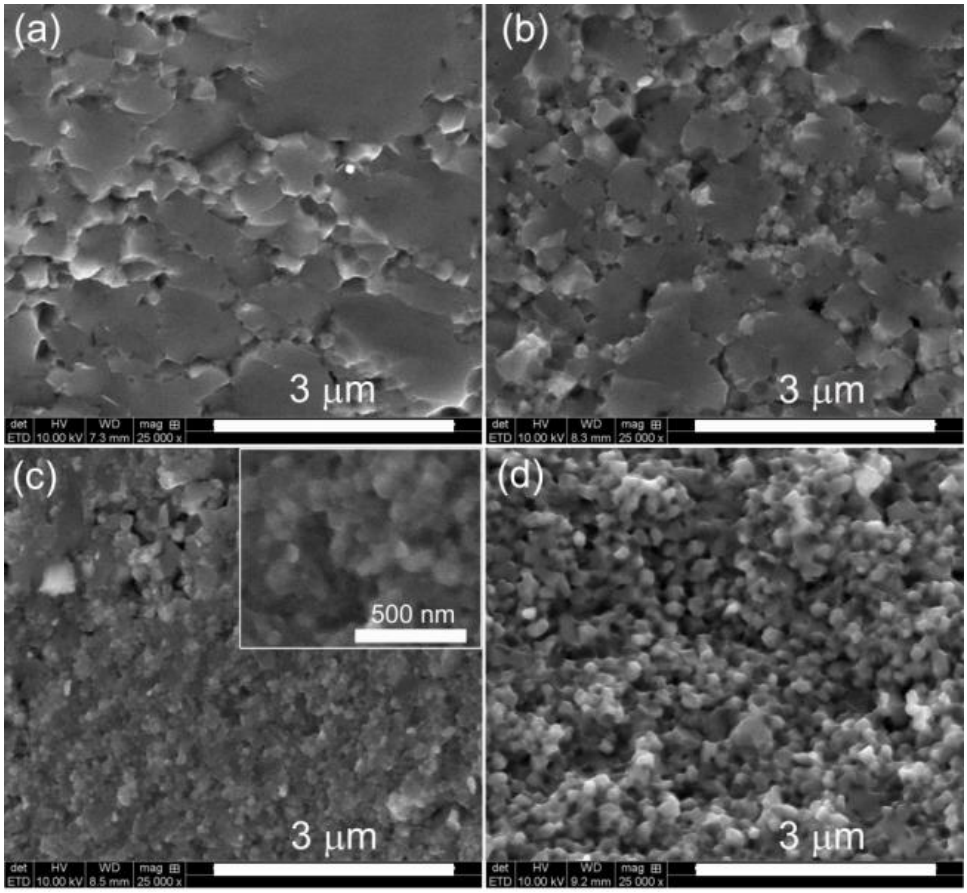

Figure 5.11: SEM images of the fracture surface of various bulk HMS samples obtained by applying SPS to powder ball-milled for (a) 2 h, (b) 6 h, (c) 18 h and (d) 54 h.

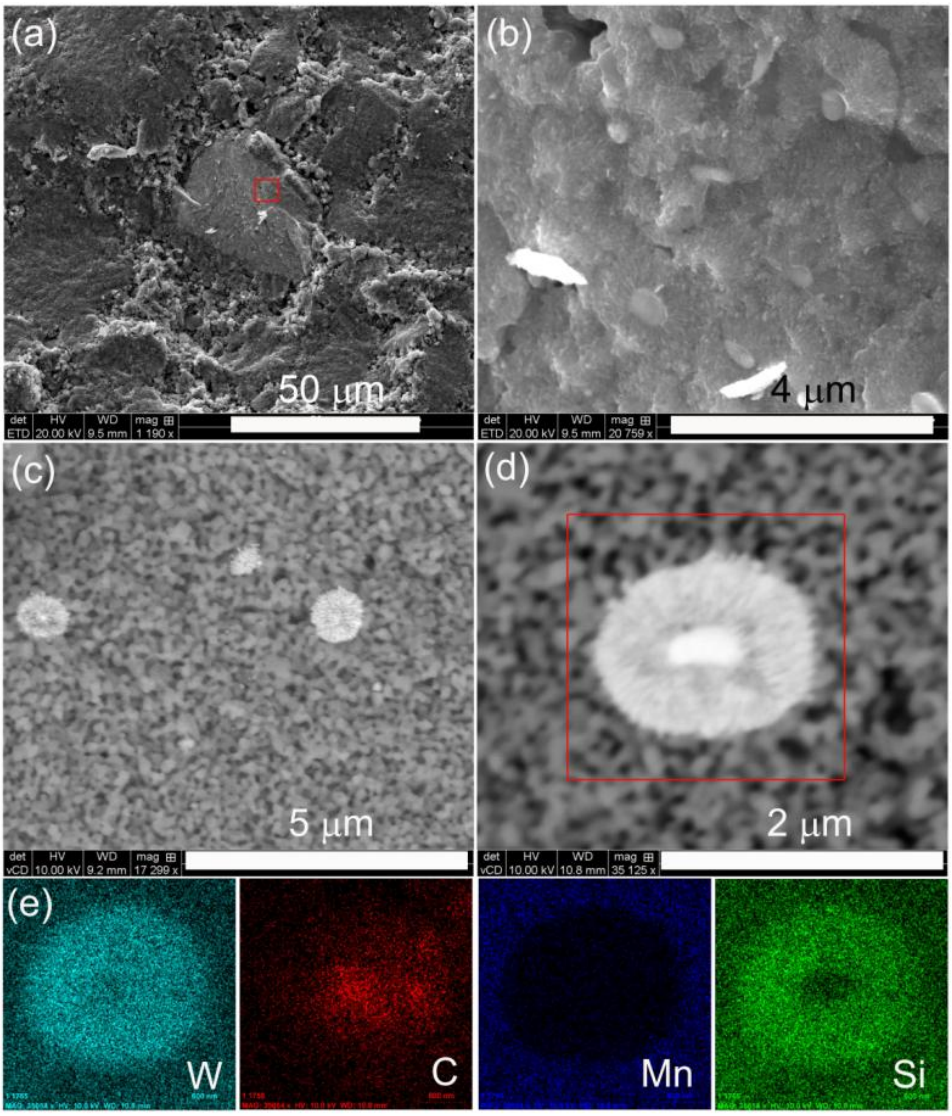

Figure 5.12: (a) SEM image of the fracture surface of the BM54h sample with different magnifications. (b) The magnification of the area marked by the red square in (a). (c), (d) backscattered electron images of the fracture surface of the BM54h sample. (e) Elemental maps of the secondary phase in (d).

5.4.2 Electronic transport properties of ball milled HMS

The temperature dependence of Hall carrier density (p_H) and mobility (μ_H) for the HMS samples are plotted in Figure 5.13. For the three samples ball milled for 2 h, 6 h, and 18 h, the room-temperature p_H is similar and about 1.3×10^{-21} cm^{-3}. Furthermore, the

p_H values are almost constant with temperature, which is typical for degenerate semiconductors. In addition, the μ_H decreases with decreasing grain size for these three samples. In comparison, the BM54h sample shows the highest p_H and lowest μ_H at room temperature as shown in Table 5.3, which could be attributed to the formation of MnSi and W/C-rich phases. The lower μ_H and higher p_H were also reported in the HMS samples with large amount of MnSi prepared by mechanical alloying and SPS.[79]

The temperature dependence of μ_H can be used to determine the dominant carrier scattering mechanism. As shown in Figure 5.13b, the mobility varies approximately as $T^{-3/2}$ for all samples above 100 K, which indicates that acoustic phonon scattering is the dominant scattering mechanism. For the BM18h sample, the mobility shows a relationship of $\mu_H \propto T^{-1/2}$ below 100 K, which reveals the effect of increased grain boundary scattering.

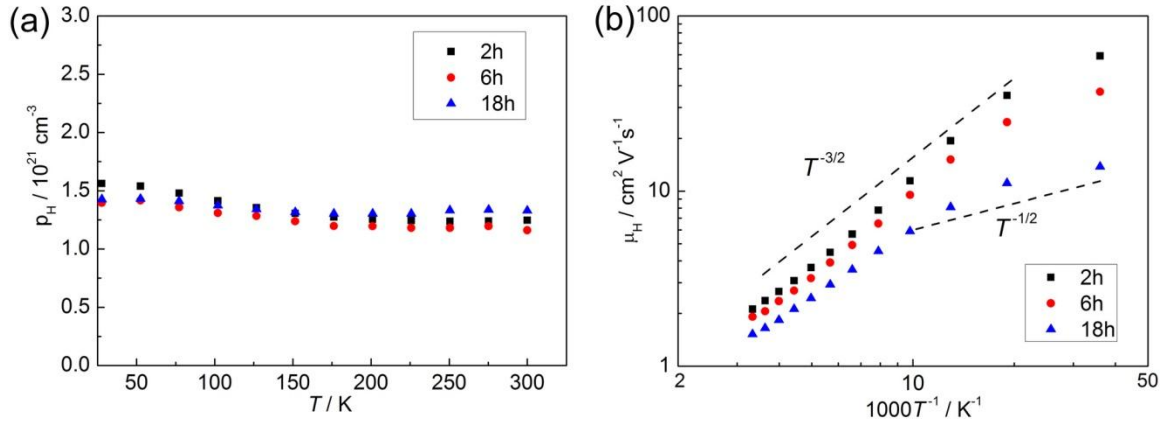

Figure 5.13: (a) Hall carrier density and (b) mobility of the bulk HMS samples with different ball-milling time. The uncertainty of carrier concentration and mobility are 6% and 8%, respectively.

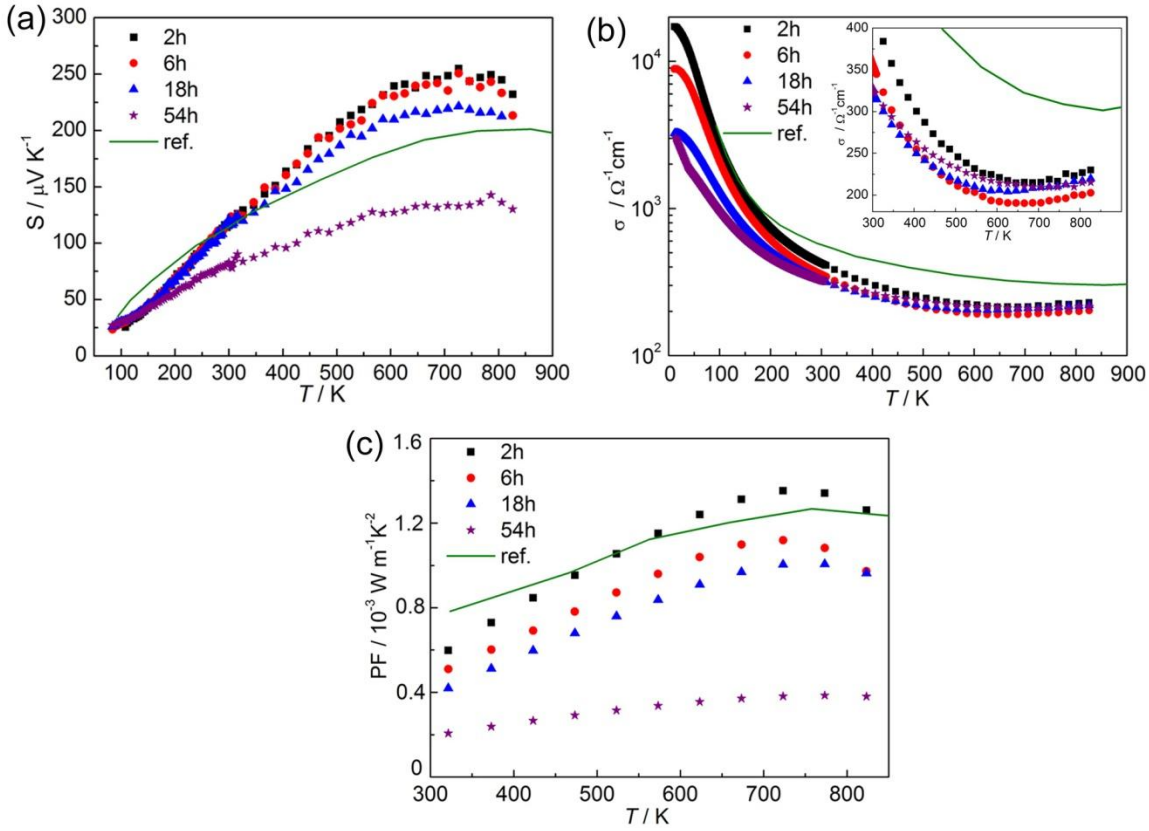

Figure 5.14: Temperature dependence of transport properties of various HMS samples with different ball milling time: (a) Seebeck coefficient with 5% uncertainty, (b) electrical conductivity with 5% uncertainty, and (c) power factor with 11% uncertainty. The inset of (b) is the electrical conductivity above 300 K. Showing for comparison are the data reported by Ponnambalam *et al.*[124]

The temperature-dependent thermoelectric transport properties of four samples are depicted in Figure 5.14 together with the data of hot-pressed HMS without ball milling reported by Ponnambalam *et al.*[124] The Seebeck coefficient (*S*) increases linearly up to 600 K then peaks at ~750 K. Most of our samples show higher *S* above 300 K than the hot-pressed HMS because our samples have lower p_H (~1.3 × 10^{-21} cm^{-3}) than the hot-pressed sample (2.1 × 10^{-21} cm^{-3}) at 300 K.[124] The *S* of the BM54h sample was reduced significantly as compared to other samples, which is mainly caused by the formation of metallic MnSi.[66,152-155] The σ below 300 K decreases monotonically with increasing BM

time owing to enhanced grain-boundary scattering. However, the BM18h and BM54h samples exhibit similar σ values as the BM2h sample above 700 K, which could be related to the formation of the secondary MnSi phase. As a consequence, the power factor (*PF*) is reduced by BM. The peak *PF* is decreased from 1.3 × 10^{-3} W m^{-1} K^{-2} for the BM2h sample to 0.4×10^{-3} W m^{-1} K^{-2} for the BM54h sample.

5.4.3 Thermal properties and *ZT* of ball milled HMS

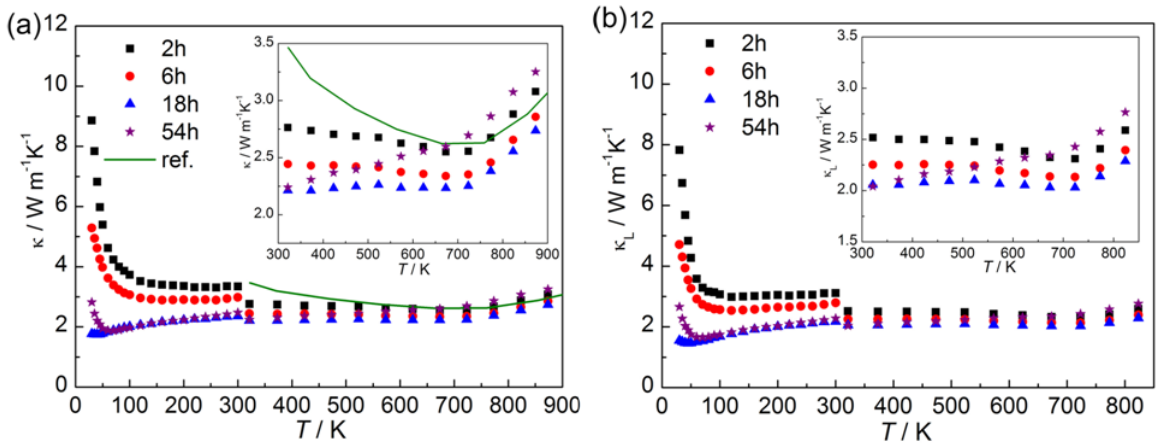

Figure 5.15: Temperature dependence of thermal properties of various HMS samples with different ball milling time: (a) total thermal conductivity, and (b) lattice thermal conductivity. The insets are the values above 300 K. The uncertainty for laser flash method and steady-state method are 7% and 15%, respectively. Showing for comparison in (a) are the data reported by Ponnambalam *et al.*[124]

The temperature dependence of total thermal conductivity (κ) and lattice thermal conductivity (κ_L) are given in Figure 5.15. The ball milled samples show lower κ than the sample without nanostructuring.[124] It is also clear that the reduction of grain size leads to lower κ values at temperatures below 700 K. The lattice thermal conductivity is calculated by subtracting the electronic contribution (κ_E) from the total thermal

conductivity. The electronic thermal conductivity is obtained by $\kappa_E = L\sigma T$, where the Lorenz number(L) is calculated as[156]

$$L = \frac{k_B^{\ 2}}{e^2}\frac{3F_0(\eta)F_2(\eta) - 4F_1(\eta)^2}{F_0(\eta)^2}. \tag{5.7}$$

The κ_L of HMS is significantly reduced by decreasing the grain size. At 323 K, the κ_L is reduced from is ~2.5 W m^{-1} K^{-1} for the BM2h sample to ~2.0 W m^{-1} K^{-1} for the BM18h sample. Due to the presence of MnSi, the BM54h sample exhibits higher κ_L values than the BM18h sample.

In order to better understand phonon transport in nanostructured HMS, we have studied the grain size dependence of the κ_L for the BM2h, BM6h and BM18h samples without noticeable secondary phases. As shown in Figure 5.16, κ_L can be remarkably suppressed when the grain size is reduced to 90 nm due to enhanced grain boundary scattering. It should be noticed that the reduction of κ_L is more significant at low temperature. The κ_L is reduced by about 75% at 40 K while this reduction is only 13% at 673 K.

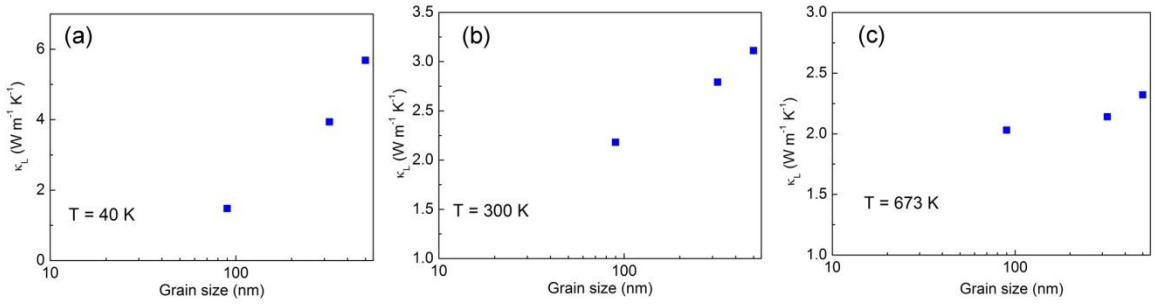

Figure 5.16: Grain size dependence of the lattice thermal conductivity for HMS samples at (a) 40 K, (b) 300 K, and (c) 673 K.

Figure 5.17 shows the *ZT* of the HMS samples. The peak *ZT* of the BM2h sample is about 0.39 near 773 K. The BM process does not improve the *ZT*. In comparison, the BM54h sample shows a peak *ZT* of only about 0.1 at 773 K. Although the κ_L is suppressed by long BM time, the σ and *S* are also reduced due to the effects of smaller grain size and formation of MnSi. Besides the adverse effects of the secondary phases, the relatively large grain size (~90 nm) also limits the *ZT* enhancement in our samples. The κ_L could be suppressed more significantly above 300 K if the grain size reaches 10 nm.[90] Thus, alternative approaches, such as the bottom-up approach,[80] should be explored to synthesize pure HMS bulk samples with much smaller grain size.

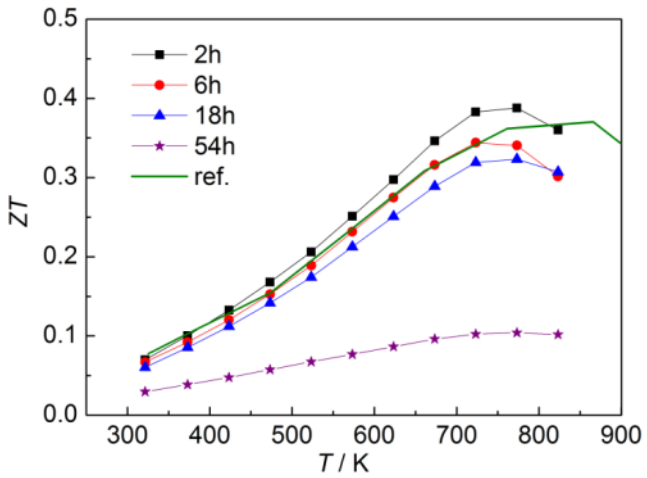

Figure 5.17: The *ZT* of various HMS samples with different ball milling time. The uncertainty of *ZT* is 13%. The data reported by Ponnambalam *et al.*[124] are shown for comparison.

5.5 SUMMARY

HMS samples with different grain sizes and porosities have been prepared by cold-pressing and annealing. Both the grain size and porosity strongly influence the thermoelectric properties of the HMS samples. Remarkable thermal conductivity

reduction in the HP HMS samples with nanoscale grain size was achieved. The mean free path of our porous samples is up to five times lower than for single-crystal HMS, indicating that the grain boundary scattering is the dominant mechanism for reduction in thermal conductivity at low temperature. We find that the phonon mean free paths are larger than the average grain size for most of the cold-pressed samples, owing to a relatively high transmission coefficient and short Kapitza length. In comparison, the phonon mean free path is considerably smaller than the grain size for the sample with a high porosity of 34% because poor grain boundary connectivity in this sample leads to low phonon transmission coefficient and increased Kapitza length. The measured *ZT* values for the HP HMS sample annealed at 1100 K is slightly higher than for the undoped single crystal HMS along the [100] direction, due to a considerably smaller thermal conductivity and comparable power factor.

Another group of nanostructured HMS samples were prepared by melting followed by ball milling and SPS. Different grain sizes in the bulk samples from ~500 nm to ~90 nm can be achieved by controlling the BM time. However, further increasing the BM time does not further reduce the grain size, but leads to the formation of MnSi and contamination of WC jars/balls, which are detrimental to TE performance of HMS. Both thermal conductivity and electrical conductivity decrease with the reduction of grain size. The lowest lattice thermal conductivity was achieved for the BM18h sample; it is about ~2.0 W m^{-1} K^{-1} at 323 K. The reduction of lattice thermal conductivity by nanostructuring is found to be more significant at low temperatures. Because of formation of the impurity phases and relatively large grain size, the *ZT* values are not improved in the ball-milled HMS samples. In order to achieve *ZT* enhancement via size effect, alternative synthesis methods, such as bottom-up approach, can be studied to prepare nanostructured HMS with a grain size of 10-20 nm.

Chapter 6: Conclusions and future work

This dissertation presents an investigation of the TE transport properties in HMS with a complex NCL structure. The work is focused to establish a better understanding of the structure-property relationships and in particularly the intriguing phonon and electron transport behaviors of this complex material. At the same time, the effects of doping and nanostructuring on microstructures and TE properties have been studied in an attempt to improve the *ZT* of HMS.

HMS crystals have been grown by the Bridgeman method for measurements of the phonon dispersion by inelastic neutron scattering as well as the thermal and thermoelectric properties. Based on a comparison between the experimental results and recent theoretical modeling inspired by the experimental results, numerous low-energy optical vibration modes are present in HMS, including unusually low-frequency twisting motions of the Si ladders inside the Mn chimneys. These optical modes show low group velocities and can provide a large phase space for scattering acoustic phonons. These features can be used to explain the low and anisotropic thermal conductivity.

Experiments and analysis have been carried out to investigate the effects of Al and (Al,Ge) doping on the microstructure and thermoelectric properties of polycrystalline HMS samples, which were prepared by solid-state reaction, ball milling, and followed by spark plasma sintering. It has been found that Al doping effectively increases the hole concentration, which leads to an increase of the electrical conductivity and power factor. By introducing the second dopant Ge into Al-doped HMS, the electrical conductivity is increased, but the Seebeck coefficient is decreased as a result of further increased hole concentration. The peak power factor is found to occur at the optimized hole concentration between 1.8×10^{21} and 2.2×10^{21} cm^{-3} at room temperature. The (Al,Ge)-

doped HMS samples show lower power factors owing to their higher hole concentrations. The mobility of (Al,Ge)-doped HMS with x=0.0035 and y=0.035 varies approximately as $T^{-3/2}$ above 200 K, suggesting that acoustic phonon scattering is the dominant mechanism. The thermal conductivity of HMS does not change appreciably by Al or (Al,Ge) doping. The maximum *ZT* of (Al,Ge)-doped HMS is 0.57 at 823 K, which is similar to that found in the optimized Al-doped HMS. The *ZT* values were reduced in the (Al,Ge)-doped with high Ge concentration (y = 0.025 and 0.035), which is caused by their lower power factor. In addition, according to a two-band model, the hole contribution to the thermal conductivity dominates the bipolar and electron contributions for all samples from 300 to 823 K, and accounts for about 12% of the total thermal conductivity at about 800 K.

The Re-substituted polycrystalline HMS samples have been prepared by solid-state reaction followed by ball milling, and consolidated by spark plasma sintering. The solubility limit of Re is determined to be about x = 0.18. Elemental inhomogeneity and the formation of $ReSi_{1.75}$ inclusions with 50–200 nm size are found within the HMS matrix. It is found that the power factor does not change markedly at low Re content of $x \leq 0.04$ before it drops considerably at higher Re contents. It has been shown that the already low thermal conductivity of HMS can be reduced further to approach the minimum thermal conductivity via partial substitution of Mn with heavier Re to increase point defect scattering. The κ_L value at x = 0.04 and T = 723 K is suppressed to be about 1.8 W m^{-1} K^{-1}, while the lowest κ_L was achieved in the sample with x = 0.12, which is about 1.6 W m^{-1} K^{-1} at 723 K. These values approach the calculated minimum κ_L value of 1.4 W m^{-1} K^{-1} for $T \geq 700$ K. Compared to pure HMS, the reduced lattice thermal conductivity in $Re_xMn_{1-x}Si_{1.8}$ results in a 25% increase of the peak figure of merit *ZT* to reach 0.57±0.08 at 800 K for x = 0.04.

Polycrystalline HMS samples with different grain sizes have been obtained by two different methods: (1) cold-pressing the HMS powder under a high pressure of about 3GPa and post annealing; (2) ball milling for different time and consolidation by SPS. For the cold-pressed samples, the effect of the grain size and porosity on the Seebeck coefficient is not as apparent as that on the electrical conductivity and thermal conductivity. The electrical conductivity of the cold-pressed samples increases as the grains grow and the grain boundary connection is improved during the post-annealing. A significant reduction in the thermal conductivity of the cold-pressed samples was observed. The sample prepared with low-pressure pressing shows the lowest thermal conductivity of 1.2 $Wm^{-1}K^{-1}$ at 300 K, which can be attributed to its high porosity of 34% and low phonon transmission coefficient through the grain boundaries. The low-temperature thermal conductivity data of all samples were analyzed to obtain the phonon transmission coefficient and the Kapitza resistance at the grain boundaries.

For the ball-milled HMS samples, both electrical conductivity and thermal conductivity decrease with reduction of grain size. It is found that the grain-size effect plays a more important role at low temperatures. By prolonging the ball milling time, MnSi and tungsten/carbon rich phases were formed due to the mechanochemical decomposition and contamination of milling tools, respectively, resulting in lower Seebeck coefficient and higher thermal conductivity above room temperature. Because of formation of the impurity phases and relatively large grain size (> 90 nm), the *ZT* values are not improved in the ball-milled HMS samples. The maximum *ZT* value for the sample with the longest ball-milling time is reduced to 0.1 at 770K, which is only about 25% of that for the sample without nanostructuring.

These experiments contribute to a better understanding of the intriguing TE phenomena in HMS of Nowotny chimney ladder phase. In particular, the experiments

have verified the predicted presence of numerous low-lying optical phonons, especially a twisting polarization in a similar frequency range with the acoustic phonon polarization. In addition, the optimum carrier concentration for HMS has been revealed by the studies. The suppression of lattice thermal conductivity has been demonstrated by isoelectronic alloying and nanostructuring. While progress has been made in this work for establishing a better structure-properties relationship of HMS, further works, especially new approaches for improving *ZT* of HMS to above unity, are still required. For future work, it is of interest to study the TE properties of nanostructured bulk HMS prepared by a bottom-up approach to address the unintentional impurities and defects found in the samples prepared by a top-down ball-milling-based approach. Further improvement in *ZT* in Re-substituted HMS may be possible via rational choice of impurity doping elements to optimize the carrier concentration of the $Re_xMn_{1-x}Si_{1.8}$ system. In addition, efforts are needed to search for resonant doping in HMS system.

References

1 DiSalvo, F. J. Thermoelectric cooling and power generation. *Science* **285**, 703-706 (1999).

2 Sales, B. C. Thermoelectric materials - Smaller is cooler. *Science* **295**, 1248-1249 (2002).

3 Seebeck, T. J. Magnetic polarization of metals and minerals. *Abhandlungen der Deutschen Akademie der Wissenschaften zu Berlin* **265** (1822-1823).

4 Peltier, J. C. Nouvellles experiences sur la caloricite des courans electrique. *Ann. Chimm.* **LV1:371** (1834).

5 Thomson, W. On a mechanical theory of thermoelectric currents. *Proceedings of the Royal Society of Edinburgh* **91** (1851).

6 Vedernikov, M. V. & Iordanishvili, E. K. A. F. Ioffe and origin of modern semiconductor thermoelectric energy conversion. *17th Int. Conf. on Thermoelectrics* **1**, 37-42 (1998).

7 de Boor, J. *et al.* Microstructural effects on thermoelectric efficiency: A case study on magnesium silicide. *Acta Mater.* **77**, 68-75 (2014).

8 Seto, J. Y. W. The electrical properties of polycrystalline silicon films. *J. Appl. Phys.* **46**, 5247-5254 (1975).

9 Xie, H. *et al.* Beneficial Contribution of Alloy Disorder to Electron and Phonon Transport in Half-Heusler Thermoelectric Materials. *Adv. Funct. Mater.* **23**, 5123-5130 (2013).

10 Tritt, T. M. Thermal conductivity: theory, properties and applications. *Kuwer Academic/Plenum Publisher, New York*, (2004).

11 Chen, X. *et al.* Effects of (Al,Ge) double doping on the thermoelectric properties of higher manganese silicides. *J. Appl. Phys.* **114** (2013).

12 Seeger, K. Semiconductor Physics: An Introduction, 9th Edition, *Springer, New York* (2004).

13 Nolas, G. S., Sharp, J. & Goldsmid, H. J. Thermoelectrics, Basic Principles and New Materials Developments. *Springer-Verlag, Berlin* (2001).

14 Migas, D. B., Shaposhnikov, V. L., Filonov, A. B., Borisenko, V. E. & Dorozhkin, N. N. Ab initio study of the band structures of different phases of higher manganese silicides. *Phys. Rev. B* **77**, 075205 (2008).

15 H. J. Goldsmid. Introduction to Thermoelectricity. *Spinger, New York* (2009).

16 Sootsman, J. R., Chung, D. Y. & Kanatzidis, M. G. New and Old Concepts in Thermoelectric Materials. *Angew. Chem.* **48**, 8616-8639 (2009).

17 Biswas, K. *et al.* High-performance bulk thermoelectrics with all-scale hierarchical architectures. *Nature* **489**, 414-418 (2012).

18 Zhao, L.-D. *et al.* Ultralow thermal conductivity and high thermoelectric figure of merit in SnSe crystals. *Nature* **508**, 373 (2014).

19 Hicks, L. D. & Dresselhaus, M. S. Effect of quantum-well structures on the thermoelectric figure of merit. *Phys. Rev. B* **47**, 12727-12731 (1993).
20 Hicks, L. D. & Dresselhaus, M. S. Effect of quantum-well structures on the thermoelectric figure of merit. *Phys. Rev. B* **47**, 16631-16634 (1993).
21 Venkatasubramanian, R., Siivola, E., Colpitts, T. & O'Quinn, B. Thin-film thermoelectric devices with high room-temperature figures of merit. *Nature* **413**, 597-602 (2001).
22 Harman, T. C., Taylor, P. J., Walsh, M. P. & LaForge, B. E. Quantum dot superlattice thermoelectric materials and devices. *Science* **297**, 2229-2232 (2002).
23 Vineis, C. J., Shakouri, A., Majumdar, A. & Kanatzidis, M. G. Nanostructured Thermoelectrics: Big Efficiency Gains from Small Features. *Adv. Mater.* **22**, 3970-3980 (2010).
24 Vineis, C. J. *et al.* Carrier concentration and temperature dependence of the electronic transport properties of epitaxial PbTe and PbTe/PbSe nanodot superlattices. *Phys. Rev. B* **77**, 235202 (2008).
25 Koh, Y. K., Vineis, C. J., Calawa, S. D., Walsh, M. P. & Cahill, D. G. Lattice thermal conductivity of nanostructured thermoelectric materials based on PbTe. *Appl. Phys. Lett.* **94** (2009).
26 Hsu, K. F. *et al.* Cubic $AgPb_mSbTe_{2+m}$: Bulk thermoelectric materials with high figure of merit. *Science* **303**, 818-821 (2004).
27 Zhao, X. B. *et al.* Bismuth telluride nanotubes and the effects on the thermoelectric properties of nanotube-containing nanocomposites. *Appl. Phys. Lett.* **86**, 062111 (2005).
28 Poudel, B. *et al.* High-thermoelectric performance of nanostructured bismuth antimony telluride bulk alloys. *Science* **320**, 634-638 (2008).
29 Joshi, G. *et al.* Enhanced Thermoelectric Figure-of-Merit in Nanostructured p-type Silicon Germanium Bulk Alloys. *Nano Lett.* **8**, 4670-4674 (2008).
30 Zebarjadi, M. *et al.* Power Factor Enhancement by Modulation Doping in Bulk Nanocomposites. *Nano Lett.* **11**, 2225-2230 (2011).
31 Yu, B. *et al.* Enhancement of Thermoelectric Properties by Modulation-Doping in Silicon Germanium Alloy Nanocomposites. *Nano Lett.* **12**, 2077-2082 (2012).
32 Pei, Y.-L., Wu, H., Wu, D., Zheng, F. & He, J. High Thermoelectric Performance Realized in a BiCuSeO System by Improving Carrier Mobility through 3D Modulation Doping. *J. Am. Chem. Soc.***136**, 13902-13908 (2014).
33 Cutler, M. & Mott, N. F. Observation of Anderson Localization in an Electron Gas. *Phys. Rev.* **181**, 1336 (1969).
34 Heremans, J. P. *et al.* Enhancement of thermoelectric efficiency in PbTe by distortion of the electronic density of states. *Science* **321**, 554-557 (2008).
35 Pei, Y. *et al.* Convergence of electronic bands for high performance bulk thermoelectrics. *Nature* **473**, 66-69 (2011).
36 Heremans, J. P., Wiendlocha, B. & Chamoire, A. M. Resonant levels in bulk thermoelectric semiconductors. *Energy Environ. Sci.* **5**, 5510-5530 (2012).

37 Jaworski, C. M., Kulbachinskii, V. & Heremans, J. P. Resonant level formed by tin in Bi2Te3 and the enhancement of room-temperature thermoelectric power. *Phys. Rev. B* **80**, 233201 (2009).
38 Zhang, Q. *et al.* High thermoelectric performance by resonant dopant indium in nanostructured SnTe. *Proc. Natl. Acad. Sci.* **110**, 13261-13266 (2013).
39 Liu, W. *et al.* Convergence of Conduction Bands as a Means of Enhancing Thermoelectric Performance of n-Type $Mg_2Si_{1-x}Sn_x$ Solid Solutions. *Phys. Rev. Lett.* **108** (2012).
40 Snyder, G. J. & Toberer, E. S. Complex thermoelectric materials. *Nature Mater.* **7**, 105-114 (2008).
41 Roufosse, M. & Klemens, P. G. Thermal Conductivity of Complex Dielectric Crystals. *Phys. Rev. B* **7**, 5379-5386 (1973).
42 Slack, G. A. in CRC Handbook of Thermoelectrics, Ed. by Rowe M., *CRC Press, Boca Ration, FL*, 407 (1995).
43 Cohn, J. L., Nolas, G. S., Fessatidis, V., Metcalf, T. H. & Slack, G. A. Glasslike heat conduction in high-mobility crystalline semiconductors. *Phys. Rev. Lett.* **82**, 779-782 (1999).
44 Christensen, M. *et al.* Avoided crossing of rattler modes in thermoelectric materials. *Nature Mater.* **7**, 811-815 (2008).
45 Brown, S. R., Kauzlarich, S. M., Gascoin, F. & Snyder, G. J. $Yb_{14}MnSb_{11}$: New high efficiency thermoelectric material for power generation. *Chem. Mater.* **18**, 1873-1877 (2006).
46 Toberer, E. S. *et al.* Traversing the Metal-Insulator Transition in a Zintl Phase: Rational Enhancement of Thermoelectric Efficiency in $Yb_{14}Mn_{1-x}Al_xSb_{11}$. *Adv. Funct. Mater.* **18**, 2795-2800 (2008).
47 Caillat, T., Fleurial, J. P. & Borshchevsky, A. Preparation and thermoelectric properties of semiconducting Zn_4Sb_3. *J. Phys. Chem. Solids* **58**, 1119-1125 (1997).
48 Toberer, E. S., Rauwel, P., Gariel, S., Tafto, J. & Snyder, G. J. Composition and the thermoelectric performance of β-Zn_4Sb_3. *J. Mater. Chem.* **20**, 9877-9885 (2010).
49 Snyder, G. J., Christensen, M., Nishibori, E., Caillat, T. & Iversen, B. B. Disordered zinc in Zn_4Sb_3 with phonon-glass and electron-crystal thermoelectric properties. *Nature Mater.* **3**, 458-463 (2004).
50 Kim, H. J., Božin, E. S., Haile, S. M., Snyder, G. J. & Billinge, S. J. L. Nanoscale alpha-structural domains in the phonon-glass thermoelectric material beta-Zn_4Sb_3. *Phys. Rev. B* **75**, 134103 (2007).
51 Liu, H. *et al.* Copper ion liquid-like thermoelectrics. *Nature Mater.* **11**, 422-425 (2012).
52 Liu, H. *et al.* Ultrahigh Thermoelectric Performance by Electron and Phonon Critical Scattering in $Cu_2Se_{1-x}I_x$. *Adv. Mater.* **25**, 6607-6612 (2013).

53 Kawasumi, I., Sakata, M., Nishida, I. & Masumoto, K. Crystal growth of manganese silicide, $MnSi_{\sim 1.73}$ and semiconducting properties of $Mn_{15}Si_{26}$. *J. Mater. Sci.* **16**, 355-366 (1981).
54 Dasgupta, T. & Umarji, A. M. Role of milling parameters and impurity on the thermoelectric properties of mechanically alloyed chromium silicide. *J. Alloy. Compd.* **461**, 292-297 (2008).
55 Umemoto, M. Preparation of Thermoelectric BETA-$FeSi_2$ Doped with Al and Mn by Mechanical Alloying. *Materials Transactions Jim* **36**, 373-383 (1995).
56 Inui, H. in *Materials and Technologies for Direct Thermal-to-Electric Energy Conversion* Vol. 886 *Materials Research Society Symposium Proceedings* (eds J. Yang, T. P. Hogan, R. Funahashi, & G. S. Nolas) 219-229 (2006).
57 Arita, Y., Mitsuda, S., Nishi, Y., Matsui, T. & Nagasaki, T. Thermoelectric properties of Rh-doped Ru_2Si_3 prepared by floating zone melting method. *J. Nucl. Mater.* **294**, 202-205 (2001).
58 Nowotny, H. The Chemistry of Extended Defects in Non-Metallic Solids. *North-Holland Publishing Co. Amsterdam* (1970).
59 Fedorov, M. I. & Zaitsev, V. K. "Thermoelectrics of Transition Metal Silicides," in CRC Handbook of Thermoelectrics: macro to nano, Ed. Rowe D.M., *CRC press: Boca Raton, FL*. (2006).
60 Karpinski, O. G. & Evseev, B. A. *Izv. Akad. Nauk SSSR, Neorg. Materialy* **5**, 525 (1969).
61 Shwomma, O., Preisinger, A., Nowotny, H. & Wittman, A. *Monatsh. Chem.* **95**, 1527 (1964).
62 Knott, H. W., Mueller, M. H. & Heaton, L. *Acta Crystallogr.* **23**, 549 (1967).
63 Zwilling, G. & Nowotny, H. *Monatsh. Chem.* **102**, 672 (1971).
64 Miyazaki, Y., Igarashi, D., Hayashi, K., Kajitani, T. & Yubuta, K. Modulated crystal structure of chimney-ladder higher manganese silicides MnSi gamma (gamma similar to 1.74). *Phys. Rev. B* **78** (2008).
65 Shukla, A., Kang, Y.-B. & Pelton, A. D. Thermodynamic assessment of the Si-Zn, Mn-Si, Mg-Si-Zn and Mg-Mn-Si systems. *Calphad.* **32**, 470-477 (2008).
66 Aoyama, I. *et al.* Effects of ge doping on micromorphology of MnSi in MnSi similar to 1.7 and on their thermoelectric transport properties. *Jpn. J. Appl. Phys.* **44**, 8562-8570 (2005).
67 de Ridder, R., van Tendeloo, G. & Amelinckx, S. Electron microscopic study of the chimney ladder structures $MnSi_{2-x}$ and $MoGe_{2-x}$. *Phys. Status solidi A* **33**, 383-393 (1976).
68 Ye, H. Q. & Amelinckx, S. High-resolution electron microscopic study of manganese silicides $MnSi_{2-x}$. *J. Solid State Chem.* **61**, 8-39 (1986).
69 Bost, M. C. & Mahan, J. E. An optical determination of the bandgap of the most silicon-rich manganese silicide phase. *J. Electron. Mater.* **16**, 389-395 (1987).
70 Rebien, M., Henrion, W., Angermann, H. & Teichert, S. Interband optical properties of higher manganese silicide thin films. *Appl. Phys. Lett.* **81**, 649-651 (2002).

71 Gao, Y. *et al.* Microstructural and optical properties of semiconducting $MnSi_{1.7}$ synthesized by ion implantation. *Jpn. J. Appl. Phys. Part 1-Regular Papers Brief Communications & Review Papers* **46**, 5777-5779 (2007).
72 Mahan, J. E. The potential of higher manganese silicide as an optoelectronic thin film material. *Thin Solid Films* **461**, 152-159 (2004).
73 Okada, S. *et al.* Crystal growth by molten metal flux method and properties of manganese silicides. *J. Alloy. Compd.* **317**, 315-319 (2001).
74 Okada, S. *et al.* MnSi and $MnSi_{2-x}$ single crystals growth by Ga flux method and properties. *J. Cryst. Growth* **229**, 532-536 (2001).
75 Girard, S. N. *et al.* Thermoelectric Properties of Undoped High Purity Higher Manganese Silicides Grown by Chemical Vapor Transport. *Chem. Mater.* **26**, 5097-5104 (2014).
76 Chen, X., Weathers, A., Moore, A., Zhou, J. & Shi, L. Thermoelectric Properties of Cold-Pressed Higher Manganese Silicides for Waste Heat Recovery. *J. Electron. Mater.* **41**, 1564-1572 (2012).
77 Zhou, A. J., Zhu, T. J., Ni, H. L., Zhang, Q. & Zhao, X. B. Preparation and transport properties of $CeSi_2$/HMS thermoelectric composites. *J. Alloy. Compd.* **455**, 255-258 (2008).
78 Luo, W. H., Li, H., Fu, F., Hao, W. & Tang, X. F. Improved Thermoelectric Properties of Al-Doped Higher Manganese Silicide Prepared by a Rapid Solidification Method. *J. Electron. Mater.* **40**, 1233-1237 (2011).
79 Itoh, T. & Yamada, M. Synthesis of Thermoelectric Manganese Silicide by Mechanical Alloying and Pulse Discharge Sintering. *J. Electron. Mater.* **38**, 925-929 (2009).
80 Higgins, J. M., Schmitt, A. L., Guzei, I. A. & Jin, S. Higher Manganese Silicide Nanowires of Nowotny Chimney Ladder Phase. *J. Am. Chem. Soc.* **130**, 16086-16094 (2008).
81 Pokhrel, A., Degregorio, Z. P., Higgins, J. M., Girard, S. N. & Jin, S. Vapor Phase Conversion Synthesis of Higher Manganese Silicide ($MnSi_{1.75}$) Nanowire Arrays for Thermoelectric Applications. *Chem. Mater.* **25**, 632-638 (2013).
82 Okamoto, N. L., Koyama, T., Kishida, K., Tanaka, K. & Inui, H. Crystal structure and thermoelectric properties of chimney-ladder compounds in the Ru_2Si_3-Mn_4Si_7 pseudobinary system. *Acta Mater.* **57**, 5036-5045 (2009).
83 Miyazaki, Y., Saito, Y., Hayashi, K., Yubuta, K. & Kajitani, T. Preparation and Thermoelectric Properties of a Chimney-Ladder $(Mn_{1-x}Fe_x)Si_\gamma$ (γ~1.7) Solid Solution. *Jpn. J. Appl. Phys.* **50** (2011).
84 Kikuchi, Y. *et al.* Enhanced Thermoelectric Performance of a Chimney-Ladder $(Mn_{1-x}Cr_x)Si_\gamma$ (γ~1.7) Solid Solution. *Jpn. J. Appl. Phys.* **51**, 085801 (2012).
85 Ponnambalam, V. & Morelli, D. T. Effect of Cr and Fe Substitution on the Transport Properties of the Nowotny Chimney-Ladder MnSi delta (1.73 < delta < 1.75) Compounds. *J. Electron. Mater.* **41**, 1389-1394 (2012).
86 Zhou, A. J. *et al.* Improved Thermoelectric Performance of Higher Manganese Silicides with Ge Additions. *J. Electron. Mater.* **39**, 2002-2007 (2010).

87 Allam, A., Boulet, P. & Record, M.-C. Substitutional Atom Influence on the Electronic and Transport Properties of Mn_4Si_7. *J. Electron. Mater.* **43**, 761-773 (2014).
88 Zhou, A. J. *et al.* Composites of Higher Manganese Silicides and Nanostructured Secondary Phases and Their Thermoelectric Properties. *J. Electron. Mater.* **38**, 1072-1077 (2009).
89 Luo, W. H. *et al.* Rapid synthesis of high thermoelectric performance higher manganese silicide with in-situ formed nano-phase of MnSi. *Intermetallics* **19**, 404-408 (2011).
90 Norouzzadeh, P., Zamanipour, Z., Krasinski, J. S. & Vashaee, D. The effect of nanostructuring on thermoelectric transport properties of p-type higher manganese silicide $MnSi_{1.73}$. *J. Appl. Phys.* **112**, 124308 (2012).
91 Sadia, Y. & Gelbstein, Y. Silicon-Rich Higher Manganese Silicides for Thermoelectric Applications. *J. Electron. Mater.* **41**, 1504-1508 (2012).
92 Truong, D. Y. N., Kleinke, H. & Gascoin, F. Thermoelectric properties of higher manganese silicide/multi-walled carbon nanotube composites. *Dalton. Trans.* **43**, 15092-15097 (2014).
93 Saleemi, M. *et al.* Thermoelectric performance of higher manganese silicide nanocomposites. *J. Alloy. Compd.* **619**, 31-37 (2015).
94 Zamanipour, Z. *et al.* Synthesis, characterization, and thermoelectric properties of nanostructured bulk p-type $MnSi_{1.73}$, $MnSi_{1.75}$, and $MnSi_{1.77}$. *Ceram. Int.* **39**, 2353-2358 (2013).
95 Itoh, T. & Ono, N. Influence of Addition of Alumina Nanoparticles on Thermoelectric Properties of Higher Manganese Silicide. *MRS Online Proceedings Library* **1490**, 127-132 (2013).
96 Zhou, A. J., Zhu, T. J., Zhao, X. B. & Mueller, E. Grain size effect on the phase transformations of higher manganese silicide thermoelectric materials: An in situ energy dispersive x-ray diffraction study. *J. Mater. Res.* **26**, 1900-1906 (2011).
97 Kikuchi, Y., Nakajo, T., Hayashi, K. & Miyazaki, Y. High temperature X-ray diffraction study on incommensurate composite crystal $MnSi_\gamma$ – (3+1)-dimensional superspace approach. *J. Alloy. Compd.* **616**, 263-267 (2014).
98 Allam, A. *et al.* Phase transformations in Higher Manganese Silicides. *J. Alloy. Compd.* **551**, 30-36 (2013).
99 Schwomma, O., Preisinger, A., Nowotny, H. & Wittmann, A. Die Kristallstruktur von $Mn_{11}Si_{19}$ und deren Zusammenhang mit Disilicid-Typen. *Monatshefte für Chemie und verwandte Teile anderer Wissenschaften* **95**, 1527-1537 (1964).
100 Fredrickson, D. C., Lee, S., Hoffmann, R. & Lin, J. The Nowotny Chimney Ladder Phases: Following the cpseudo Clue toward an Explanation of the 14 Electron Rule. *Inorg. Chem.* **43**, 6151-6158 (2004).
101 Goldsmid, H. J. The Thermal Conductivity of Bismuth Telluride. *Proc. Phys. Soc. B* **69**, 203-209 (1956).
102 Akhmedova, G. A. & Abdinov, D. S. Effect of thallium doping on the thermal conductivity of PbTe single crystals. *Inorg. Mater.* **45**, 854-858 (2009).

103 Toberer, E. S., Christensen, M., Iversen, B. B. & Snyder, G. J. High temperature thermoelectric efficiency in $Ba_8Ga_{16}Ge_{30}$. *Phys. Rev. B* **77**, 075203 (2008).
104 Yonenaga, I., Akashi, T. & Goto, T. Thermal and electrical properties of Czochralski grown GeSi single crystals. *J. Phys. Chem. Solids* **62**, 1313-1317 (2001).
105 Lamberton, G. A. *et al.* High figure of merit in Eu-filled CoSb3-based skutterudites. *Appl. Phys. Lett.* **80**, 598-600 (2002).
106 Slack, G. A. & Oliver, D. W. Thermal Conductivity of Garnets and Phonon Scattering by Rare-Earth Ions. *Physical Review B* **4**, 592-609 (1971).
107 Chen X. *et al.* Twisting Phonons in Complex Crystals with Quasi-One-Dimensional Substructures. *Under review.*
108 De Ridder, R. & Amelinckx, S. The structure of defect manganese silicides. *Mater. Res. Bull.* **6**, 1223-1234 (1971).
109 Ma, J. *et al.* Glass-like phonon scattering from a spontaneous nanostructure in $AgSbTe_2$. *Nature Nanotechnol.***8**, 445-451 (2013).
110 Aouissi, M., Hamdi, I., Meskini, N. & Qteish, A. Phonon spectra of diamond, Si, Ge, and α-Sn: Calculations with real-space interatomic force constants. *Phys. Rev. B* **74**, 054302 (2006).
111 Jood, P. *et al.* Microstructural Control and Thermoelectric Properties of Misfit Layered Sulfides $(LaS)_{(1+m)}TS_2$ (T = Cr, Nb): The Natural Superlattice Systems. *Chem. Mater.* **26**, 2684-2692 (2014).
112 Shikano, M. & Funahashi, R. Electrical and thermal properties of single-crystalline $(Ca_2CoO_3)_{0.7}CoO_2$ with a $Ca_3Co_4O_9$ structure. *Appl. Phys. Lett.* **82**, 1851-1853 (2003).
113 Cheng, J. G., Zhou, J. S. & Goodenough, J. B. Stress-induced perovskite to post-perovskite transition in CaIrO3 at room temperature. *Phys. Rev. B* **82**, 132103 (2010).
114 Aoyama, I. *et al.* Doping effects on thermoelectric properties of higher manganese silicides (HMSs, $MnSi_{1.74}$) and characterization of thermoelectric generating module using p-type (Al, Ge and Mo)-doped HMSs and n-type $Mg_2Si_{0.4}Sn_{0.6}$ legs. *Jpn. J. Appl. Phys. Part 1-Regular Papers Brief Communications & Review Papers* **44**, 4275-4281 (2005).
115 Koirala, M. *et al.* Thermoelectric property enhancement by Cu nanoparticles in nanostructured $FeSb_2$. *Appl. Phys. Lett.* **102**, 213111 (2013).
116 Kawasumi, I., Sakata, M., Nishida, I. & Masumoto, K. Crystal growth of manganese silicide, $MnSi_{\sim 1.73}$ and semiconducting properties of $Mn_{15}Si_{26}$. *J. Mater. Sci.* **16**, 355-366 (1981).
117 Nishida, I. Semiconducting properties of nonstoichiometric manganese silicides. *J. Mater. Sci.* **7**, 435 (1972).
118 Glassbrenner, C. J. & Slack, G. A. Thermal Conductivity of Silicon and Germanium from 3°K to the Melting Point. *Phys. Rev. A-General Physics* **134**, 1058 (1964).

119 Cahill, D. G. & Pohl, R. O. Thermal properties of a tetrahedrally bonded amorphous solid: $CdGeAs_2$. *Phys. Rev. B* **37**, 8773-8780 (1988).
120 Wang, Z. J., Alaniz, J. E., Jang, W. Y., Garay, J. E. & Dames, C. Thermal Conductivity of Nanocrystalline Silicon: Importance of Grain Size and Frequency-Dependent Mean Free Paths. *Nano Lett.* **11**, 2206-2213 (2011).
121 Zaitsev, V. K. & Fedorov, M. I. "Thermal conductivity of semiconductors with complex crystal structures," in *CRC Handbook of Thermoelectrics: macro to nano,* Ed. Rowe D.M., CRC press: Boca Raton, FL. (2006).
122 Fu, C. G., Xie, H. H., Zhu, T. J., Xie, J. & Zhao, X. B. Enhanced phonon scattering by mass and strain field fluctuations in Nb substituted FeVSb half-Heusler thermoelectric materials. *J. Appl. Phys.* **112** (2012).
123 Terazawa, Y., Mikami, M., Itoh, T. & Takeuchi, T. Effects of Heavy Element Substitution on Electronic Structure and Lattice Thermal Conductivity of Fe_2VAl Thermoelectric Material. *J. Electron. Mater.* **41**, 1348-1353 (2012).
124 Ponnambalam, V., Morelli, D. T., Bhattacharya, S. & Tritt, T. M. The role of simultaneous substitution of Cr and Ru on the thermoelectric properties of defect manganese silicides MnSi delta (1.73 < delta < 1.75). *J. Alloy. Compd.* **580**, 598-603 (2013).
125 Ivanova, L. D. Preparation of thermoelectric materials based on higher manganese silicide. *Inorg. Mater.* **47**, 965-970 (2011).
126 Cahill, D. G., Watson, S. K. & Pohl, R. O. Lower limit to the thermal conductivity of disordered crystals. *Phys. Rev. B* **46**, 6131-6140 (1992).
127 Pauling, L. The Chemical Bond. *Cornell University Press, Ithaca, New York* (1967).
128 Kishida, K. *et al.* Thermoelectric properties of ternary and Al-containing quaternary Ru1-xRexSiy chimney-ladder compounds. *Acta Mater.* **57**, 2010-2019 (2009).
129 Slack, G. A. & Hussain, M. A. The maximum possible conversion efficiency of silicon - germanium thermoelectric generators. *J. Appl. Phys.* **70**, 2694-2718 (1991).
130 Glicksman, M. Mobility of Electrons in Germanium-Silicon Alloys. *Phys.Rev.* **111**, 125-128 (1958).
131 Bardeen, J. & Shockley, W. Deformation Potentials and Mobilities in Non-Polar Crystals. *Phys.l Rev.* **80**, 72-80 (1950).
132 Liu, W. *et al.* Enhanced thermoelectric properties of n-type $Mg_{2.16}(Si_{0.4}Sn_{0.6})_{1-y}Sb_y$ due to nano-sized Sn-rich precipitates and an optimized electron concentration. *J. Mater. Chem.* **22**, 13653-13661 (2012).
133 Callaway, J. & von Baeyer, H. C. Effect of Point Imperfections on Lattice Thermal Conductivity. *Phys. Rev.* **120**, 1149-1154 (1960).
134 Yang, J., Meisner, G. P. & Chen, L. Strain field fluctuation effects on lattice thermal conductivity of ZrNiSn-based thermoelectric compounds. *Appl. Phys. Lett.* **85**, 1140-1142 (2004).

135 Pei, Y. L. *et al.* High thermoelectric performance of oxyselenides: intrinsically low thermal conductivity of Ca-doped BiCuSeO. *Npg Asia Materials* **5** (2013).
136 Kurosaki, K., Kosuga, A., Muta, H., Uno, M. & Yamanaka, S. Ag_9TITe_5: A high-performance thermoelectric bulk material with extremely low thermal conductivity. *Appl. Phys. Lett.* **87** (2005).
137 Sanditov, D. S. & Belomestnykh, V. N. Relation between the Parameters of the Elasticity Theory and Averaged Bulk Modulus of Solids. *Tech. Phys.* **56**, 1619-1623 (2011).
138 Bouvier, M., Lethuillier, P. & Schmitt, D. Specific heat in some gadolinium compounds. I. Experimental. *Phys. Rev. B* **43**, 13137-13144 (1991).
139 Bux, S. K. *et al.* Nanostructured Bulk Silicon as an Effective Thermoelectric Material. *Adv. Funct. Mater.* **19**, 2445-2452 (2009).
140 Rowe, D. M. & Shukla, V. S. The effect of phonon - grain boundary scattering on the lattice thermal conductivity and thermoelectric conversion efficiency of heavily doped fine - grained, hot - pressed silicon germanium alloy. *J. Appl. Phys.* **52**, 7421-7426 (1981).
141 Goldsmid, H. J. & Penn, A. W. Boundary scattering of phonons in solid solutions. *Phys. Lett. A* **27**, 523 (1968).
142 Parrott, J. E. The thermal conductivity of sintered semiconductor alloys. *J. Phys. C Solid State Phys.* **2**, 147 (1969).
143 Kim, D. H. & Mitani, T. Thermoelectric properties of fine-grained Bi_2Te_3 alloys. *J. Alloy. Compd.* **399**, 14-19 (2005).
144 Coble, R. L. Sintering Crystalline Solids. I. Intermediate and Final State Diffusion Models. *J. Appl. Phys.* **32**, 787-792 (1961).
145 Mott, N. F. Metal-Insulator transition. *Taylor & Francis, London* (1990).
146 Zhou, A. J. *et al.* Microstructure and thermoelectric properties of SiGe-added higher manganese silicides. *Mater. Chem. Phys.* **124**, 1001-1005 (2010).
147 Groβ, E., Riffel, M. & Stohrer, U. Thermoelectric generators made of $FeSi_2$ and HMS: Fabrication and measurement. *J. Mater. Res.* **10**, 34-40 (1995).
148 Nan, C. W., Birringer, R., Clarke, D. R. & Gleiter, H. Effective thermal conductivity of particulate composites with interfacial thermal resistance. *J. Appl. Phys.* **81**, 6692-6699 (1997).
149 Toprak, M. S. *et al.* The impact of nanostructuring on the thermal conductivity of thermoelectric $CoSb_3$. *Adv. Funct. Mater.* **14**, 1189-1196 (2004).
150 Nan, C. W. & Birringer, R. Determining the Kapitza resistance and the thermal conductivity of polycrystals: A simple model. *Phys. Rev. B* **57**, 8264-8268 (1998).
151 Zhou, A. J. *et al.* Mechanochemical decomposition of higher manganese suicides in the ball milling process. *Intermetallics* **18**, 2051-2056 (2010).
152 Umemoto, M., Liu, Z. G., Omatsuzawa, R. & Tsuchiya, K. in *Mater. Sci. Forum* Vol. 343-346 *Mater. Sci. Forum* 918-923 (2000).
153 Sadia, Y., Dinnerman, L. & Gelbstein, Y. Mechanical Alloying and Spark Plasma Sintering of Higher Manganese Silicides for Thermoelectric Applications. *J. Electron. Mater.* **42**, 1926-1931 (2013).

154 Lee, Y. G., Choi, M. K., Kim, I. H. & Ur, S. C. Thermoelectric properties of Nowotny phase, higher manganese silicides synthesized by mechanical alloying process. *J. Ceram. Process. Res.* **13**, 816-819 (2012).
155 Shin, D. K., Jang, K. W., Ur, S. C. & Kim, I. H. Thermoelectric Properties of Higher Manganese Silicides Prepared by Mechanical Alloying and Hot Pressing. *J. Electron. Mater.* **42**, 1756-1761 (2013).
156 Liu, X. *et al.* Low Electron Scattering Potentials in High Performance $Mg_2Si_{0.45}Sn_{0.55}$ Based Thermoelectric Solid Solutions with Band Convergence. *Adv. Energy Mater.* **3**, 1238-1244 (2013).

Vita

Xi Chen was born in Taicang, P.R. China. Following graduation from Jiangsu Taicang Senior High School in 2003, he attended Southeast University, earning his bachelor's degree in Materials Science and Engineering in 2007. Then he went to the Zhejiang University for his graduate study and got his master degree in Materials Science and Engineering in 2010. He is currently pursuing a doctoral degree in Materials Science and Engineering from the University of Texas at Austin, where his research interests include synthesis and thermoelectric transport properties of environmentally-friendly silicides.

Email address: chen1@utexas.edu

This dissertation was typed by the author.